UC Berkeley
UC Berkeley Electronic Theses and Dissertations

Title
MEMS Resonant Strain Sensor Integration

Permalink
https://escholarship.org/uc/item/11v8j97m

Author
Myers, David Richard

Publication Date
2010

Peer reviewed|Thesis/dissertation

eScholarship.org Powered by the California Digital Library
University of California

MEMS Resonant Strain Sensor Integration

by

David Richard Myers

A dissertation submitted in partial satisfaction of the

requirements for the degree of

Doctor of Philosophy

in

Engineering - Mechanical Engineering

in the

Graduate Division

of the

University of California, Berkeley

Committee in charge:

Professor Albert P. Pisano, Chair
Professor Liwei Lin
Professor Andrew Neureuther

Fall 2010

MEMS Resonant Strain Sensor Integration

Copyright © 2010

by

David Richard Myers

Abstract

MEMS Resonant Strain Sensor Integration

by

David Richard Myers

Doctor of Philosophy in Engineering - Mechanical Engineering

University of California, Berkeley

Professor Albert P. Pisano, Chair

Despite commercial availability since the 1950's, silicon strain sensors have not experienced the same success as other microdevices, such as accelerometers, pressure sensors, and inkjet heads. Strain sensors measure mechanical deformation and could be used in many structural components, improving safety, controls, and manufacturing tolerances. This thesis examines major strain sensing techniques and highlights both advantages and disadvantages of each. MEMS resonant strain gauges are identified to have superior performance over many traditional strain gauges in terms of sensitivity, resolution, stability, and size. To use these gauges, additional issues such as harsh environment survivability, strain transfer, temperature stability, and encapsulation must be solved, as detailed in this thesis.

Concerning harsh environment survivability, this work presents a MEMS resonant strain gauge fabricated from silicon carbide, which operates at 600°C, and has been tested to 64,000 G, while still resolving 0.01 microstrain in a 10 kHz bandwidth. Specific details on how to create harsh environment testing equipment are presented. Additionally, this original work identifies a unique temperature stability method based on purposely mismatched device and substrate layers. Full analytical equations are presented, and experimental confirmation of the scheme shows that temperature stability is improved from 23 ppm/°C to 3.6 ppm/°C.

All MEMS devices are created on flat substrates, which are useful when integrating electronics, but can be difficult to use when measuring strain in structural components, especially round objects. Furthermore, no work has been presented for gauges operating at high strain. To address this issue, this thesis contains the first demonstration of a MEMS resonant strain gauge operating at 1000 microstrain on a static automobile halfshaft. Details on joining the substrate to the circular halfshaft are presented, as well as how to treat the issue of strain transfer.

To protect the device, encapsulation is designed specifically to not change the strain sensitivity of the gauge. The encapsulation utilizes directional ion beam sputtering, which is experimentally shown to deposit spatially confined, extremely thin material through the release holes. Typical depositions were nanometers in thickness (<0.5% of deposited material) and on the order of tens to hundreds of femtograms.

For my love

Contents

Contents ii

List of Figures vi

Acknowledgements viii

1 Introduction 1

1.1 MEMS Integration Overview 1
1.2 Review of Existing Strain Sensing Technology 2
1.2.1 Metal Foil Strain Gauges 3
1.2.2 Piezoresistive & Piezoelectric Strain Gauges 3
1.2.3 Surface Acoustic Wave Strain Gauges 4
1.2.4 Optical Strain Gauges 5
1.2.5 MEMS Capacitive Based Strain Gauges 5
1.2.6 MEMS Double-Ended Tuning Fork Strain Gauges 6
1.3 Key DETF Integration Issues in Thesis 6
1.3.1 Harsh Environment Survivability 6
1.3.2 Temperature Stability 7
1.3.3 Bonding & Strain Transfer 8
1.3.4 Encapsulation 9
1.4 Remaining DETF Issues 9
1.4.1 Thermal strains 9
1.4.2 Power & Wireless Data Transfer 10
1.5 Concluding Remarks 11

2 Harsh Environment Strain Gauge **12**
2.1 Silicon Carbide DETF and Uses . . . 12
2.2 Device Structure and Fabrication . . . 13
2.2.1 Extending Device Survivability to 600°C . . . 13
2.2.2 Etching Considerations . . . 15
2.3 Test Setup and Characterization . . . 17
2.3.1 Strain Sensitivity, Strain Noise, & Quality Factor . . . 17
2.3.2 High Temperature Testing . . . 17
2.3.3 Shock Testing . . . 19
2.4 Results . . . 19
2.4.1 Phase Noise . . . 19
2.4.2 Quality Factor under Vacuum . . . 22
2.4.3 Temperature Sensitivity . . . 22
2.4.4 Shock Testing . . . 24
2.5 Discussion . . . 24

3 Temperature Compensation **26**
3.1 Temperature Compensation Overview & Methods . . . 26
3.2 Analytical Model . . . 28
3.2.1 Frequency of Fixed-Fixed Beam with Trapezoidal Cross Section . . . 28
3.2.2 Modulus of Elasticity of Silicon Carbide . . . 29
3.2.3 Mechanical & Thermal Strain . . . 30
3.2.4 Physical Insight . . . 31
3.2.5 Turn-over Temperature . . . 32
3.3 Measurement Setup . . . 32
3.4 Results . . . 36
3.4.1 Coefficients of Thermal Expansion . . . 36
3.4.2 Thermal Strain & Frequency Response . . . 37
3.4.3 Turnover Temperature Estimates . . . 39
3.5 Discussion . . . 39

4 Strain & Torque Testing **41**

4.1 Torque Sensor Uses and MEMS Potential . . . 41

4.2 Torque Measurements & Strain Transfer . . . 43

4.2.1 Strain Based Torque Measurement . . . 43

4.2.2 MEMS Double Ended Tuning Fork Strain Equation . . . 43

4.2.3 Strain Transfer for Torque . . . 44

4.2.4 DETF High Strain Analysis . . . 45

4.3 Experiment . . . 46

4.3.1 Torque Testing Apparatus . . . 46

4.3.2 Epoxy Bonding . . . 47

4.3.3 Metallic Adhesive Induction Bonding . . . 48

4.3.4 Testing . . . 49

4.4 Results . . . 49

4.4.1 Strain Sensitivity . . . 49

4.4.2 Temperature Sensitivity . . . 54

4.5 Discussion . . . 56

5 Ion Beam Sputtered Silicon Carbide Encapsulation & Film Characterization **57**

5.1 Tuning Fork Encapsulation Issues and Needs . . . 57

5.2 Ion Beam Deposited Silicon Carbide for Encapsulation . . . 58

5.3 Encapsulation Overview & Design . . . 61

5.3.1 Stress & Deflection Calculation . . . 62

5.3.2 Nonlinear Considerations . . . 64

5.3.3 Shock Survivability . . . 64

5.3.4 Encapsulation Effect on Strain Transfer . . . 64

5.4 Through Hole Deposition Experimental Testing . . . 65

5.5 Mass Loading Results . . . 67

5.5.1 Deposition Spatial Confinement . . . 67

5.5.2 Deposition Shape Analysis . . . 67

5.5.3 Mass Estimates . . . 70

5.6 Discussion 73

6 Conclusions & Future Work **74**

6.1 Improved Harsh Environment Survivability 74

6.2 Temperature Stability & Compensation 75

6.3 High Strain Torque Testing 76

6.4 Low Mass Loading Encapsulation 76

Bibliography **78**

List of Figures

1.1 Viewgraphs of Current Strain Sensing Technology 4
1.2 Overview of Strain Sensing Integration Issues 7

2.1 Balanced Mass Double Ended Tuning Fork and Principle of Operation 14
2.2 Silicon Carbide BDETF Cross Section 15
2.3 Square Wave Oscillator Board with MEMS 16
2.4 High Temperature Testing Setup 18
2.5 High Shock Testing Setup 18
2.6 Phase Noise of SiC BDETF as a function of Bias Voltage 20
2.7 Clearly visible SiC layers in BDETF 21
2.8 Quality Factor of BDETF at Different Pressures 21
2.9 Temperature Sensitivity of BDETF 23
2.10 Sample Dry Steam Testing Results 23
2.11 Time Lapse Photography of the Shock Event 25
2.12 Experimental Data extracted from Time Lapse Photography 25

3.1 Conceptual Schematic of DETF Temperature Compensation Scheme 27
3.2 Figure and Schematic of Tuning Forks used in Temperature Compensation . 33
3.3 Temperature Testing of DETF structures 35
3.4 Comparison of Coefficients of Thermal Expansion of SiC and Si 38
3.5 Thermal Strains Induced in DETF 38
3.6 Experimental and Predicted Frequencies as a Function of Temperature . . . 40
3.7 Turnover Temperature Geometric Tunability 40

4.1 Conceptual Image of MEMS Torque Measurement System 42

4.2 Engineering Shear Strain through Silicon Die on Halfshaft 45
4.3 Torque Testing Apparatus 47
4.4 Induction Bonding and Temporal Temperature Data 50
4.5 Torque Measurement Experimental Setup 50
4.6 DETF Strain Transfer Experimental Results for Torque 51
4.7 Measured frequency response to Applied Strain for Epoxy 52
4.8 Measured frequency response to Small Applied Strain for Epoxy 53
4.9 Calculated Torque Sensitivity 54
4.10 Frequency Response to Temperature using Metal Bond 55
4.11 Frequency Response to Temperature using Epoxy Bond 55

5.1 Key Needs of DETF Encapsulation 59
5.2 Possible Encapsulation Sealing Methods 60
5.3 Conceptual Schematic of Ion Beam Deposited SiC Encapsulation 61
5.4 Design Graph of SiC Encapsulation 63
5.5 Experimental Setup and Deposition Step Overview 66
5.6 SEM of Test Structure and Through Hole Deposition 68
5.7 KOH testing of Through Hole Deposition 68
5.8 Width of Mass Deposits 69
5.9 Heights of Mass Deposits 69
5.10 Evolution Profile of Mass Deposits 71
5.11 Deposition Angles and Rates 71
5.12 Mass Measurements of Through Hole Deposition for various times 72

Acknowledgements

I received a great deal of support in completing this degree, and this thesis would simply not exist were it not for the care and help of my friends, colleagues, and mentors. I'd like to begin by thanking Al for inviting me into his group. Al has a knack for putting together amazing teams of people at any given time, and I've been extremely grateful for my entire time in Berkeley Micromechanical Analysis Design Group. I'm also grateful to my qualifying exam committee members, Prof. Lin, Prof. Mao, Prof. Liepmann, and Prof. Neureuther, for their insights and support.

Robert Azevedo and Muthu Wijesundara graciously mentored me and taught me a great deal about design, research, writing, micro-processing, and ion beam deposition. They were instrumental to helping me get a fast start at BMAD. More importantly, I'm deeply thankful to all the help they have provided over the years. I also learned a great deal about writing from Brian Sosnowchik, and hope that my writing does his lessons justice.

Within this thesis, several components were possible because of a team effort. Babak Jamshidi was behind the high temperature testing setup and did a great job putting that together. Matt Chan and Brian Sosnowchik were instrumental in getting an induction bonded strain sensor onto the halfshaft. Also, Brian Sosnowchik was kind enough to assist with the AFM images used in the mass loading section. I'm thankful to all of these people, and it was my utmost pleasure to work with them.

The Berkeley Micromechanical Analysis and Design Group (BMAD) has always made research fun. My life has been enriched by the many people that I have met over the years. Moreover, I am thankful for the close friends that I have made: Rob Azevedo, Muthu Wijesundara, Josh Heppner, Mike Mueller, Gabriele Vigevani, Chris Hogue, and Matt Chan.

I would like to say a special thanks to Donna Craig and Joe Donnelly. Donna has always been there at pivotal moments in my graduate career. She helped me make it out to Berkeley; transition to a lab with a good fit; and for keeping me in grad school (Yes, you actually do need to register by the third week of classes!). Joe has been a good friend, and has spent countless hours working with me in the microlab on the ion beam deposition system to ensure that it is running in top condition.

Finally, I would like to thank my beautiful wife, Becky. She has always encouraged me to do my absolute best. She originally pushed me to pursue the opportunity to study at Berkeley. Over the years, she has given me support, love, and understanding. I am deeply indebted and grateful to her for my happiness.

Chapter 1

Introduction

1.1 MEMS Integration Overview

This thesis specifically considers MEMS resonant strain sensors and the challenges which have prevented them from becoming commercially successful. Specifically, MEMS double-ended tuning fork (DETF) strain gauges are identified to have superior performance over traditional strain gauges in terms of sensitivity, resolution, stability, and size. To use these gauges, additional issues such as harsh environment survivability, strain transfer, temperature stability, and encapsulation must be solved, as detailed in this initial chapter. The remaining chapters will focus on each individual issue, and recommend solutions. However, before examining these issues, it is helpful to first consider a brief history of MEMS, noting both successes and failures, and to provide some context on the development of MEMS resonant strain sensors.

Although the exact starting date of microelectromechanical systems (MEMS) is a bit ambiguous, most experts agree on a few common milestones branching from the integrated circuit industry, such as the invention of surface micromachining [1]. Since that early time, a number of researchers have made great strides towards the goal of creating fully integrated sensing systems and sensing networks. Within the commercial sector, some MEMS products have been quite successful, including inertial sensors such as Analog Device's accelerometer lines, or the highly anticipated Invensense gyroscopes, or Texas Instruments Digital Light Projection, or Knowles MEMS Microphones. The key to the success of all of these products has been the successful integration of the MEMS based device and the surrounding sensing environment.

Despite the inherent advantages of MEMS in regards to cost, size, and sensitivity, additional precautions are needed to ensure that the devices are properly protected from extra-

neous environmental stimuli. Furthermore, the size and cost of these devices opens up the possibility of ubiquitous network sensing, but only with additional research on wireless data transmission and reasonable power requirements. Hence, research on MEMS integration with the local environment is essential.

The MEMS strain gauge presents an interesting example of the need for integration research. Silicon piezoresistive strain gauges were first offered commercially in 1958 by Kulite. However, many MEMS technologies which were introduced much later in the 1970's have gone on to become successful products, where MEMS strain sensors tend only to be used in research settings. While one could argue that there are non-MEMS based strain sensors commercially available, they do not enjoy the same ubiquity of pressure sensors, print heads, and inertial sensors.

This is surprising when considering that strain gauges offer the ability to turn virtually any object into a force sensor. In the simplest case, this knowledge could be used to anticipate yielding and failure of a component. However, knowledge of the forces on different components could be used in active feedback systems, enabling better controls and smaller components.

A key reason for the lack of success is inherent to the measurand. Aside from optical strain sensors, strain sensors must be directly attached to an object in order to measure strain. However, this direct attachment can cause thermally applied strains, fatigue from repeated cycling, and creep. A number of different strain sensing solutions have been proposed over the years, but each one has a significant drawback which has prevented the technology from gaining widescale commercial acceptance. Simply put, the strain gauge must be able to only measure mechanical strain, remain stable, and be sensitive enough such that it can be mounted on virtually any part without modification.

In more recent times, the double-ended tuning fork (DETF) structure was examined as a strain sensor given it's high sensitivity. A continued research effort on these gauges has helped overcome some of the major integration issues which could prevent widescale success. From better temperature compensation [2], to harsh environment operation [3, 4], to nanostrain resolution [5]. The nanoscale resolution is of special interest since virtually all objects experience these levels of strain during normal use. Furthermore, these sensor can be attached to virtually any object and will have a minimum impact on the strength and dynamics of the structure given the small form factor.

1.2 Review of Existing Strain Sensing Technology

The following section gives a brief overview of competing strain sensing technologies, but is by no means exhaustive, skipping some technologies such as magnetoelastic based stress sensing [6]. The goal of this section is to examine a variety of strain sensing technologies, and note both the advantages and disadvantages of each. The section concludes with the

key advantages of MEMS double-ended tuning forks (DETF) and introduces what research is needed to solve remaining integration issues.

1.2.1 Metal Foil Strain Gauges

Traditional metal foil strain gauges are composed of a thin metal on a plastic substrate. Figure 1.1A shows a typical metal foil strain gauge. The metal is typically patterned in a serpentine shape, such that applied strain causes an elongation of the metal dimensions. As a consequence of Poisson's ratio, the metal also contracts in a perpendicular direction to the strain. Both phenomenon contribute to an increased resistance in the metal foil gauge.

Since the gauges are very thin and typically created on plastic substrates, they have the unique advantage of being very compliant relative to the component which they are measuring. The gauges may also be made from a number of different materials, enabling a good coefficient of thermal expansion (CTE) match with the measurement surface. However, these gauges typically suffer from creep and fatigue. Furthermore, since the measurement is resistive based, temperature increases cause thermal noise. Finally, they suffer from poor sensitivity compared to other strain gauges. The interested reader is referred to [7, 8] for further information on the theory and use of metal foil gauges.

1.2.2 Piezoresistive & Piezoelectric Strain Gauges

Initially, MEMS based strain sensors were piezoresistive based, and can be quite small as shown in Figure 1.1B. These sensors capitalized on the piezo-properties of silicon [12], which could be tailored using simple doping schemes. These sensors were easy to integrate using existing technology, since they could be created with a simple lithographic and ion implantation step. Compared to metal foil gauges, the sensitivity is 10 to 50 times greater. However, piezoresistive gauges suffer from high temperature sensitivities and nonlinear strain measurements [7]. Very small changes in temperature cause large changes in the sensor output, leading to erroneous measurements.

These sensors were originally commercialized by Kulite in 1958, which, according to their company website "began as the first commercial source of bare silicon strain gauges". However, it is interesting to note that the current primary focus of Kulite is on pressure transducers which utilize piezoresistive elements. Even today, the electrical change in a semiconductor due to applied strain is being used for high level research work [13]. However, the strain sensing properties are rarely used to directly measure strain on an object. This is most likely due to the originally mentioned drawbacks of piezoresistive gauges, which are the most useful in controlled environments.

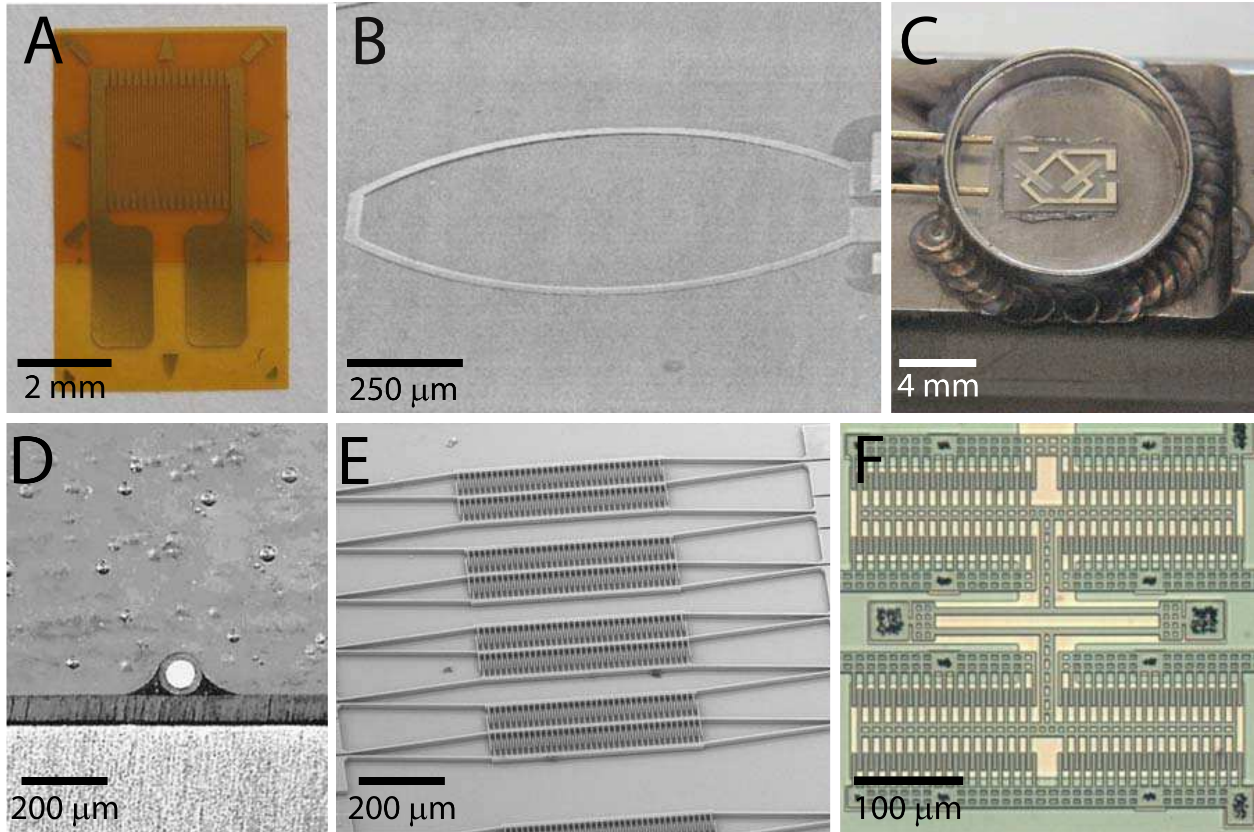

Figure 1.1. A) Metal Foil Strain Gauge B) Piezoelectric Strain Gauge C) SAW Torque Sensor with included package [9] D) Fiber Bragg Grating Based Optical Strain Gauge [10] E) MEMS Capacitive Based Strain Gauge [11] F) MEMS Double Ended Tuning Fork [5]

1.2.3 Surface Acoustic Wave Strain Gauges

Surface acoustic waves (SAW) were first shown to be directly coupled into a material in 1965 [14] using interdigitated electrodes on piezoelectric materials. SAWs can be used to detect temperature, strain, mass, conductivity, and other phenomenon [15]. In all cases, sensing is done by measuring changes in the path over which the acoustic waves travel [16]. SAW strain sensors, such as the one shown in Figure 1.1C can be wirelessly interrogated, eliminating the need for a power source.

As such, these sensors are enjoying some commercial success, as seen by Transense plc. and Honeywell (through licensing agreements). However, the ultimate success and ubiquitous use of these sensors will depend on overcoming some current issues. First, the packaging is quite large and cumbersome, locally reinforcing the area of measurement. Second, while the passive design is advantageous, careful attention must be paid to the antenna to ensure that it does not add a significant mass or volume on moving parts. Finally, SAW devices are typically constructed on piezoelectric substrates, limiting flexibility in reducing CTE mismatch with other materials. While this can be calibrated out on an individual basis,

even a two point temperature calibration (room temp and 90°C in Kalinin [17] will take quite a bit of time and effort.

1.2.4 Optical Strain Gauges

Optical Strain gauges typically refer to using optics to track the elongation of a material. There are multiple ways to do this, in the simplest case, a direct measurement may be made by tracking the change in distance between two points fixed to a material. Other possibilities involve gratings which cause changes in diffraction patterns [18]. Since the strain measurement is visual, the sensing electronics and optics do not necessarily need to be in direct contact with the gauge itself. This is a key advantage as the strain sensor can be created from materials which can survive harsh environments, and be remotely measured. However, the tools used to measure the optical gauges also represent the key disadvantage. They are typically bulky, preventing their use in confined spaces [19].

An important subset of optical strain gauges are based on fiber Bragg gratings. The fiber Bragg grating is created in a thin optic fiber and is composed of alternating sections of different indexes of refraction. This back and forth index of refraction will reflect a portion of light passed along the fiber, which is dependent on the strain. These fibers have the advantage of size, as shown in Figure 1.1D and electromagnetic insensitivity. However, these sensors need to be directly connected to the optical measurement equipment. To fully utilize this area microscale, disposable, optical equipment which can integrate with circuitry is needed.

1.2.5 MEMS Capacitive Based Strain Gauges

MEMS Capacitive based strain gauges simply transduce strain to a capacitive signal. The simplest case would be a parallel plate attached to a substrate. Strain induced in the substrate would cause the change in the distance between plates to increase or decrease, changing the capacitance. More complicated structures use mechanical linkages to amplify the movement caused by strain [20, 21, 11]. While the structure in [20] utilizes an optical readout, this could be changed into a capacitive structure.

One of the primary drawbacks to capacitive sensors is the sensitivity. This can be improved through the use of comb-drive structures [22], as seen in Figure 1.1F [11]. However, this typically means increasing the size of the gauge, which prevents localized strain measurements. This also is problematic because large area gauges are typically less shock resistant. However, MEMS based sensors can be easily mass produced and integrated with electronics and packaging. These gauges can also be created from materials which perform well in harsh environments [23, 11].

1.2.6 MEMS Double-Ended Tuning Fork Strain Gauges

The measured frequency of a double ended tuning fork (DETF) is dependent on applied strain. DETFs have been extensively studied [24, 25], since they can be used directly as strain sensors, or as the basis of more complicated sensors such as accelerometers [26] or gyroscopes [27]. The key advantage to using a frequency to strain conversion is that frequency can be measured with excellent accuracy, and electronics capable of measuring nanostrain have been created [5, 28].

DETFs share the advantages of MEMS capacitive strain gauges, with the added advantage of exceptional strain sensitivity. Unfortunately, they are also sensitive to other environmental influences, such as temperature, humidity, and pressure. The key to successfully implementing MEMS double ended tuning forks lies in isolating or compensating other environmental factors while maintaining a high strain sensitivity. This can be difficult as these isolation, protection, and compensation mechanisms can change the strain sensing properties of the devices.

Based on the high sensitivity, integrated electronics, and potential for use in a number of different environments, this thesis will focus on the integration and implementation of a MEMS DETF strain gauge. The key need is to provide solutions to integration issues which do not affect the existing strengths of the gauge. For example, encapsulation must be designed not to change the strain sensitivity of the device. As such, a systems overview of the DETF strain gauge is needed.

1.3 Key DETF Integration Issues in Thesis

There are a number of integration issues which need to be resolved before any MEMS based strain gauge may be commercially deployed as shown in Figure 1.2. This section introduces the four key integration issues examined within this thesis: harsh environment survivability, temperature stability, strain transfer, and encapsulation. An overview of the problem with general strategies to solve the issue are provided.

1.3.1 Harsh Environment Survivability

The chief advantage of making harsh environment MEMS sensors is the ability to place them directly in environments previously inaccessible to standard sensors. Some proposed locations include engines for single cylinder monitoring [29, 30] and aircraft [31]. The key to making this transition with traditional MEMS lies in changing materials from silicon to ones suited to harsh environments. Early on, silicon carbide was proposed and has since been used in harsh environments due to it's excellent material properties [32].

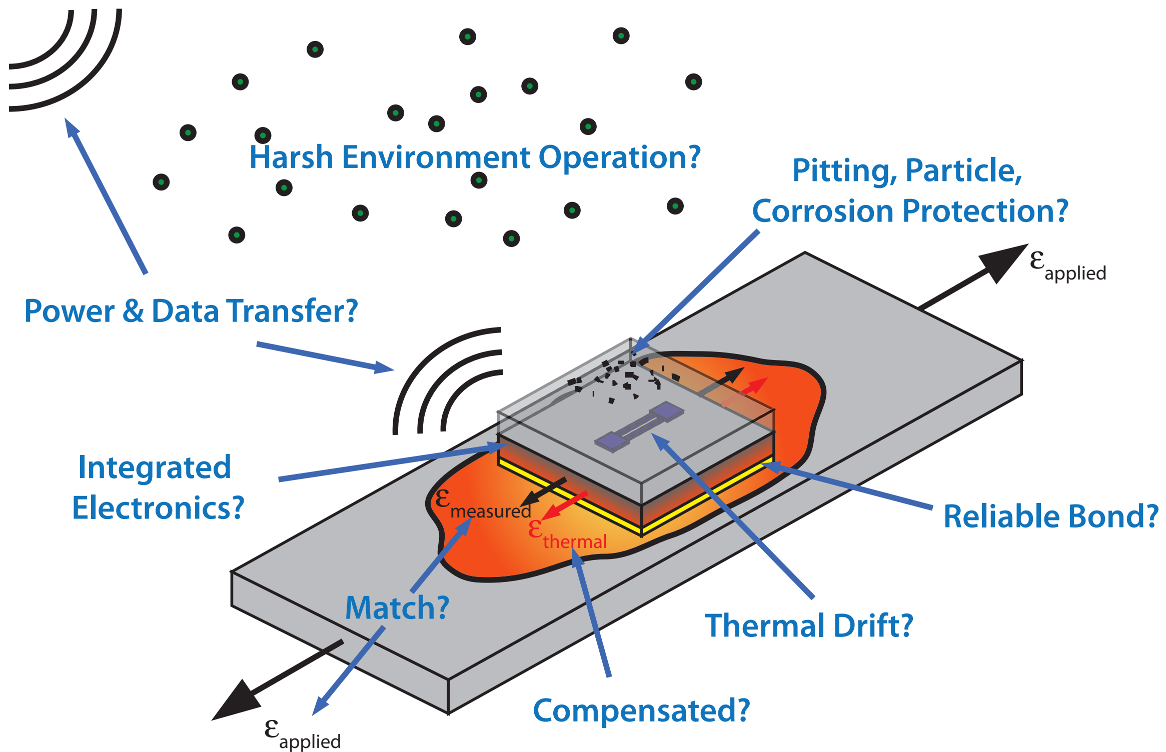

Figure 1.2. Once a strain gauge has been successfully demonstrated, a number of issues still need to be resolved before the gauge may realistically be used for any commercial purposes.

Silicon carbide has a high bandgap and is mechanically stronger and more stable with temperature when compared to silicon. However, processing constraints such as sidewall angle, deposition rate, and etch times limit device dimensions. Furthermore, to characterize the completed device, unique testing setups need to be designed. Cost is also currently an issue for SiC processing, especially with regard to the substrates, however, this is expected to become less of an issue as the technology matures.

This thesis builds on the design work of Azevedo [3], and presents a MEMS strain gauge which survives 600°C and 64,000 G, without sacrificing sensitivity and resolution-bandwidth. In Chapter 2, details of the device fabrication, and high temperature high shock testing are presented. Ultimately, it is shown that MEMS strain gauges can use different materials to enable high temperature, high shock, harsh environment operation. However, with the processing constraints in mind, the sensitivity and resolution bandwidth are maintained.

1.3.2 Temperature Stability

The temperature stability of DETFs is dependent on changes in the Young's Modulus with temperature. As temperature increases, the Young's modulus tends to decrease, with

the noted exception of silicon dioxide. Several methods for dealing with this effect have been researched previously, and are discussed more fully in Chapter 3. Both active techniques involving multiple resonators and passive techniques using creative mechanical structures can be employed. However, these techniques can change the strain sensitivity of the device and performance characteristics.

This thesis specifically explores a newly discovered passive temperature compensation method which simply uses a different substrate material from the device layer. The CTE mismatch between the device layer and substrate induces thermal strains which cancel the modulus of elasticity changes. Chapter 3 provides the needed design equations, discusses this new technique in light of other materials, and presents experimental evidence showing reduced temperature sensitivities.

1.3.3 Bonding & Strain Transfer

Since MEMS devices are fabricated on silicon substrates, a key issue to resolve is bonding this silicon to a number of different surfaces, especially metals. Sosnowchik has addressed a number of these issues [33, 34], and was able to find a relatively low temperature, rapid method way to bond silicon dies to steel. This method proved that blank substrates could be bonded, and survive high strains up 2000 microstrain with no bond fatigue after thousands of high strain cycles. In this work, it was found that thin substrates (100 μm) had the best performance in terms of bond fatigue and ultimate strain.

However, attaching a silicon die to a surface also has the effect of changing the localized strain field in the test object. Azevedo was able to perform an extensive numerical analysis for strain transfer in silicon dies attached to steel parallels of varying thicknesses [35]. Briefly, it was found that both the ratio of the silicon die thickness to silicon length and the ratio of the die thickness to steel object thickness determined the strain transfer. In axial conditions, the die tends to locally stiffen the area of measurement, reducing strain sensitivity. However, for bending conditions, the die will increase the sensor's distance from the neutral axis of the measurement object. As such, it is possible to actually amplify the strain experienced by the object.

Building on the work of Azevedo and Sosnowchik, this thesis examines how to modify and measure strains on round objects in Chapter 4. Specifically, strain is measured on a static halfshaft, the stiff metal component joining the differential and wheel of a passenger automobile. This system has great potential given the ability of the gauge to measure very small applied strains, such as those experienced during normal driving and maneuvering. This work includes a discussion of bonding to circular objects, and the effect of modifying such objects, and the systems level analysis needed to understand the strain transfer to the gauge. Finally, this work demonstrates the first high strain measurements using a MEMS DETF strain gauge, up to 1000 microstrain.

1.3.4 Encapsulation

Strain gauge encapsulation is required to meet all of the demands placed on traditional encapsulation. The encapsulation must protect the device from dirt and particulates, and from changes induced by the environment (such as humidity). Furthermore, the MEMS device itself is fragile when directly touched, so the package must protect the device from harm. Also, the package should be able to survive the same conditions that the device it is protecting can survive or more. For example, if the tuning fork is capable of surviving a shock of 100,000 G, the package should similarly be able to survive this shock.

For MEMS devices which are also being used as strain sensors, additional constraints exist on the encapsulation. First, the encapsulation itself must be compact and compliant such that it does not locally reinforce the sensing area, similar to the problems discussed in 1.3.3. Second, the packaging must be able to directly transfer strain from the sensing surface to the device. One possible implementation of this might be a wafer level encapsulation with a solder placed directly on the underlying silicon surface. Depending on the bonding method chosen, the device must occasionally withstand direct pressure which occurs during the bonding process or an injection molding process.

Finally, for the case of double ended tuning fork, the encapsulation should not shift the resonant frequency of the device. Most wafer level encapsulation options include a sealing step which applies material to the tuning fork, changing the fundamental resonant frequency. In chapter 5, designs and preliminary results for a novel encapsulation method using ion beam deposited silicon carbide are presented.

1.4 Remaining DETF Issues

While this thesis does address several key DETF integration issues, several still remain, including thermal strains, power, and data transfer. However, these are well known issues which have been examined by other research groups as well. In this section, the issues are explained and key research in this area and the relation to the DETF is mentioned. By combining the work in this thesis with some of the ideas mentioned below, a fully deployable MEMS DETF strain gauge becomes a potential reality.

1.4.1 Thermal strains

Thermally induced strains plague all strain sensors which have a coefficient of thermal expansion (CTE) mismatch with the measurement surface. Often, this problem is dealt with by trying to match the sensing device CTE with that of the sensing surface. For example, when ordering metal foil gauges, it is possible to specify the desired coefficient of thermal expansion. However, most MEMS strain gauges are fabricated on semiconductor surfaces,

which tend to have coefficients of thermal expansion around 2-4. Unfortunately, most metal surfaces have coefficients of thermal expansion above 10, and as high as 30 (zinc). As such, roughly 8-25 $\mu\epsilon$ can be induced with each degree. These thermal strains are indistinguishable from mechanical strains, so removing them is challenging.

Most of the techniques which have been developed to date rely on clever strain gauge deployment. The general idea is that temperature tends to be a global phenomenon, uniformly affecting all strain gauges, while mechanical strains tend to be more local. Also, these deployment techniques rely on some apriori knowledge of the expected failure mode. For example, consider a cantilever with strain gauges mounted such that when the cantilever is placed in bending, one gauge will measure tension and one will measure compression. Both gauges will have a CTE mismatch to the substrate, so changes in temperature will affect both gauges equally. By using a differential signal, the CTE mismatch is effectively cancelled out. However, in such a case, the gauges are now susceptible to making a measurement error when the beam is pulled on axially.

Another option is to bond a dummy gauge to an area of a component which is not experiencing mechanical strain. Expanding upon that idea, a dummy gauge could simply consist of a MEMS device bonded to a thin piece of metal which is the same composition as the measurement surface. For the case of a MEMS tuning fork, this dummy gauge would actually be quite small and unobtrusive. More work is needed to solve this problem in a definitive manner. However, given that direct bonding of MEMS DETF strain sensors has just been achieved [36], additional research in this area is warranted.

1.4.2 Power & Wireless Data Transfer

Aside from a repeatable way to deal with thermal strains, these issues are the last remaining barrier which prevents wide scale deployment of MEMS DETF strain gauges. Power is needed for sense electronics and to resonate the tuning fork. Ideally, the power supply will be small such that it will not drastically change the dynamics of moving systems when attached to them. Some researchers have examined using energy scavenging for this area, but more work will be necessary to lower the power requirements of the DETF electronics and to raise the power generated from scavenging. Other approaches include small scale batteries [37], nuclear scavenging [38, 39], thermoelectric generation [40], and remote power [41]. All of these technologies are at varying stages of development, and need additional work to be considered a mature technology.

Once bonded to the substrate, a method of getting data out of the gauge is needed. Since strain monitoring will most likely be examining many points on a given structure, or on moving and rotating components, a wireless solution may be the only way to realistically implement such a system. This system will need to be carefully planned to manage tradeoffs between the amount of information being transmitted and the power available for the system. The previously mentioned remote powering scheme also has an integrated wireless solution [41], which achieves sub-microstrain resolution in a 10 kHz bandwidth.

1.5 Concluding Remarks

Strain gauges are more difficult to implement than other MEMS gauges because measuring strain requires that the MEMS be in direct contact with the measurand surface. The measurand surface itself can influence the behavior of the gauge, causing erroneous readings. The ideal gauge must only measure mechanical strain, but remain stable, and be sensitive enough to measure very small strains. Aside from large equipment, the primary drawback for the other strain sensors is either low strain sensitivity, or high temperature sensitivity.

Since DETFs have a number of inherent advantages compared to other strain sensors, this thesis focuses on addressing some of the integration issues introduced in coupling these gauges to real world objects. Specifically, this thesis will consider harsh environment survivability, temperature stability, strain transfer, and encapsulation. It is important to keep all strain gauge issues in mind when designing, such that design changes to address one issue, such as harsh environment survivability, do not adversely effect other issues, such as temperature stability. Other issues such as thermal strains, power, and data transfer have been effectively addressed by other groups mentioned previously. Each of the following chapters will address the issues presented, and provides design ideas that do not influence the other aspects of the gauge. When combined into a single design, the solutions presented in this thesis could lead to a fully deployable MEMS DETF strain gauge for commercial use.

Chapter 2

Harsh Environment Strain Gauge

2.1 Silicon Carbide DETF and Uses

This chapter describes the fabrication and testing of a silicon carbide (SiC) MEMS double-ended tuning fork (DETF). Beginning with the design described by Azevedo [3], an alternate material set is used to enable high temperature, high shock operation. Being mindful of processing constraints, the SiC tuning fork is shown to have the same strain sensitivity and resolution bandwidth of comparable silicon double ended tuning forks. However, using previously described [42] and novel testing apparatuses, this chapter elaborates on some of the first high temperature testing at 600°C and high shock testing above 50,000 G previously described in [4]. Additionally, this chapter also reports on lower than expected quality factors for these devices.

Silicon carbide is used in for MEMS harsh environment sensors because SiC has attractive thermal, chemical, and mechanical stability at elevated temperatures as well as a large bandgap suitable for high temperature electronics [32]. When compared to traditional MEMS materials, such as silicon, SiC has a higher fracture toughness [43], which allows for the creation of MEMS devices able to survive higher shock events. Furthermore, silicon carbide has a higher Young's modulus (E) than silicon, reducing the deflection of device layers experiencing high G load forces.

SiC MEMS sensors and actuators have potential applications in a variety of harsh environment situations. For example, SiC sensors have operated in corrosive high temperature environments such as those experienced in automotive engine exhaust [44] and those found inside engine cylinders [29]. In addition, sensors have been designed to survive high shocks (>60,000 G) such as those found in avionic, space, and military applications [45]. Since SiC sensors and electronics may operate at high temperatures (500°C) [46], there is no need

for active cooling systems to ensure operation, saving weight in critical avionic, hybrid and electric automotive applications [47].

Besides being useful for strain sensing, tuning forks may also be used to create other sensors. Combining the tuning fork structure with a proof mass allows for the creation of an accelerometer [48] or gyroscope [27]. By placing a tuning fork on a diaphragm, one can create a pressure sensor [49, 50]. Alone, the double ended tuning fork also be used as a temperature sensor [51]. The versatility of the DETF is further improved when combined with a square wave oscillator circuit, allowing for high resolution operation at atmospheric pressure [5].

2.2 Device Structure and Fabrication

2.2.1 Extending Device Survivability to 600°C

The resonator structure and principle of operation has been presented in detail by Azevedo *et al.* [3]. A conceptual schematic of the device is shown in Figure 2.1A. It features a central node comb drive configuration which minimizes torque applied to each tuning fork during shock events. However, the increased transduction area of a comb drive is maintained, which improves strain resolution.

The previously reported process flow has been modified in this work to include key changes to improve the ability of these devices to withstand higher temperature, harsh environment operation. First, the routing layer is now created from silicon carbide to improve corrosion resistance. Second, the low-temperature oxide (LTO) insulation layer is seen as a potential failure point under high thermal cycling as well as in a corrosive media. Therefore, the LTO is replaced with a thick LPCVD low-stress silicon nitride (LSN). LSN is more corrosion-resistant than oxide, and is used as protective coating by the IC industry and an etch mask for KOH etching. Moreover, LSN has higher thermal conductivity than oxide and its thermal coefficient of expansion (TCE) is significantly closer to SiC than oxide. These changes reduce the thermally induced stress mismatch between layers and improve the oxidation resistance, providing a strain sensor capable of working at 600°C. The material properties of different thin films are summarized in Table 2.1. The aforementioned changes will also accelerate the future transition of this device from Si substrate to SiC substrate, creating an all-SiC sensor.

The modified stack structure is shown in Figure 2.2. It has several characteristics which could be useful to the designer in creating other structures. It is readily adaptable to a variety of fabrication situations, and includes an electrical feedthrough layer to allow for the creation of more complicated and compact MEMS structures. Diaphragms, proof masses, and encapsulation layers can be incorporated into the existing structure with minimal changes. The maximum thickness of the poly-SiC device layer is limited by the selectivity

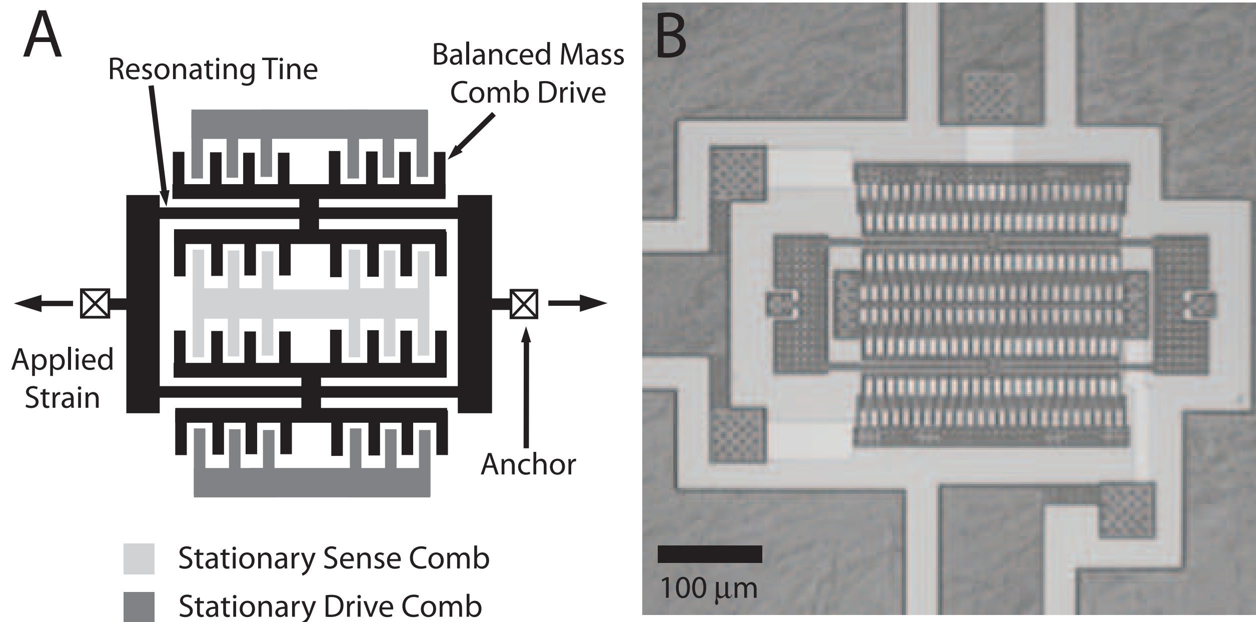

Figure 2.1. A) Conceptual schematic of a Balanced Mass Double Ended Tuning Fork (BDETF) featuring a central node comb drive B) Optical Micrograph of BDETF

Table 2.1. Material properties of different films [43, 52, 53]

	4H-SiC	Poly-SiC	Poly-Si	LSN	SiO_2
Dielectric Constant	9.66	9.72	11.7	7.5	3.9
Dielectric Strength (10^6 V/cm)	3.5	3	0.3	6.5	13
Young's Modulus (GPa)	448	340	160	290	57
Thermal Conductivity (W/cm-K)	4.9	3.2	0.35	0.15	0.01
Thermal Coefficient of Expansion (ppm/K)	4.2	2.9	2.8	3	0.5
Thermal Coefficient of Young's Modulus (ppm/K)	-	-51	-64	-	-
Fracture Toughness (MPa $m^{1/2}$)	-	2.9	0.8	-	-

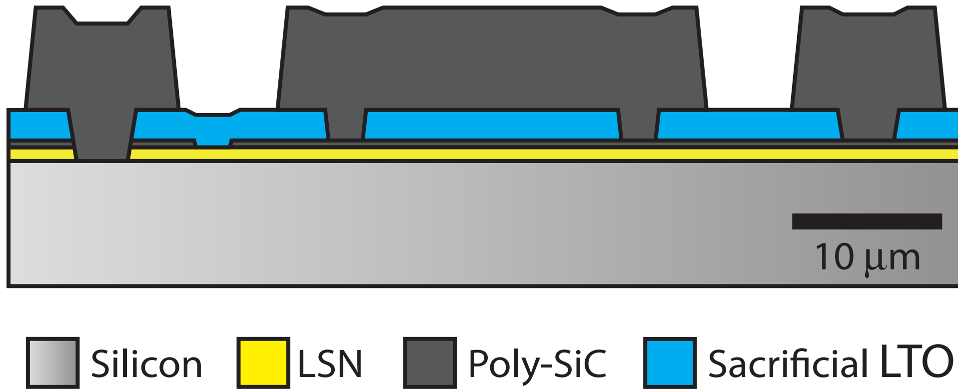

Figure 2.2. Process flow cross section before sacrificial oxide release

and sidewall angle of the etching process used. The minimum thickness is determined by the desired strain resolution, since the thickness is proportional to the motional current passing through the MEMS.

2.2.2 Etching Considerations

The design of SiC MEMS structures is similar to silicon, but there are some subtleties in regards to etching. Etching can be difficult because current CMOS compatible masks, such as silicon dioxide and silicon nitride, experience a selectivity, sidewall angle, and etch speed tradeoff [54, 55]. Recent results using aluminum nitride have been promising, but have not been demonstrated on poly-SiC films [56]. The sidewall tradeoff can be especially difficult when dealing with intricate structures such as comb-drives, which need narrow gaps for high performance. Also, it should be noted that since silicon optimized equipment was used, etching of whole four inch wafers was not possible. While performing etch optimization recipes for the BDETF, it was discovered that changing etch parameters such as pressure, gas ratio, and power had little effect on the actual etching, it was all bad. When individual dies were etched instead, the results closely matched the published literature [54]. In this particular case, 7 μm represented the maximum thickness which could be achieved for 2 μm comb drive gaps. Greater thickness would have been preferable as it improves shock resistance [3] and improves the signal coming from the device.

The stack used to create this tuning fork begins with a 100 mm diameter n-type <100> silicon wafer and LSN (1.3 μm) is deposited by LPCVD. The first mask is used to pattern the thick LSN layer using Lam Autoetcher 590 to provide electrical contact to the substrate. Subsequently, in-situ nitrogen-doped poly-SiC (300 nm) is deposited by LPCVD using an optimized recipe for achieving an acceptable film residual stress (300 MPa tensile) and low resistivity (~0.025 Ω-cm) [57]. The poly-SiC layer is patterned to form the electrical routing layer. Then, a thick LPCVD LTO (2 μm) is deposited and annealed at 950°C for 1 hour to

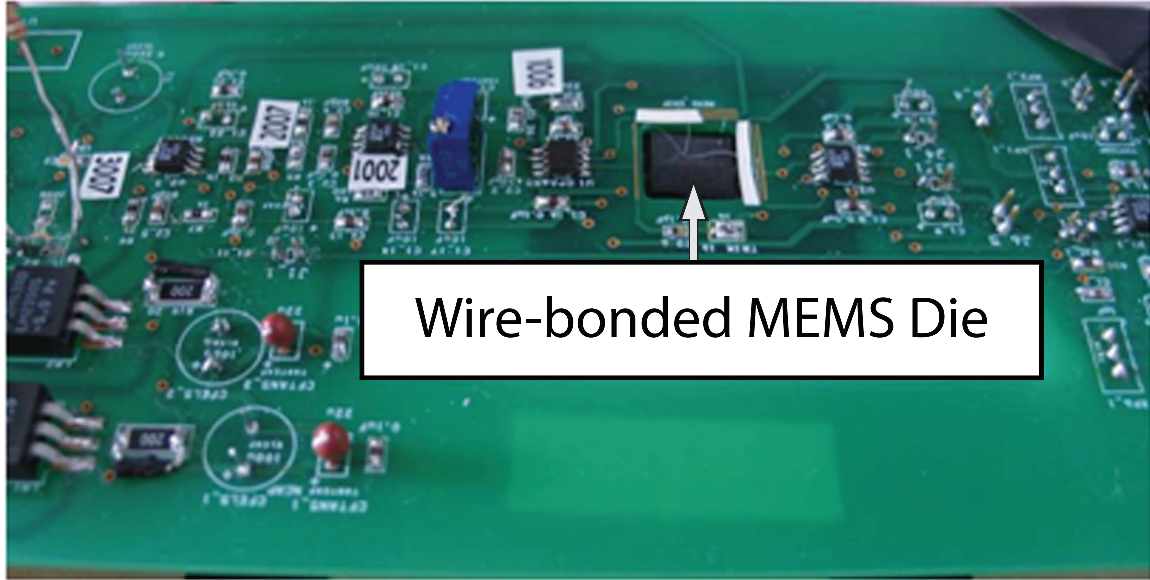

Figure 2.3. Oscillator Board with senor die attached (some electronic components are beneath the board)

serve as the sacrificial release layer. Anchors and electrical contact points are then patterned on the LTO using a Lam Autoetcher 590. Afterward, thick poly-SiC (7 μm) is deposited by LPCVD at Case Western Reserve University using the process described in [29], and patterned using LTO as the etch mask to form the resonator structure. Finally, the etch mask and sacrificial oxide are removed in vapor hydrofluoric acid to release the resonator structure.

Patterning of all the poly-SiC films in the fabrication process is performed with plasma etching in a commercial LAM Transformer Coupled Plasma (TCP) 9400 system, using an etch vapor mixture of HBr (125 sccm) and Cl_2 (75 sccm). The TCP forward and bias powers used are 300W and 150W respectively, while the chamber pressure is kept at 12 mTorr for optimized etch selectivity and sufficient etch rate [54]. The final fabricated device is shown in Figure 2.1B. Thicknesses of deposited thin films are measured using a Nanospec 4000 AFT Spectrophotometer and confirmed by cross-sectional scanning electron microscopy (SEM). Resistivity values are obtained using a Tencor RS35C 4-Point Probe.

2.3 Test Setup and Characterization

2.3.1 Strain Sensitivity, Strain Noise, & Quality Factor

The fabricated devices are wire-bonded onto a square-wave oscillator (SWO) board shown in Figure 2.3, which is able to drive the BDETF into resonance in air despite the presence of large feed-through capacitance. The oscillator design is detailed in Reference [5]. The strain sensitivity of the sensor is characterized using an on-chip electrostatic actuator. The electrostatic actuator applies axial force to the BDETF which can be equated to an applied strain. The strain resolution of the senors is computed from phase noise data, measured using an Agilent E4440A Spectrum Analyzer.

The quality factor as a function of pressure was measured in a vacuum chamber modified with electrical feedthroughs. To make these measurements, a different board was used. The square wave oscillator board mentioned above worked well in air, but under vacuum conditions, mechanical spring stiffening was observed. Instead, the tuning fork was wirebonded to a small pcb board, containing two LF353 amplifiers. One was configured as a unity gain buffer, and the other was configured as a transimpedance amplifier with a gain of 10,000, as detailed in [58]. To modify the board to accept a larger die size, a razor blade was used to scrape the appropriate traces for signal in and out on the board. These scraped traces could then accept a wirebond.

2.3.2 High Temperature Testing

For the temperature testing, a specialized high temperature test setup that locally heats the fabricated device up to 600°C in air was constructed and is shown in Figure 2.4, as described in [42]. This setup allows for the testing of the SiC BDETF with well known, well characterized silicon electronics shown in Fig 2.3. An IR lamp (SpotIR Model 4085, Research, Inc.) is placed underneath the oscillator board with the focal point targeted on the backside of the die. A heat shield consisting of a steel plate and wood is added to prevent scattered radiation of the IR lamp from warming the silicon electronics. Also, a piece of Fiberfrax® insulation is placed between the heat shield and PCB. The fiberfrax has a hole drilled in it to allow some light to pass through to the die. The hole was cut such that it prevented scattered radiation from hitting the board, but still mechanically supported the die during wire-bonding. To extend temperature testing time, a heat sink created from square brass tubing was attached to the PCB with copper tape. During experiments, compressed air is blown in the square tubing at 550 kPa to cool the silicon electronics. Before testing MEMS dice, the setup was calibrated using a blank silicon die and thermocouple.

Dice are heated to various temperatures for approximately 100 seconds at a time, both with and without steam. Steam was used to accelerate potential oxidation at the elevated operating temperature. After 100 seconds, the signal from the square wave oscillator was

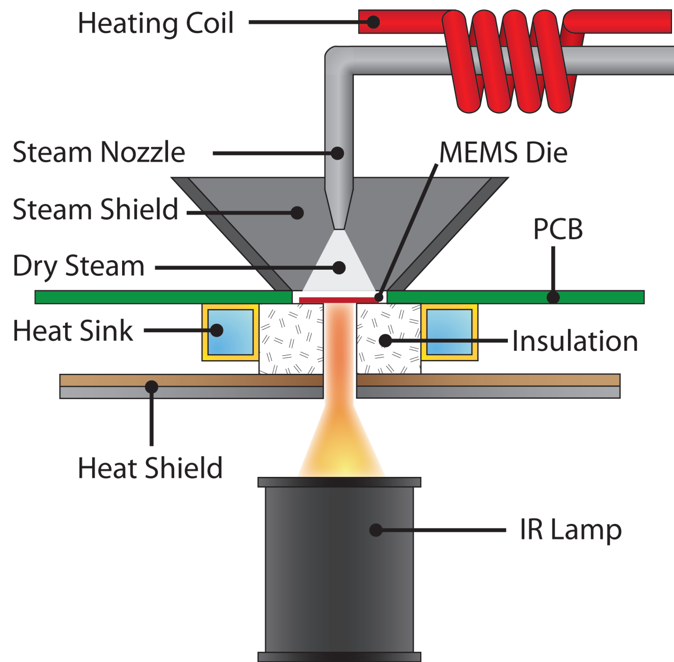

Figure 2.4. Schematic of High Temperature Heating Setup

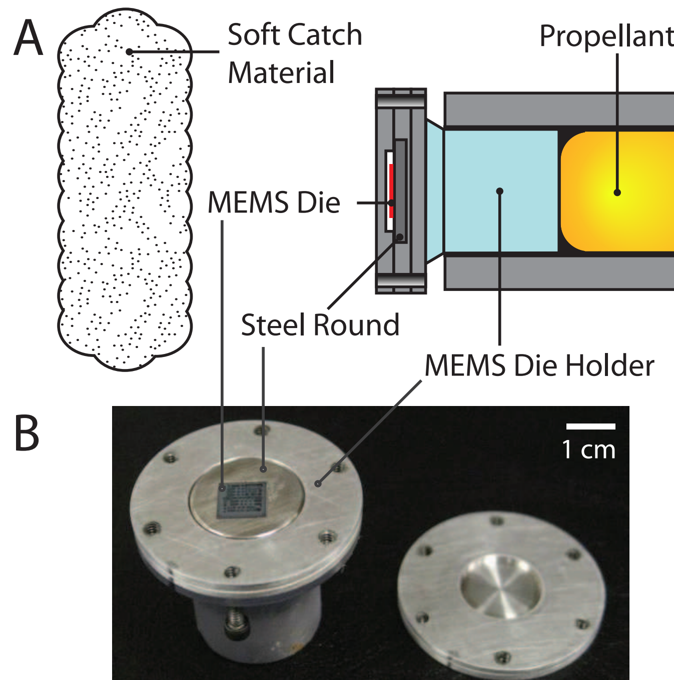

Figure 2.5. A) Schematic of G-shock light gas gun system B) Specialized MEMS die holder for use in light gas gun system with bonded MEMS die

lost. This could be due to the oscillator electronics being pushed out of tolerance, but after sufficient cooling, the board would begin working again. For the steam tests, the dice were allowed to heat up to 600°C (approximately 40 seconds) before applying dry steam. The dry steam was directed towards the MEMS die using a nozzle. Steam was created using a Top Innovations model SF-290 Multi-Purpose Steamer. The steam was routed through copper tubing into a heater coil which was kept at approximately 300°C to ensure that only dry steam is present around the device. Wet steam could with water droplets could cause the device to stop working. A steam shield consisting of additional insulation was constructed to protect the PCB from steam.

2.3.3 Shock Testing

For the shock testing, two samples were bonded to steel rounds using Vishay MBond 610 strain gauge epoxy. Once bonded, images of the dice and individual devices were taken to document the pre-shock condition of the sensor. The steel rounds were placed in a specialized testing holder used in conjunction with a light gas gun system at the Aerophysics Research Center located at the University of Alabama, Huntsville. Shock was applied to the dice using a hard-launch, soft-catch method, in which the dice were rapidly accelerated while leaving the gas gun and landed on soft padding. A schematic of the light gas gun system and MEMS die holder is shown in Figures 2.5A and 2.5B, respectively. Acceleration data was determined by examining sub-millisecond high speed video of the shock event and correlating distance and time data to acceleration. Images of the devices were taken after exposure to G-shock and operation was tested by attempting to resonate the device.

2.4 Results

2.4.1 Phase Noise

Several dice were taken from different locations on multiple wafers for testing. The poly-SiC BDETFs without the on-chip electrostatic actuator have resonance frequencies between 196 and 207 kHz in air. The variation in resonance frequency is attributed to the non-uniformity of thin film deposition and etching variation. The sensitivity of the BDETF resonant frequency to applied strain is measured to be 66 Hz/$\mu\varepsilon$ using the techniques described in [3]. The phase noise density is measured at room temperature and is used to compute the strain resolution according to Equation 2.1.

$$\varepsilon_{res} = \left(\frac{\partial f}{\partial \varepsilon}\right)^{-1} \sqrt{f_{res}^2} = \left(\frac{\partial f}{\partial \varepsilon}\right)^{-1} \sqrt{\int_0^{BW} \phi(f_c) df_c} \qquad (2.1)$$

where f_c is the carrier offset frequency, BW is the bandwidth of interest and ϕ is the measured phase noise density [59]. Figure 2.6 shows measurements of the strain resolution as a function of both film thickness and bias voltage.

With the bias voltage set to 80V, the measured strain resolution is 0.045 $\mu\varepsilon$ at a bandwidth of 10 kHz. This is comparable to the state-of-the-art silicon comb-drive DETF strain sensor [5]. However, implementing this high voltage in conjunction with application specific circuitry could be difficult, so the strain resolution for other voltages was tested as well.

For this particular device, the range of bias voltages was limited between 40V and 80V. Below 40V the motional current was too low for the oscillator circuit to work properly. Above 80V the electrostatic combs exhibit snap-in behavior. Decreasing the bias voltage reduces the motional current passing through the MEMS, and therefore reduces the strain resolution of the oscillator circuit. However, at 40V the BDETF is still capable of resolving 0.2 $\mu\varepsilon$ in a 10 kHz bandwidth.

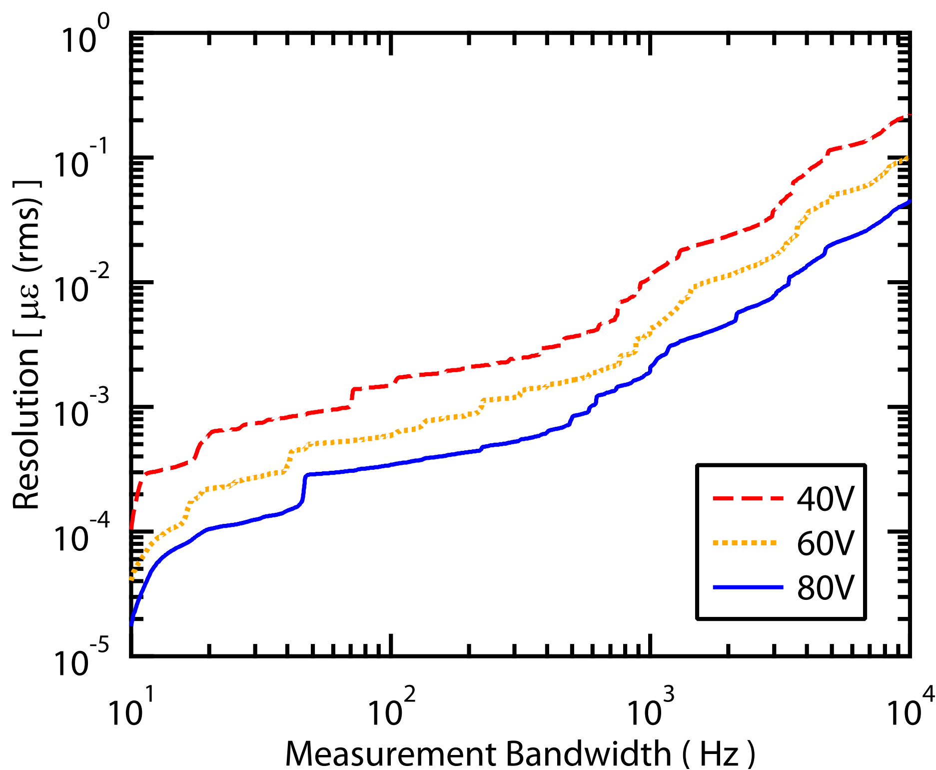

Figure 2.6. Strain resolution as a function of measurement bandwidth and bias voltage (Data taken at room temperature).

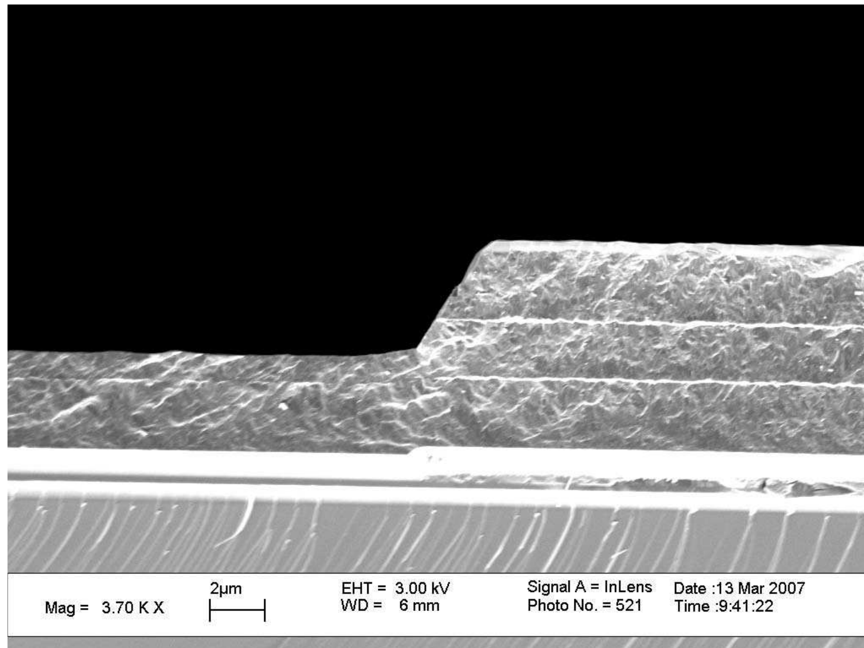

Figure 2.7. The three layers of SiC used to achieve 7 $\mu\epsilon$ are clearly visible here. Also, it is noted that a great deal of texture can also be seen in the layers, indicating a large grain size.

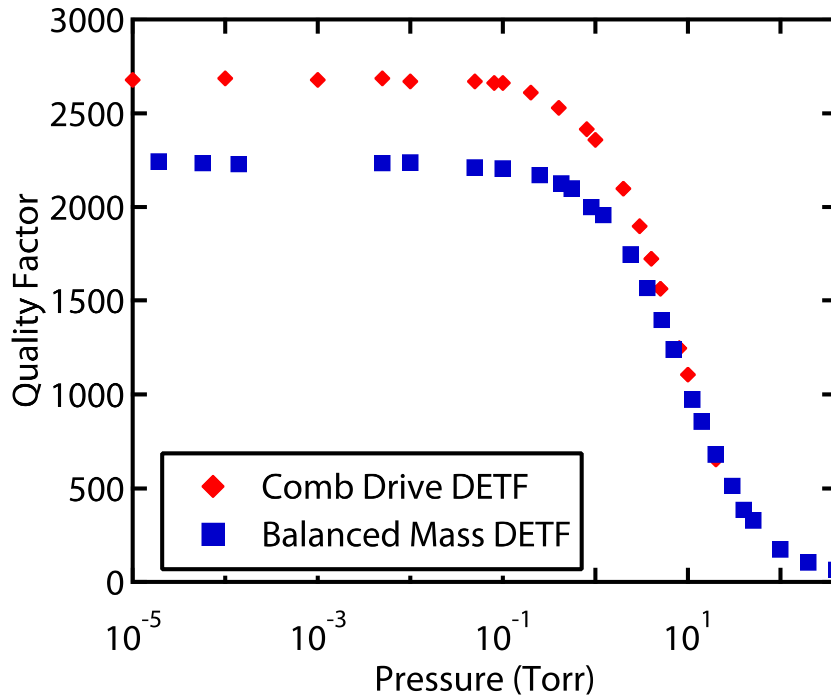

Figure 2.8. Quality factor of BDETF and completely different device with varying geometry. The low quality factor appears to be related to a systems level issue, such as material quality.

2.4.2 Quality Factor under Vacuum

Given the high acoustic velocity of silicon carbide, the quality factor was surprisingly low. Both the BDETF and a similar well characterized comb driven double ended tuning fork (CDDETF) were tested [5]. Both resonators showed maximum quality factors that were not limited by pressure, and were in the range of several thousand, shown in Figure 2.8. The CDDETF was a replica of a previously fabricated device, created with a 10 μm epitaxial silicon device layer. The CDDETF displayed a maximum quality factor of 25000 under vacuum, indicating that the device geometry is not the limiting factor. Also, the quality factor associated with thermoelastic damping (TED) was calculated and found to be orders of magnitude larger than the quality factors measured here.

The lower quality factor is believed to come from a combination of the slanted sidewalls, rough sidewall edges, and interface layers. The slanted, rough sidewalls which were common to this etching process can contribute to spurious modes, and the rough edges can be a source of energy dissipation. Also, the method of deposition could be contributing to energy losses in the silicon carbide layer as well. To get thicknesses of silicon carbide which are greater than 2.5 μm, it is necessary to perform several long furnace runs. In examining cross-sections of our devices, it was possible to clearly see three distinct layers with a scanning electron microscope, as shown in Figure 2.7. When cleaving devices for inspection under the SEM, occasional delamination between these layers would occur. It is hypothesized that some oxidation or layer inhomogeneity is dissipating energy, limiting the quality factor. Recent research also indicates that the grain size of a polycrystalline silicon carbide film is much more important than electrical resistivity in determining quality factor [60].

2.4.3 Temperature Sensitivity

The temperature sensitivity of this device for temperatures up to 602°C is shown in Figure 2.9. The device has a temperature sensitivity of approximately −17 Hz/°C (−91 ppm/°C) from 26°C to 600°C. When possible, devices are created from the same material as the substrate to minimize thermal strains induced by coefficients of thermal expansion mismatch. However, for these experiments, silicon substrates were used due to their substantially lower cost.

For comparison purposes to the CTE data, it is useful to calculate the expected temperature dependence for a SiC device fabricated on a SiC substrate. Assuming that a perfectly matched substrate was used, the expected temperature sensitivity would only be a function of the modulus of elasticity. In this case, using data from [53], the calculated frequency dependence is approximately −5 Hz/°C (−23 ppm/°C). Over the entire range of temperatures, the temperature sensitivity of the device is much higher. However, in examining Figure 2.9, it is noted that there is a flat region near room temperature, where changes in temperature cause little change in the frequency. This is attributed both the temperature dependence of

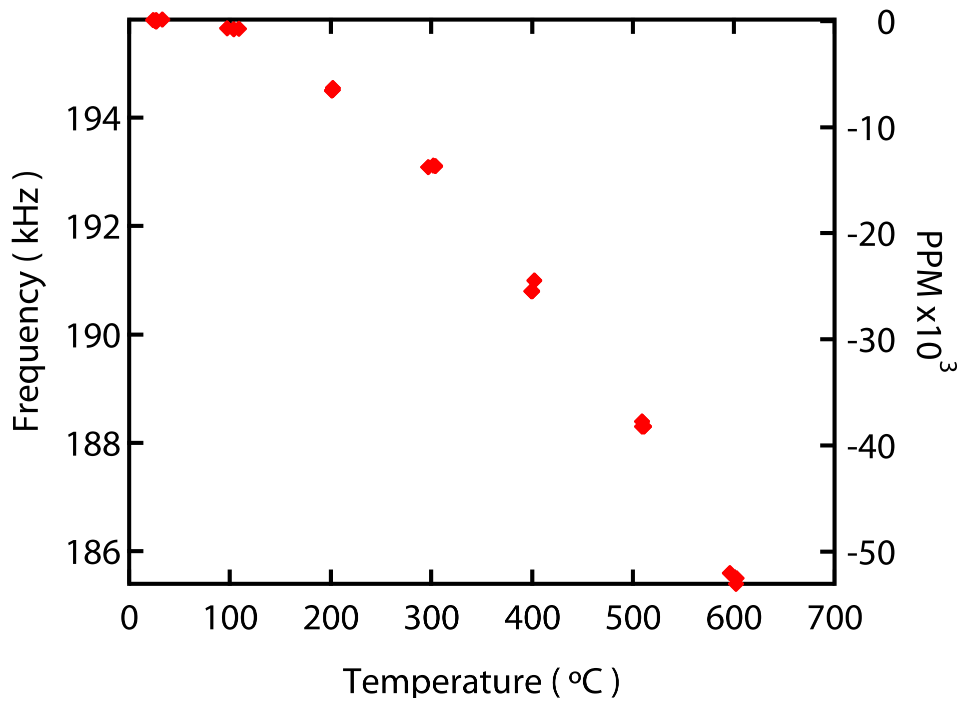

Figure 2.9. Temperature Sensitivity of BDETF

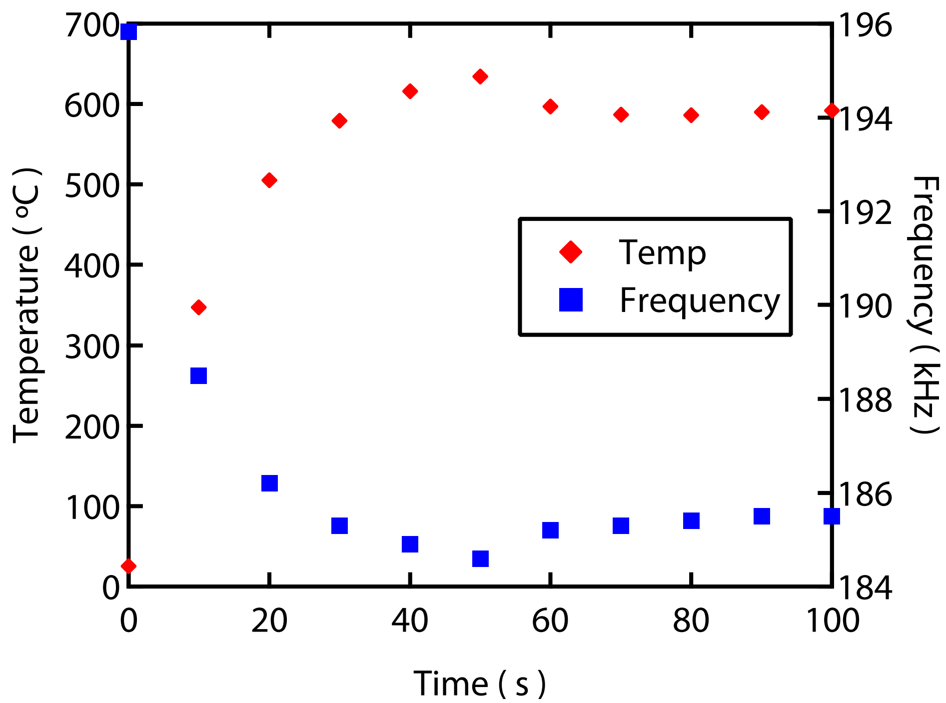

Figure 2.10. Sample Dry Steam Testing Results

the modulus of elasticity and to the coefficient of thermal expansion mismatch between the silicon substrate and silicon carbide structure. Additional details are discussed in Chapter 3.

In Figure 2.10 is shown a sample transient response curve of the BDETF in dry steam. In dry steam, the BDETF resonance frequency was 185.5 kHz at 592°C. This steady state value matched that of the same resonator without steam to within the resolution limits of this experiment. This indicates that the resonator was not oxidized, demonstrating the high temperature stability of the device.

2.4.4 Shock Testing

Example time lapse photography of the G-shock testing is shown in Figure 2.11. Videos of the shock event shown in Figure 2.11 are used to extract the position and time data shown in Figure 2.12. A superimposed line to help the reader identify the front of the MEMS die holder has been included in Figure 2.11. A fourth order polynomial curve was fit to the data. Taking the derivative twice, the acceleration on the die as a function of time was determined and is also plotted in Figure 2.12.

Visually, the BDETF pre-shock and post-shock images were identical, and looked similar to Figure 2.1B. No cracks, film delamination, or fracture was observed on or around the BDETF structure. The BDETF also successfully resonated within normal operational parameters after the shock event, indicating no damage had occurred.

2.5 Discussion

This chapter details the fabrication and testing of a MEMS SiC BDETF with a modified materials set which enables 600°C operation in steam, and survives a shock of 64,000 G. Detailed descriptions of the specialized testing equipment and customized setups are given. A high temperature testing setup is used which is capable of locally heating a MEMS chip to 600°C while using traditional silicon electronics. Furthermore, a light gas gun is used for shock testing which exceeds that which can be achieved using an accelerated drop test rig [3].

This device achieves a resolution of 0.045 $\mu\varepsilon$ in a 10 kHz bandwidth, which is comparable to previously reported silicon-based strain sensors. The current design uses a low Q tuning fork with a square wave oscillator, which is optimized to reduce phase noise in large bandwidth [5, 28]. Future devices may need higher quality factor devices, so additional work is needed to improve the quality factor under vacuum.

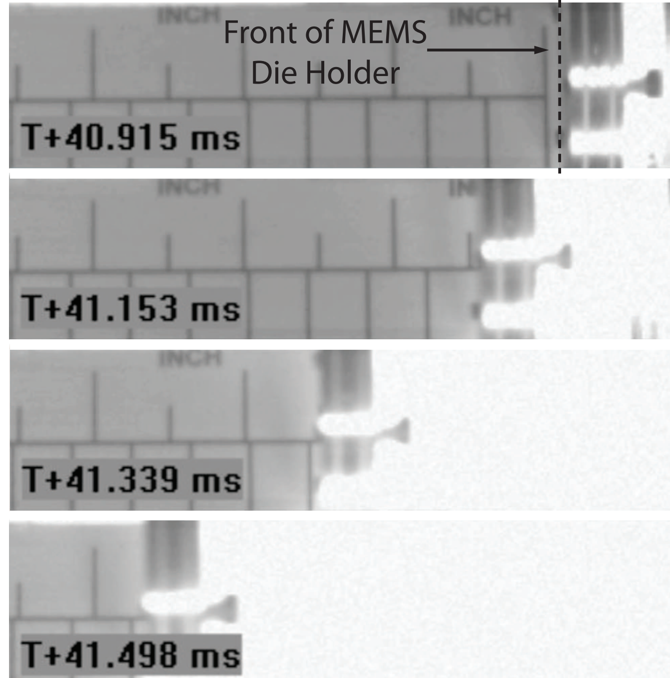

Figure 2.11. Time Lapse Photography of the Shock Event

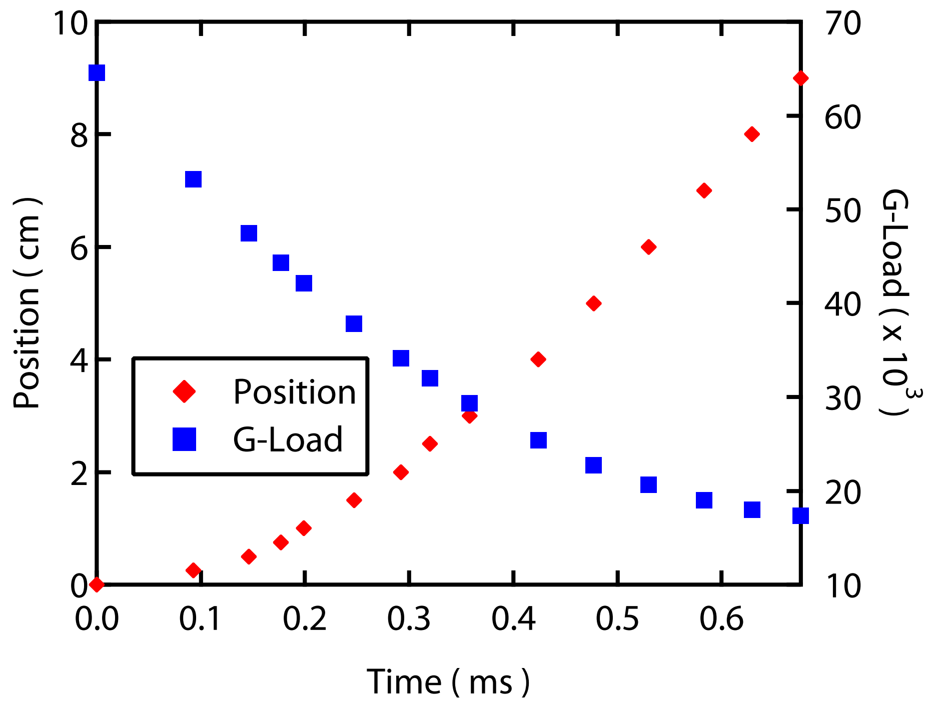

Figure 2.12. Experimental Data extracted from Time Lapse Photography

Chapter 3

Temperature Compensation

3.1 Temperature Compensation Overview & Methods

This chapter presents an analytical model for a novel temperature compensation mechanism with experimental verification. By purposely mismatching the device layer and substrate layer, thermal strains can be induced which cancel changes in the frequency due to a shift in the modulus of elasticity. Two poly-SiC double ended tuning forks (DETF) of different physical dimensions are fabricated on single crystalline substrates (SCS). The devices are tested between 5°C and 320°C, and have reasonable agreement with the model. However, the model is found to be quite sensitive to coefficient of thermal expansion (CTE) values. Before examining the analytical model itself, it is helpful to review typical device construction for temperature stability and existing temperature compensation schemes.

Typically, a DETF is constructed on a substrate composed of the same material. By doing this, the coefficients of thermal expansion are well matched between the tuning fork and substrate. As such, changes in temperature do not cause thermal strains to be induced. However, temperature compensation is still needed for tuning fork structures because the modulus of elasticity of a material also changes with temperature. These changes in the modulus of elasticity will cause the resonant frequency to shift, and in the case of strain sensors, cause erroneous readings of strain. This effect is especially detrimental in the case of timing references, and several different approaches have emerged to counteract temperature effects.

These temperature compensation methods can be divided into two categories: active or passive. Active compensation typically involves the addition of extra sensors. In the simplest form, the compensation is simply another resonator coupled to the substrate differently [61]. It is also possible to measure multiple modes [2] or quantities of the same resonator, such as

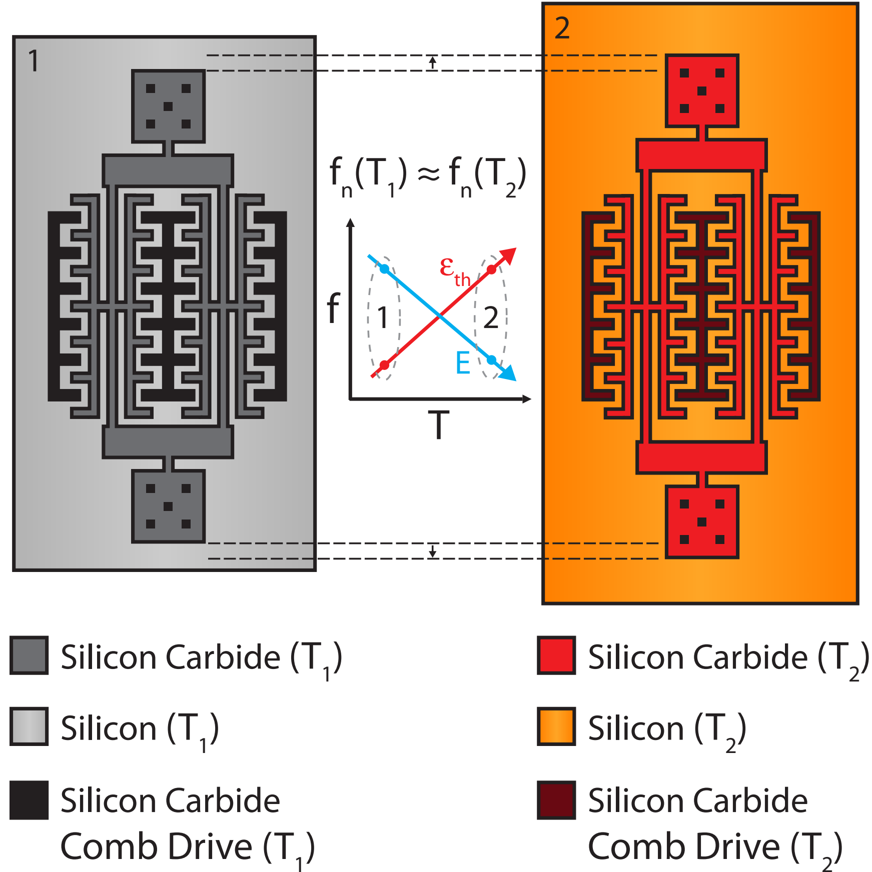

Figure 3.1. Conceptual schematic of the temperature response of a poly-SiC resonant DETF micro-extensometer on a SCS substrate near the turnover temperature. Device construction typically relies on closely matching the coefficients of thermal expansion. However, in this case, slightly mismatched coefficients of thermal expansion create tensile strain in the tuning fork, compensating the drop in the modulus of elasticity.

Q [62]. These additional measurements presumably have a different temperature dependence. By using a model of the system, the temperature-induced error can be canceled. Although these methods may produce well compensated resonators, they typically involve additional circuitry and complexity. Furthermore, active measurement techniques are not always able to eliminate large error in frequency due to temperature, thereby requiring additional passive temperature compensation techniques [63].

Passive temperature compensation methods typically rely on mechanical design to cancel out the effects of modulus changes [64], but often increase the fabrication complexity. One clever approach involves using a thin film of silicon dioxide which stiffens with temperature to cancel out shifts in silicon resonators [65]. Unfortunately, these techniques were not designed for strain sensing applications. More analysis on these areas would be needed to account how the compensation mechanism may attenuate on-axis strain or increase susceptibility to off-axis strain.

Instead, this work proposes to cancel out the modulus of elasticity change by inducing a thermal strain in the device layer by purposely mismatching the device and substrate layer. Specifically, silicon carbide (SiC) has a slight difference in CTE from silicon, which will induce tensile strain with increasing temperature. This tensile strain cancels out temperature changes in the modulus of elasticity. This technique is advantageous because it enables passive temperature compensation without degrading the mechanical strain coupling of the tuning fork to the substrate (Figure 3.1). Furthermore, design equations for the strain sensing properties of the tuning fork are simpler since they involve just one material.

3.2 Analytical Model

The following analysis considers the case of a DETF which is sensitive to temperature. Beginning with the equation for a fixed-fixed beam, the frequency for a DETF as a function of geometry, material properties, and strain is determined. The modulus of elasticity and thermal strains are identified as the key parameters which can be changed with temperature. Both are explored in further detail with a discussion of the existing experimental data for each. Afterwards, physical insights are discussed to give the reader a more intuitive understanding of the mechanism. Also discussed is the turnover temperature, where the linear temperature coefficient of the frequency equals zero [65]. This section concludes with a brief discussion of methods to estimate this point and methods to tune this temperature.

3.2.1 Frequency of Fixed-Fixed Beam with Trapezoidal Cross Section

The analysis begins by solving for the tuning fork frequency dependence on geometrical properties, material properties, and induced strain. Later in the analysis, all temperature dependent properties and thermal strains will be incorporated into this equation. This section specifically considers the case of a tuning fork with a trapezoidal cross-section. This is needed since many existing compatible silicon carbide etching processes tend to create sloped sidewalls [54, 3]. The analysis starts with the Bernoulli-Euler governing differential equation for a fixed-fixed beam subjected to an axial force:

$$\frac{\partial^2}{\partial x^2}\left(EI_xz\frac{\partial^2 u}{\partial x^2}\right)+\beta\frac{\partial u}{\partial t}+\frac{\partial}{\partial x}\left(F\frac{\partial u}{\partial x}\right)+\rho A\frac{\partial^2 u}{\partial t^2}=-P(x) \tag{3.1}$$

where u is deflection in the y-diretion, E is the elastic modulus, I_{xz} is the moment of inertia of the beam, β is the damping coefficient, F is the axial tension in the beam, ρ is the density of the film, A is the cross-sectional area of the beam, and P is the transverse force applied to the beam. The natural frequency is found by solving using the Rayleigh-Ritz method,

as described by Azevedo [66]. The interested reader is directed to [25, 24] for additional details. In this case, the fixed-fixed beam frequency equation for a beam with trapezoidal cross-section vibrating along the width of the cross-section is:

$$
\begin{aligned}
f &= \frac{1}{2\pi}\sqrt{\frac{198.6EI_{xz} + 4.85EAL^2\varepsilon}{L^3(0.397\rho AL + m_c)}}, \\
I_{xz} &= \frac{h}{48}(w_a + w_b)(w_a^2 + w_b^2), \\
A &= \frac{h}{2}(w_a + w_b).
\end{aligned}
\tag{3.2}
$$

Here m_c is the mass of the sense and drive comb arrays and w_a and w_b are the upper and lower widths of the trapezoidal beam, respectively. In examining 3.2, the main terms which can be affected by temperature are the modulus of elasticity (E) and the strain (ε). The density, ρ, also tends to decrease with increasing temperature. But this effect is significantly smaller than the change in Young's modulus with temperature. So, it can be ignored with little loss in accuracy. Likewise, possible softening of the substrate with temperature is ignored because its cross-sectional area is approximately 10^5 times that of the tines.

3.2.2 Modulus of Elasticity of Silicon Carbide

Pozzi *et al.* [53] experimentally determined the Young's modulus dependence of poly-SiC on temperature as shown in equation 3.3. The films used in this experiment were obtained from the same lab as Pozzi, so the films are expected to be similar.

$$
\begin{aligned}
E(\theta) &= E_0\left(\eta_0 + \eta_1\,\theta + \eta_2\,\theta^2\right), \\
\eta_0 &= 1.0134, \\
\eta_1 &= -4.1 * 10^{-5}, \\
\eta_2 &= -1.3 * 10^{-8}
\end{aligned}
\tag{3.3}
$$

where E_0 is the Young's modulus at room temperature.

One of the chief difficulties with microfabricated devices is determining the exact modulus of elasticity and initial strain. The range of silicon carbide values can be as low as 295 GPa [53] to as high as 448 GPa [67]. In this study, there are two separate tuning forks, with different geometrical dimensions. Given the two known resonant frequencies at room temperature, it is possible to use equation 3.2 to solve for the modulus and initial strain. In other words, using equation 3.2 twice, once for each tuning fork, E and ε may be calculated. In performing this calculation, the room temperature frequencies are used, and zero thermal strain is assumed.

The modulus of elasticity is calculated to be 298 GPa, and the initial strain is estimated to be 419 $\mu\varepsilon$ (equivalent to 125 MPa). The modulus of elasticity matches well with

340 ± 45 GPa measured by Pozzi. The initial stress is 125 MPa, which is a bit lower than the 200 MPa ± 25 MPa, but is likely due to processing improvements. Also, by taking the derivative of 3.2 with respect to strain, the sensitivity of the BDETF is estimated as 80 Hz/$\mu\varepsilon$. This compares well to the measured sensitivity of 75 Hz/$\mu\varepsilon$ [3]. To get the measured sensitivity, it is important to scale the previously reported value by the new modulus value, since this number is calculated based the estimated value of the modulus of elasticity.

3.2.3 Mechanical & Thermal Strain

For a doubly-anchored DETF resonator, the relevant strains are

$$\varepsilon = \varepsilon_0 + \varepsilon_m + \varepsilon_{th} \tag{3.4}$$

where ε_0 is the intrinsic film strain and ε_m is the mechanically applied strain that the micro-extensometer is trying to measure.

The thermal strain, ε_{th}, induced by a difference in coefficient of thermal expansion of a poly-SiC tuning fork on SCS is estimated as:

$$\varepsilon_{th}(\theta) = \int_0^\theta (\alpha_{SCS}(\theta) - \alpha_{SiC}(\theta))d\theta \tag{3.5}$$

where $\theta = T - T_0$ and T_0 is some reference temperature, taken as room temperature in this work, and α is the CTE. This equation builds on the aforementioned concept that the substrate has a much larger cross-sectional area than the tuning fork. As such, it is assumed that the substrate thermal expansion is not constrained by the mechanical stiffness of the gauge. Therefore, the thermal strain is the difference between how much the substrate and gauge expand with temperature, independent of each other. This assumption would not be appropriate when the device layer and substrate are of similar stiffness.

The reference temperature choice can greatly effect the expected response of the tuning fork. Specifically, the reference temperature is the temperature in which "zero" thermal strain is expected. Alternately, the calculation could be performed which assumes that the "zero" thermal strain occurs at the deposition temperature. The difference between these two approaches is simply a constant value of strain which is induced from the cooling of the wafer from the deposition temperature to room temperature. When the zero point is set at a high temperature, the constant value of strain is added to the thermal strains. When the zero point is set at room temperature, this constant value is added into the intrinsic strain. Currently reported intrinsic strain numbers are at room temperature, and already include the thermal effects of cooling from the deposition temperature. Using the "zero" thermal strain at room temperature simplifies comparison of intrinsic strains with current literature.

The temperature dependence of the coefficients of thermal expansion were estimated from various literature sources. Some authors have provided their own unique fitting functions

to tabulated data, such as Reeber [68]. For other authors who provided tabulated data, polynomial fits were sufficient. It should be noted that even small differences in the value of the measurement of the coefficient of thermal expansion can have a significant effect on the predicted frequency response of this model. To try to minimize differences in measurements between authors, data from an author who published values for both silicon and silicon carbide was preferentially viewed.

3.2.4 Physical Insight

Given all these insights, one area which is not clear is the amount and nature of the thermal strain which needs to be applied to counteract changes in the resonant frequency due to modulus of elasticity softening. To gain some physical intuition one can combine equations 3.2, and 3.3 to solve for the strain as a function of modulus, as shown in equation 3.6.

$$\begin{aligned}\varepsilon(\theta) &= \frac{C_1}{C_3}\left(\frac{1}{E(\theta)} - \frac{C_2}{C_1}\right),\\ C_1 &= (2\pi f)^2 L^3 (0.397\rho AL + m_c),\\ C_2 &= 198.6 I_{xz},\\ C_3 &= 4.85AL^2,\end{aligned} \tag{3.6}$$

Plotting this equation with numbers used from this experiment reveals that a very small increase is needed to deal with the decreasing modulus of elasticity. However, to determine the applied strain, one will most likely be examining coefficient of thermal expansion data, and not the applied thermal strain directly. As such, this means that a very small constant difference in CTE will lead to perfect temperature compensation. In practice, it is difficult to find materials with perfectly matched, very small differences in CTE.

Instead, another way to achieve this very small difference is to find where the CTE data for different materials will exactly match and cross-over one another (as is the case for SiC on Si). At this cross-over point, the CTE of SiC is perfectly matched to Si. While the CTE data does not exactly follow a constant small difference, the area close to the cross-over point may be approximated as such, and does provide temperature compensation. As the temperature increases further, the CTE numbers become quite different. Thus, for large temperature excursions, this phenomenon also increases the temperature sensitivity of the device away from the optimal operating temperature. As such, it may also be used to increase the temperature sensitivity of a device.

It is also important to keep in mind the magnitude and direction of both the change in the modulus of elasticity and the applied thermal strain. For the case of SiC on Si, with increasing temperature, the modulus of elasticity decreases. As such, tensile strain is needed to compensate, and the CTE of Si needs to be greater than SiC. Most materials follow this trend, however, there area few materials in which the modulus of elasticity increases with

temperature, such as silicon dioxide. If a device needing temperature compensation were fabricated from such a material, compressive strains would need to be introduced.

Finally, it should be noted that changing the geometrical properties of the tuning fork will also change the extent and nature of temperature compensation. In examining equation 3.6, it is noted that the coefficients of thermal expansion and modulus of elasticity will be constant for a given material set. However, changing the other tuning fork parameters will change the constants in equation 3.6. This can also be used to change the temperature at which the exact temperature compensation occurs.

3.2.5 Turn-over Temperature

While the method mentioned above is highly dependent on the exact location of the cross-over point in CTE data between SiC and Si, there is some flexibility in where the temperature compensation will occur. This was determined by taking the derivative of equation 3.2, as shown in equation 3.7. Setting the derivative to zero and solving for θ gives the temperature where the frequency is a maximum or minimum. At and around this point, called the turn-over temperature, the passive temperature compensation has it's maximum effect. Alternatively, one could also use a maximizing routine in conjunction with equation 3.7. In all cases, changing the geometrical properties of the tuning fork will also change the turn-over temperature. However, this will also change the resonant frequency, so care must be used if designing for specific frequency and turn-over temperature goals.

$$\begin{gathered}\frac{\partial f}{\partial \theta} = \sqrt{\frac{198.6E'I_{xz} + 4.85E'AL^2\varepsilon + 4.85EAL^2\varepsilon'}{L^3(0.397\rho AL + m_c)}} \\ E' = E_0(\eta_1 + \eta_2\theta) \\ \varepsilon' = \alpha_{SCS}(\theta) - \alpha_{SiC}(\theta)\end{gathered} \tag{3.7}$$

3.3 Measurement Setup

To validate the analytical model presented, two different double ended tuning forks of similar frequency but different geometrical parameters were used, as shown in Figure 3.2. The two designs have been described and tested previously, and will be referred to as either the balanced-mass double-ended tuning fork (BDETF) [3] or the comb-drive double-ended tuning fork (CDDETF) [5]. The tuning forks were fabricated in a four-mask process on single crystalline silicon substrates, described previously [3]. Both forks utilize the same anchor (five of diamonds) and the same bond pad to ensure that the differences in frequencies are not due to a secondary effect. The tuning forks were resonated in air using a previously described square wave oscillator (SWO) [5]. As such, they also had a similar, low quality factor near 500.

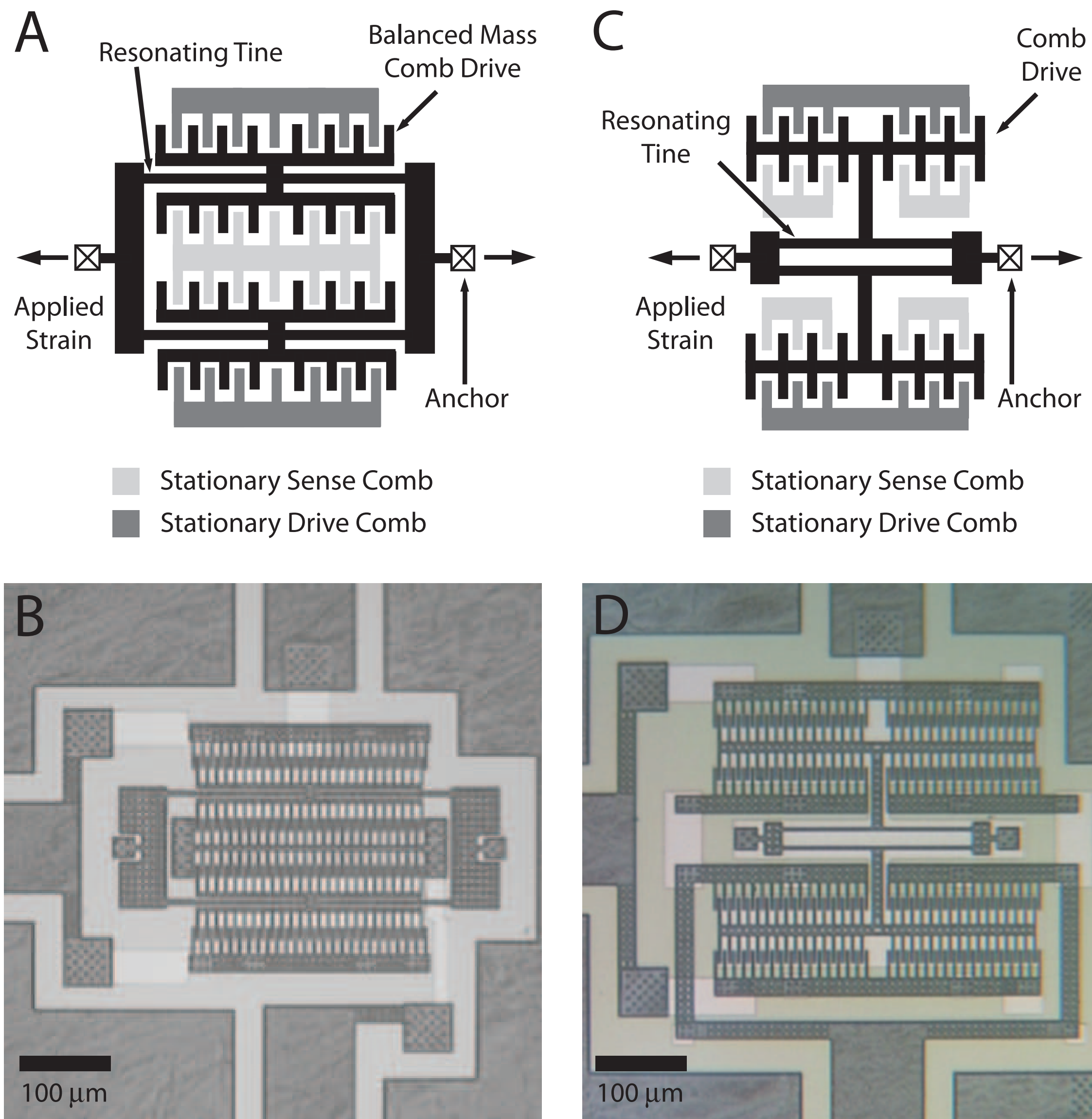

Figure 3.2. Two different tuning fork topologies with identical anchors were used in this study. A) Principle location of the tines, drive combs and sense combs of the balanced-mass double-ended tuning fork (BDETF) B) Micrograph of the actual BDETF C) Standard comb-drive double-ended tuning fork (CDDETF) topology and the location of important components D) Micrograph of the CDDETF

Table 3.1. Geometrical & Material Properties of Tested SiC on Si tuning forks [5, 3]

Property	CDDETF	BDETF	units
Room Temperature Frequency (f)	213.92	207.88	kHz
Beam length (L)	200	306	μm
Top beam width (w_a)	3.34	3.8	μm
Bottom beam width (w_b)	4.7	6.7	μm
Film thickness (t)	7.0	7.0	μm
Comb-drive mass (m_c)	$1.997 \cdot 10^{-10}$	$1.4061 \cdot 10^{-10}$	kg
Initial film strain	419		$\mu\varepsilon$
Density	3150		kg/m^3
Modulus of Elasticity at RT (E_0)	298		GPa

In order to characterize the temperature response of the tuning forks at high temperature, a localized heating setup is used, as shown in Figure 3.3. The IR lamp (SpotIR Model 4085, Research, Inc.) is aligned to an aluminum plate aperture and focused onto the backside of the MEMS die. Foam is used to isolate the PCB electronics from the aperture and scattered infrared radiation. The setup is calibrated for different power and time settings using a K-type thermocouple. This setup enables heating the die to 320°C while keeping all of the PCB-mounted electronics at or below 125°C. Temperature accuracy is expected to be no greater than ± 5°C for this setup.

To verify that the flatting of the frequency response near room temperature was not an artifact of the high temperature testing apparatus, additional measurements between 5°C to 80°C were made using a Tenney Jr. environmental chamber (Figure 3.3). The chamber has a temperature resolution of 0.1°C and a maximum control tolerance of ±0.3°C. The SWO electronics with the DETF dice attached were placed inside the environmental chamber. Desiccant was placed inside the chamber and the chamber was purged with nitrogen prior to starting the temperature tests in order to minimize the risk of condensation onto the electronics during the low temperature setpoints. Tests were conducted from 5 to 80°C in 5°C intervals. During all tests, temperature setpoints were run in non-sequential order to ensure the results were not influenced by possible drift in the resonant frequency with time or with the direction of temperature ramping.

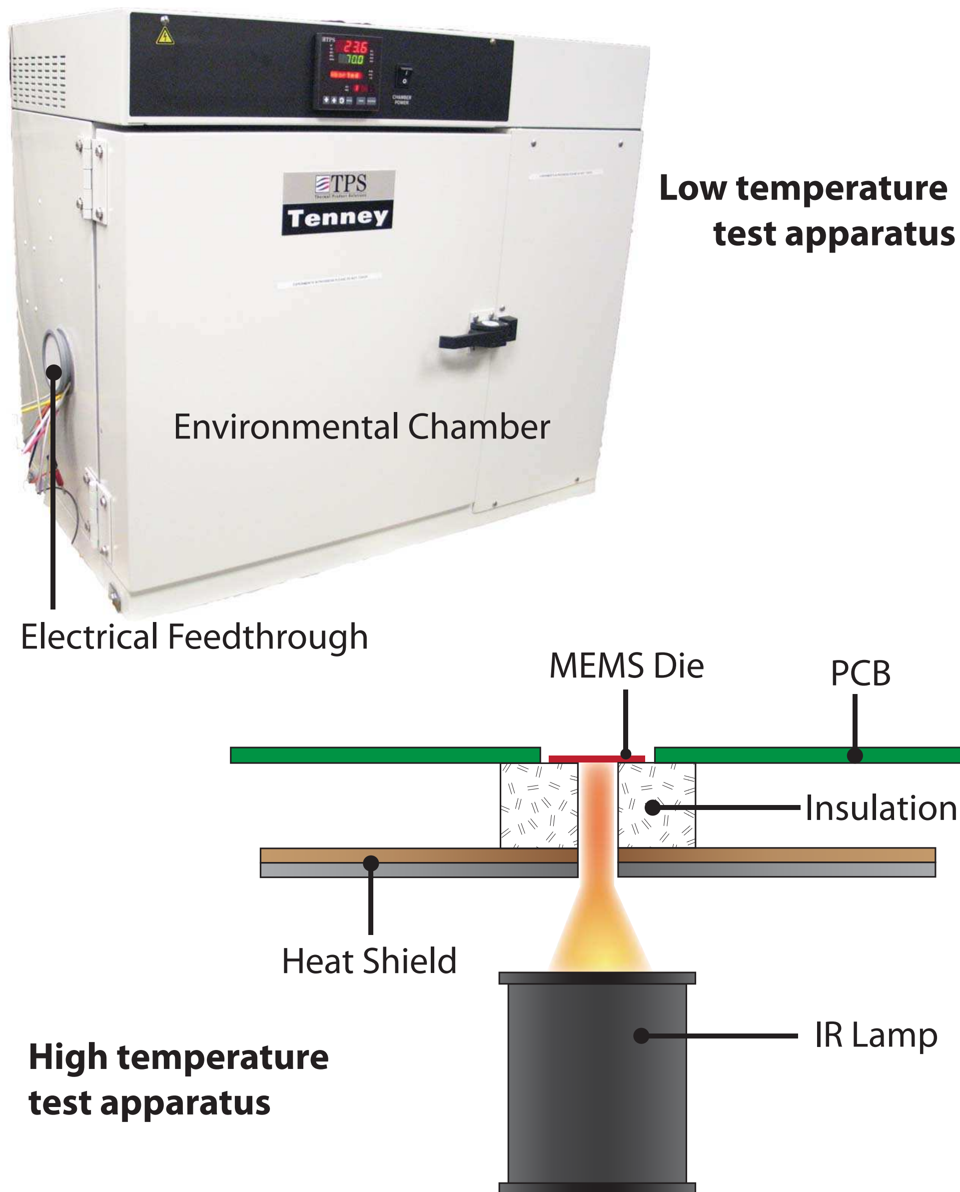

Figure 3.3. For high temperature characterization a localized heating setup is used to characterize the frequency versus temperature response of the resonant micro-extensometer. This setup does not provide sufficient temperature sensitivity near the turnover temperature, instead an environmental chamber is used in that regime.

3.4 Results

3.4.1 Coefficients of Thermal Expansion

It is helpful to begin by examining some of the published values of the coefficients of thermal expansion of silicon and silicon carbide, as shown in Figure 3.4. CTE data for SCS and poly-SiC is available from a variety of literature sources [69, 70, 71]. The model presented previously is highly dependent on the values and difference between the different CTEs. For this particular analytical model, only CTE data from literature sources in which the same author characterized both SCS and poly-SiC was used. It is presumed that these authors would have less deviation between data compared to different authors.

It is interesting to note that the standard values of α found in the literature for SCS and poly-SiC are 2.6 ppm/°C and 4.2 ppm/°C, respectively [72]. Furthermore, the temperature range for which these values are appropriate is often not listed. Indeed, it is clear from Figure 3.4 that these tabular values are not for the same temperature range. As such, a turn-over temperature would not be expected based on the constant-value tabular data usually presented for these materials. The temperature compensation only appears because α_{SCS} and α_{SiC} are functions of temperature and α_{SiC} decreases more rapidly near and below room temperature than α_{SCS}. The values are different by less than 0.5 - 1 ppm, but this small difference is still the primary cause of temperature compensation.

For the case of a silicon substrate with a silicon carbide device layer, the exact location of the cross-over point greatly effects the temperature compensation. As mentioned previously, the cross-over point is where small thermal strains are produced which can counteract the change in the modulus of elasticity. In examining Figure 3.5, it is seen that the location of the cross-over point with respect to temperature also co-insides with the peak in the thermal strain curve. Unfortunately, the data presented in the literature has cross-over points at vastly different temperatures. Slack's data has a cross-over temperature around 250 K, where as Reeber's data has a cross-over temperature around 425 K. Also, the authors collecting CTE data warn that the errors in this data can be high, with Slack estimating a maximum error of 15%.

Neither of these CTE data sets exactly matched the experimental data when used with equation 3.2. However, the experimental data showed a turn-over temperature of approximately 325 K, which was in between the data presented by Reeber and Slack. To see if the experimental data could reasonably be explained by slight changes in the CTE data, an experimental fit to the frequency data was created and used to back calculate a CTE difference. Beginning with the frequency data, a thermal strain for each set of experimental data was calculated. Using this thermal strain, and a reference CTE line (in this case, Slack Si data), an estimated SiC CTE was calculated, shown as the solid line Figure 3.4. The reference CTE was needed since the thermal strain information does not contain information on the absolute value of the CTE, only a difference. Either author's silicon CTE could have been used for this plot, and similar results are expected. Since CTE data should be the same

for each device, an average was also calculated. The slight changes in CTE data could be attributed to a measurement errors, or through slight changes in the material properties of the films. In all cases, the CTE data was well bounded by the authors, with a similar curve shape and form, as seen in Figure 3.4.

3.4.2 Thermal Strain & Frequency Response

The thermal strains predicted by different authors and from an experimental fit are shown in Figure 3.5. As mentioned previously, the location of the thermal strain peak is set by the cross-over point. However, the actual magnitude of this peak is dependent on the reference temperature chosen in equation 3.5. The thermal strains predicted from experimental data have the lowest absolute value since they are the closest to the chosen reference temperature.

From Figure 3.6, it is seen that the experimental data temperature turnover point is bounded by both Reeber and Slack. Furthermore, the shapes of the curves, especially near the turnover temperature are similar. One of the key questions about the two different experimental data sets was whether a single set of thermal strain data could be applied for both tuning forks. To determine this, polynomial fits to the experimental data were created and using equation 4.3, thermal strains were determined. These thermal strains were the exact strains needed to fit the analytical model to the experimental data. Ideally, the thermal strains should be matched since the same material was used for both resonating devices. These differing thermal strains were averaged and the frequency vs. temperature response for both tuning forks was plotted. This response is shown in Figure 3.6 as "CD. Average" for the CDDETF and "B. Average" for the BDETF. Both of these plots are using the same value for thermal strain, and only the geometric properties of the tuning forks are different. Since both curves fit the experimental data well, this indicates that the temperature phenomenon observed is not due to some unique property of a particular tuning fork. Rather, this is a physical phenomenon which arises from a modulus of elasticity change compensated by thermal strains.

Considering all of these results, the proposed model appears to have captured the physics occurring to thermally compensate these tuning forks. First of all, the calculated frequencies using an averaged thermal strain match well with the experimental data, shown in Figure 3.6. The thermal strains needed to fit this data are similar to those calculated from other authors as seen in Figure 3.5. Finally, the estimated coefficients of thermal expansion are within the numbers proposed by Reeber and Slack, both in value and crossover point. Considered together, this data does support the idea that modulus of elasticity softening is compensated with induced thermal strains created by a CTE mismatch between the device and substrate layers.

However, it is clear that there are some errors present in this model. For example, there should really be a single value of the thermal strain and CTE. However, experimental errors are the most likely explanation for this discrepancy. Collecting high temperature data, using traditional silicon electronics is challenging and requires local heating of the

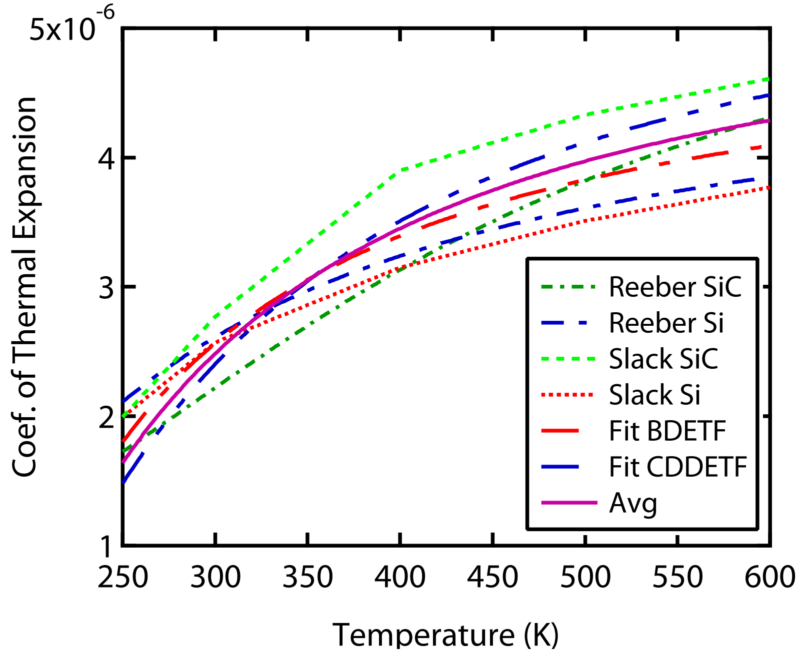

Figure 3.4. CTE (α) of SCS and poly-SiC from the literature [70, 71, 69]. It is noted that the silicon carbide and silicon data is matched (crossover) for Slack around 250K whereas Reeber's data is matched around 425K. Neither data set accurately predicted the response of the two DETFs. Instead, the predicted CTE function of the poly-SiC used in the fabricated structures is calculated from the experimental frequency response of the micro-extensometer. This predicted CTE value is in between the values specified by Reeber and Slack.

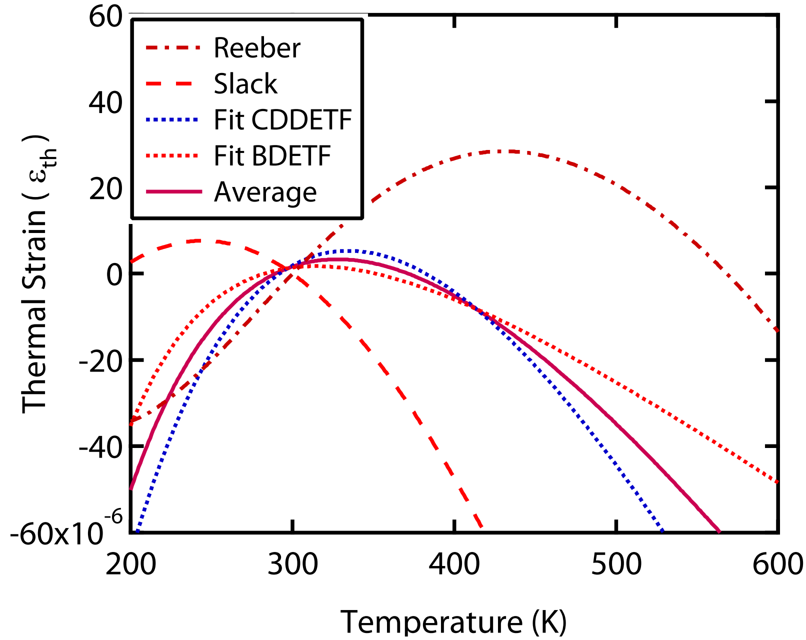

Figure 3.5. The thermal strain (ε_{th}) applied to the resonant micro-extensometer anchors versus temperature is calculated from the CTE mismatch based on the literature as well as from the measured frequency response.

MEMS die. In examining the data, the largest error occurs at the higher temperatures. Furthermore, it should be noted that these devices were not encapsulated and are subject to slight environmental variations. However, the environmental variations typically appear over longer time scales than those used in these experiments.

3.4.3 Turnover Temperature Estimates

By examining the resulting equation, it is seen that the width-to-length ratio can be used to tune the turn-over temperature. Therefore, the resonator designer has some control of the turn-over temperature by geometric means. Figure 3.7 plots $\hat{\theta}$ as a function of the tine width to length ratio, w/l. This figure demonstrates one of the design trade-offs necessary to tune $\hat{\theta}$ closer to room-temperature. Namely, decreasing $\hat{\theta}$ also decreases the normalized strain sensitivity of the resonator. Likewise, the unstrained natural frequency, f_0, increases with w/l, which introduces additional challenges in designing ultra-low noise oscillator electronics. So, although the designer is allowed a geometric method in which to tune $\hat{\theta}$, this modification is constrained by other aspects of the resonator design.

3.5 Discussion

The analytical model described in this chapter can be adapted for any two material sets to predict the frequency response of a DETF for a given temperature. The key to using this model lies in finding coefficient of thermal expansion (CTE) data as a function of temperature. This particular model predicts that a temperature insensitive region occurs for the case of a silicon carbide DETF on a silicon substrate. Experimental evidence taken from two DETFs with different geometries supports this model. However, the exact location of the temperature insensitive region is highly dependent on the actual value of the CTE for a given temperature. Also, it is possible to slightly move the location of the temperature insensitive region by changing the geometrical parameters of the tuning fork.

To determine the effectiveness of the temperature compensation, the data from the analytical fits of the experimental data presented in Figure 3.6 is used. Each tuning fork will have a peak temperature compensation at different temperatures due to the different geometries. Considering a 50°C range (±25°C), the BDETF temperature sensitivity is a minimum around 38°C at 0.2 Hz/°C (0.9 ppm/°C). Similarly, the CDETF had a temperature sensitivity of 0.1 Hz/°C (0.46 ppm/°C) at 35°C. This is a 10-fold improvement over an equivalent epitaxial silicon resonant miro-extensometer (-30 ppm/°C) at those temperatures [5]. However, the comparison to a silicon resonator is useful, but it does not compare two silicon carbide devices. Unfortunately, experimental data has not yet been taken for an all SiC tuning fork, but the predicted value based on modulus of elasticity softening is 22ppm/°C. As such, similar performance improvements are expected.

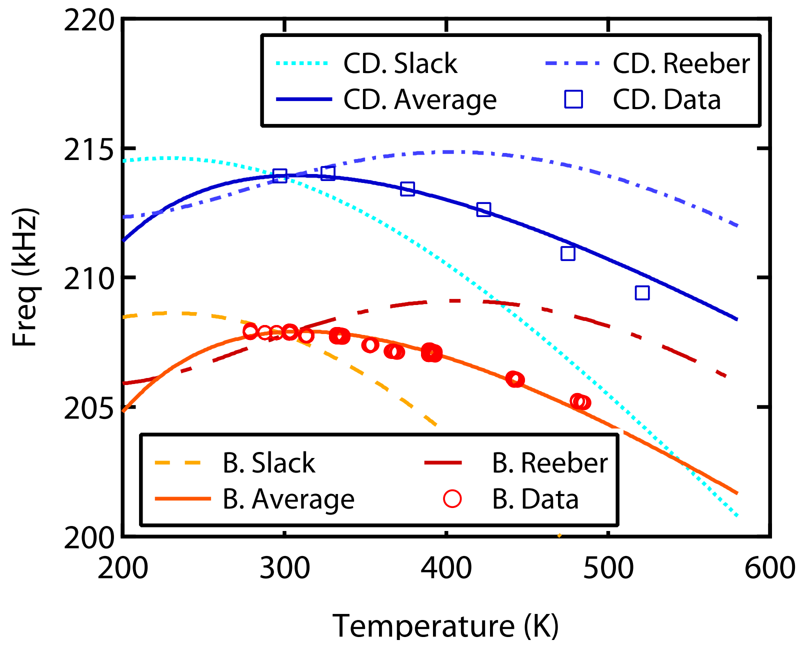

Figure 3.6. Predicted frequency response of the BDETF (B.) and CDDETF (CD.) versus temperature. Each line is based on different values of CTE from the literature. The data points are the experimentally measured frequency response.

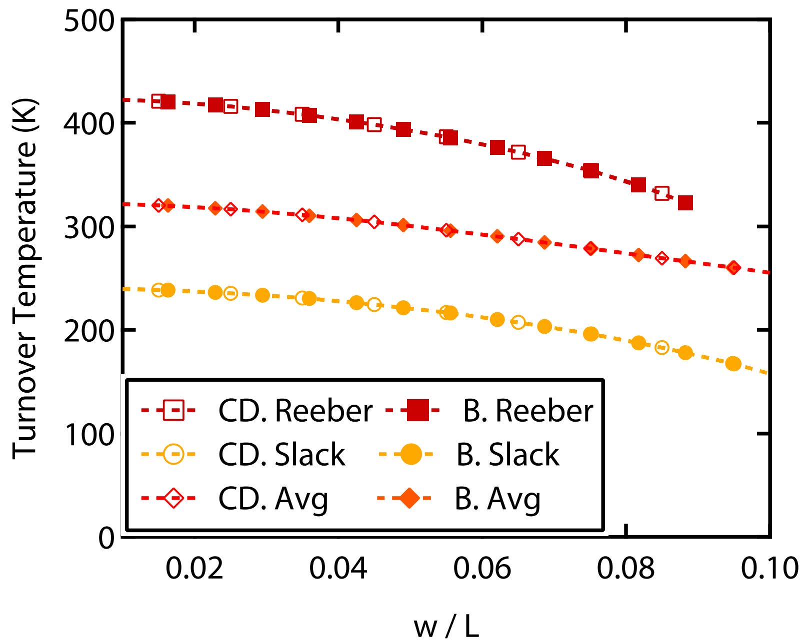

Figure 3.7. Equation 3.2 predicts that the tuning fork tine width-to-length ratio can be used to significantly adjust the turnover temperature. Each point is the numerically calculated turnover temperature for the different resonator designs and CTE data. "B." is for the BDETF and "CD." is for the CDDETF.

Chapter 4

Strain & Torque Testing

4.1 Torque Sensor Uses and MEMS Potential

This chapter specifically examines how to use a MEMS double-ended tuning fork (DETF) as a torque sensor on a circular shaft. It begins with an examination of how to join circular objects to MEMS dies. To predict the strain transfer to the MEMS gauge, a combination of analytical and numerical models were needed and are described here. Experimentally, the gauge is bonded to a custom built test apparatus using both epoxy and metal induction bonds. With the metal bonds, the chapter reports on the first high strain ($1000\mu\varepsilon$) testing of a MEMS strain sensor.

One of the key reasons for using MEMS DETF strain sensors is the extreme sensitivity. Previous work has shown that MEMS double ended tuning fork (DETF) resonant strain sensors are inherently sensitive and capable resolving nanostrain in high bandwidth applications [5]. These properties combined with a small form factor make the MEMS resonant gauges well suited to measuring strains on a variety different components. The extreme sensitivity is especially useful on monitoring very stiff components, such as an automotive halfshaft, which experience very small strains under normal use.

The halfshaft is a solid metal rod used to connect a wheel to the differential. It is typically induction hardened and is approximately one inch in diameter. This extremely rigid component is designed to accommodate high torques which occur during emergency maneuvers. As such, strains which occur in the halfshaft from normal driving conditions tend to be small and difficult to measure. Here, by taking advantage of both the high sensitivity and resolution in high bandwidths, real time wheel conditions can be determined as shown in Figure 4.1. Accurately knowing the torque conditions at the wheel of an automobile could improve stability and traction control.

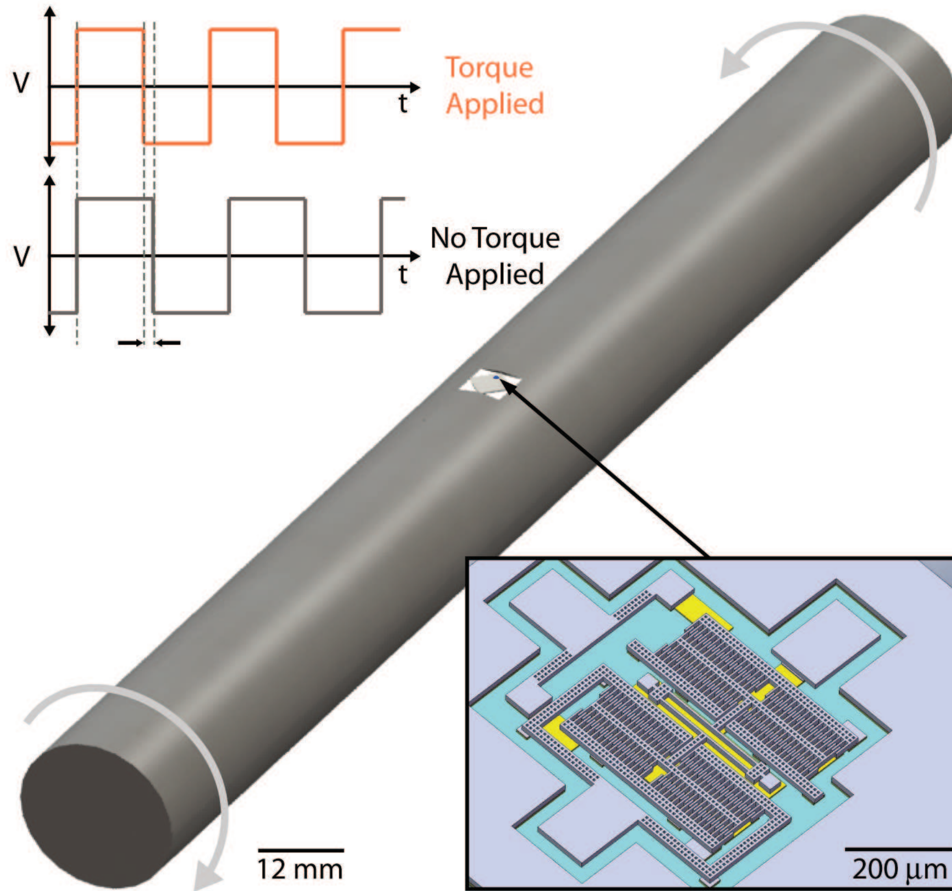

Figure 4.1. Conceptual image of MEMS resonant strain sensor measuring torque on a 2.55 cm diameter pipe. Both the main graphic and inset are to scale. The MEMS DETF strain gauge is on a 5 mm x 5 mm die.

Aside from being useful for automotive technology, torque sensors are useful where knowledge of the forces on mechanical components could significantly improve system life, function, and efficiency. Other applications include monitoring machining operation cutting forces [73], stability control, robotics, oil drilling, and damage monitoring in aviation components [31].

The MEMS resonant strain sensor performance compares favorably with other existing torque sensors. Fundamentally, torque may be monitored by measuring strain, angle of twist, or stress (magneto-elastic methods) [6]. When combined with an application specific circuit (ASIC), the strain sensor in this work will have an extremely small form factor, which is advantageous when compared to optical based sensors. Furthermore, the sensors are insensitive to magnetic fields, unlike the magnetoelastic based torque sensors. Finally, these sensors are more sensitive than surface acoustic wave (SAW) based sensors [74], the ppm change in this work is approximately 96 ppm vs 46 ppm for the SAW sensor.

4.2 Torque Measurements & Strain Transfer

4.2.1 Strain Based Torque Measurement

Torque measurements may be taken by measuring strain, angle of twist, or stress (magneto-elastic methods) [6]. The sensor presented in this work operates by measuring surface strains induced when torque is applied to the halfshaft. Typical shafts experience a variety of principle (ε_x, ε_y) and shear strains (γ_{xy}). Each applied strain will affect the strain (ε) measured for a given direction (θ), as shown by the normal strain transformation given in Eq 4.1. In Eq 4.1, $\theta = 0$ is in line with the principle longitudinal axis of the halfshaft.

$$\varepsilon(\theta) = \varepsilon_x \cos^2\theta + \varepsilon_y \sin^2\theta + \gamma_{xy}\sin\theta\cos\theta \tag{4.1}$$

By setting the measurement angle to 45°, and assuming negligible applied principle strains, the torque as a function of measured strain may be written as shown in Eq 4.2, where G is the modulus of rigidity and r is the outer radius of a solid tube. The assumption of negligible principle strains is valid in this system since the testing apparatus was specifically designed to give this condition. In actual practice, multiple gauges would be necessary in a strain rosette formation to determine the complete state of strain.

$$T = \frac{\gamma_{xy}\pi G r^3}{4} = \frac{\epsilon(45°)\pi G r^3}{8} \tag{4.2}$$

From Eq 4.2, it is observed that for a given torque value, T, increasing the radius slightly will greatly decrease the measurable strain. Thus, for a constant strain sensitivity, the torque sensitivity will decrease with increasing radius and increasing component Modulus of Elasticity (E). For systems experiencing non-negligible principle strains, three gauges mounted at differing angles can be used to extract the complete state of stress.

4.2.2 MEMS Double Ended Tuning Fork Strain Equation

For the case of a double ended tuning fork, the frequency change of the device as a function of strain (ε), material properties, and device dimensions is given by equation 4.3 as derived in [28]. Briefly, the differential equation for a vibrating beam with tension and point masses is solved using a Rayleigh-Ritz approach, which is detailed in [25, 24]. An analytical version of the solution is found by assuming a trial function for the first mode shape, as found in [75, 28].

$$f[\epsilon] = \frac{1}{2\pi}\sqrt{\frac{256 E w^3 t}{15 L^3 \left(\frac{128}{315}\rho t w L + M_{\mathrm{act}}\right)}\left(1 + \frac{1}{7}\frac{L^2}{E w^3 t}(2wtE\varepsilon) + \frac{2}{7}\frac{L^2}{w^2}\varepsilon_{\mathrm{bi}}\right)} \tag{4.3}$$

Here, the length (L) is 200 μm; width(w) is 7 μm; and height (h) is 10 μm; the density(ρ) is 2220 kg/m^3; and Modulus of Elasticity (E) is 146 GPa. It should be noted that the coefficient for the applied strain (ε) and the built in strain ($\varepsilon_{\mathrm{bi}}$) is exactly the same, but written differently. In this format, $2wtE\varepsilon$ can be easily replaced with the force, F, if needed. If the built in strain is within the same order of magnitude as the applied strain, there will not be a significant change in the sensitivity of the gauge, but there will be a shift in the frequency with zero applied strain. The key to accurately determining the expected frequency response lies in determining the actual strain transfer to the gauge, from the measurement surface, through the substrate, and coupled into the resonating beams.

4.2.3 Strain Transfer for Torque

Previous authors [35, 33] have found that the strain transfer through a silicon die may have a significant effect on the strain measured by the strain gauge. The presence of the silicon die tends to locally stiffen the area of measurement. However, in the case of bending, the additional distance from the neutral axis can actually amplify the measured strain. To understand the strain transfer for a round object in torsion with an applied die, it was necessary to construct a finite element model.

In this case, a 3D half scale model of the experimental setup was constructed using COMSOL 3.5a. The shaft was 25.5 mm in diameter with a 3.5 mm flat, and assumed to be isotropic, 4340 AISI Steel. Other methods may be used to attach the die to the halfshaft, but in this case creating a flat had a minimal effect on the structure. Only 0.5 mm of shaft material was removed, exposing a 7 mm flat for bonding (which is a 3.5 mm flat when modeling half of the structure). Using a modified moment of inertia and stiffness to account for the flat[76], it was found that the shaft stress increases 9% and the stiffness reduces by 0.7% [77]. Also, the full length of the bar was not modeled, instead a length was chosen in which the end loading conditions did not effect the middle die area.

A 30 $\mu\varepsilon$ isotropic solder layer of 60Sn-40Pb was used to join the steel to silicon die. The silicon die was 5mm on a side, 200 $\mu\varepsilon$ thick, and modeled as anisotropic material, with the 100 direction normal to the surface, and the 110 direction parallel to the die edge. The die was orientation mimicked what would be needed for the actual sensors used in this case, since the tuning fork sense direction is parallel to the edges of the die. Since the tuning forks are lithographically defined, their on-chip direction may be easily changed, and virtually any die orientation could be chosen.

Each material was meshed with tetrahedral elements, and torque was applied to the boundaries. In this case, a torque was applied to create 1000 $\mu\varepsilon$ of engineering shear strain in the top surface of the halfshaft, as shown in Figure 4.2. Here it is noted that the maximum strain transmitted to the center of the die is approximately 84%. The strain transfer rapidly decreases near the edges of the die, and there is also a corner effect. In this particular case, the gauge is mounted approximately 2 mm from the top edge and 1 mm from the left edge of the die. At this location, the expected strain transfer is 75%. In Figure 4.2, it is seen that

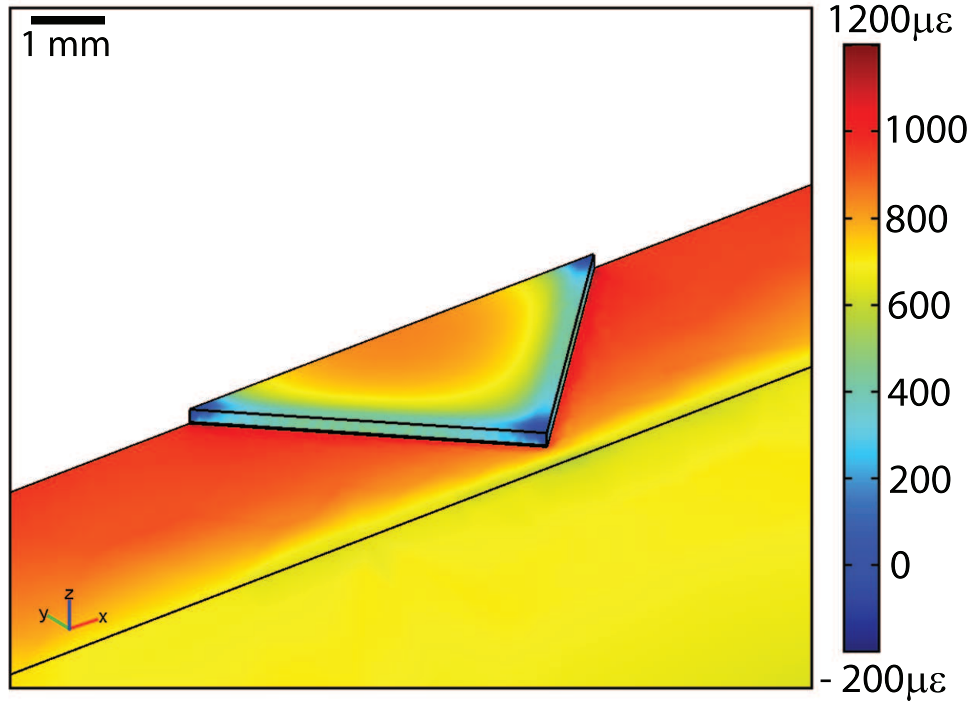

Figure 4.2. Plot of engineering shear strain (ε_{xy}) through a silicon die solder bonded to a steel halfshaft. When compared to the top steel surface, the strain at the center of the die is significantly lower and the shear strain rapidly decreases near the edges of the die. In order to achieve good strain sensitivity, careful placement of the strain gauge is needed.

there is a slight strain enhancement near the edges of the die and some induced compressive strain at the corners of the die.

4.2.4 DETF High Strain Analysis

When performing initial experiments on this device, it was found that using the beam resonant theory given above in combination with substrate transfer estimates was not adequate in describing the data. A Finite Element Analysis of the device discovered that additional strain transfer losses occurred between the substrate and the resonating beams.

A device level simulation was implemented using ANSYS 12.1. The model geometry was created and saved as IGES file in SolidWorks. By importing the IGES geometry in ANSYS environment it was possible to mesh the top surface of the device with MESH200 elements and extrude the meshed surface through the volume of the device using the command VSWEEP (see Figure 1). The element type used in the 3D mesh was SOLID5; these elements are 8 nodes with up to 6 degrees of freedom at each node are suitable for 3D coupled field analysis. The element size used to mesh the top surface of the device was 3 μm while the

element size used to extrude the 2D mesh through the entire volume was 5 μm. This mesh resulted in a model of less than 14000 elements which guaranteed a short computational time and accurate solution.

The loads and the boundary conditions are applied to the bottom surfaces of both anchors. In order to simulate the behavior of the strain gauge, all the degrees of freedom of one anchor were removed. A fixed displacement was applied to the nodes of the second anchor. In order to obtain the frequency shift due to the base displacement, the ANSYS script first performs a static analysis to record the DETF stresses. The result of the static analysis is then used to perform the modal analysis. The displacement was applied in steps of 0.24 μm. The simulation shows that due to the effect/deformation of the anchors, the frequency shift is not linear. This simulation may partially explain and clarify the non-linearity's recorded in the experiments.

4.3 Experiment

4.3.1 Torque Testing Apparatus

The testing apparatus used to characterize the torque sensors is shown in Figure 4.3. The apparatus is based on a dual torsion member, closed-loop force design. This design applies a nearly pure torsional load to the halfshaft, ensuring that the device under test is only measuring applied torque. In this particular case, the apparatus is constructed around a modified 1987 BMW 325 halfshaft, but it may accept other halfshafts. Additional details on the design, construction, and validation of this testing apparatus, as well as a set of measured drawings are available in [77].

To operate the device, force is applied to the torque arm with the hydraulic jack. The torque arm is attached to the halfshaft via a spline, and applies a torsional load to the halfshaft. The Rzeppa (constant velocity) joint accommodates angular misalignment and holds the halfshaft rigidly in place during testing. The halfshaft may be completely removed from the testing apparatus to facilitate strain gauge bonding, wire-bonding, and temperature testing.

A flat was milled into the halfshaft to simplify the bonding process. For this particular case, to achieve a 7 mm wide flat for a 26 mm diameter shaft, 0.5 mm of shaft material was removed. It should be noted that the purpose of the flat is only to facilitate the connection between the die based sensor and halfshaft, and is not intended to weaken the shaft. Using a modified moment of inertia and stiffness to account for the flat[76], it was found that the shaft stress increases 9% and the stiffness reduces by 0.7% [77].

The MEMS DETF has a gauge length of 200 μm and is fabricated on silicon wafers which were diced into 5 mm squares. The DETF used for this experimentation is located approximately 1 mm from the top and 2 mm from the left side of the die. The final die

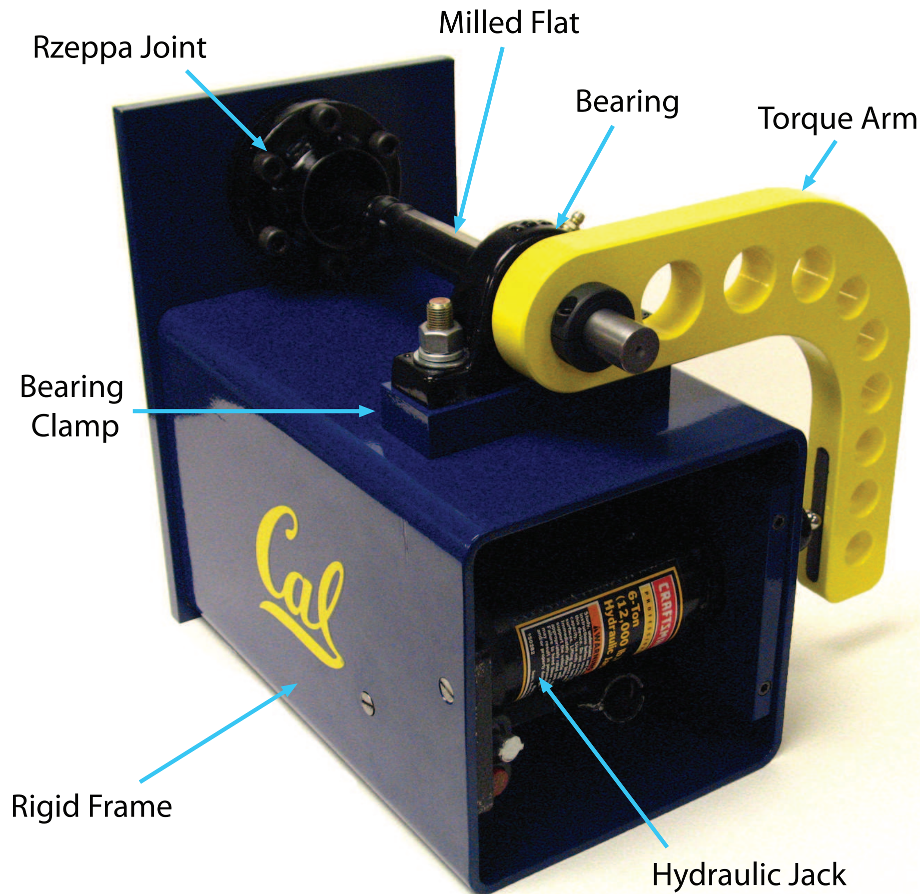

Figure 4.3. Torque testing apparatus. This apparatus has been specifically designed to apply pure torque to an automotive halfshaft.

thickness is 200 μm. Additional details on the DETF fabrication and device dimensions are given in [5].

Bonding has presented another key challenge which has prevented die based sensors from actually being attached to components. Several recent papers [33, 34, 78] have demonstrated the successful bonding of silicon based structures to metal substrates. In particular, the method described in [34] has the advantage of being implemented quickly and has been extensively tested. In this work, both a standard epoxy bond used previously [36] and the method described by Sosnowchik [34] were implemented.

4.3.2 Epoxy Bonding

The MEMS die was bonded to the halfshaft using MBond 610 epoxy, a two-component, epoxy-phenolic, solvent-thinned adhesive. It has a 30 minute work time and is suited to

operation at elevated temperatures. The sense beams were aligned 45 degrees to the central axis of the halfshaft. A well characterized Vishay CEA-13-187UV-350 metal foil strain gauge, designed for torque sensing, was also bonded with the same epoxy to measure the actual strain experienced on the halfshaft surface. It is noted that the metal foil gauge is expected to have perfect strain transfer since it is constructed of a pliable polyimide backing with thin metal traces. The metal foil gauge was applied to the halfshaft following Vishay's "Instruction Bulletin B-130".

The MEMS die was attached to the halfshaft using a modified version of the Instruction Bulletin. The area was degreased, dry abraded, conditioned and neutralized to clean and prepare the surface for bonding. M-bond 610 was applied to the target bonding area and to the back of the die. The die was placed on the shaft and a piece of teflon tape and a 1 mm thick silicone sheet with square holes were placed over the die. Then a 3 mm thick piece of aluminum was placed on the silicone, and pressure of approximately 200 Pa was applied using a v-block and v-block clamp. The holes were slightly smaller than the die area, such that pressure was transmitted to the edges of the die but did not touch the device area, as the sensor was not encapsulated.

The temperature curing process is based on the manufacturers recommendation, and is not optimized for joining two stiff objects together. The entire assembly was placed in a Tenny Jr. environmental temperature chamber, which is rated to hold a constant temperature within $\pm$ 0.3°C. The temperature was ramped to 165C over 1 hour, and held at temperature for 2 hours. The clamps were then removed, and a postcure at 200C for 2 hours was performed. The assembly was then allowed to cool overnight in the chamber.

4.3.3 Metallic Adhesive Induction Bonding

Bonding was performed using an Ameritherm Nova Star 1M induction heating module with a power output of 1350W at 11.7MHz. At this power and frequency, the bonding time required was 22 seconds. The copper induction coil used has an outer diameter of 16mm with eight turns and a pitch of 3.25 mm. The bonding location of the half-shaft was positioned 2.34 mm below the bottom of the induction coil.

A metallic adhesion layer consisting of 50 nm of Titanium, 500 nm of Nickel, and 20 nm of Gold was directionally evaporated onto the bonding surface of the MEMS device using an Edwards EB3 Electron Beam Evaporator in the UC Berkeley Marvell Nanofabrication Laboratory. Gold was evaporated last to reduce the formation of surface oxides during the bonding process.

The solder used for joining the MEMS die to the torque tube was 96.5Sn/3Ag/0.5Cu lead-free solder paste (Hi-Performance Lead-Free No-Clean Solder Paste, S3X58-M405, Koki Company Ltd.) Using a stenciled metal screen-printing shim, it was possible to obtain a layer of solder 50 μm thick, covering the 5 mm x 5 mm die area. The MEMS sensor was positioned off-axis from the half-shaft at a 45° angle.

The bonding process was observed using a FLIR A-320 infrared camera and using the manufacturer's suggested method, the emissivity of the steel on the milled flat surface was determined to be ϵ=0.122 and the emissivity of the half-shaft's paint-coating was determined to be ϵ=0.96. A peak temperature of 226.13°C was observed immediately beside the MEMS Device, as shown in Figure 4.4

4.3.4 Testing

Once bonding was completed, the square wave oscillator (SWO) board was attached to the halfshaft using two hole mount metal pipe clamps and screws. For the holes near signal traces, plastic screws were used to attach the pipe clamps to the board. The MEMS die was then wire-bonded to the SWO board. An additional wire-bond from the board ground to the halfshaft significantly reduced noise appearing in the square wave output signal. The frequency was measured using a frequency counter and the square wave was monitored utilizing an oscilloscope.

The halfshaft was then placed in the torque testing apparatus, as shown in Figure 4.5. Torque was applied to the halfshaft, and the frequency response of the MEMS strain gauge was compared to the response of the metal foil strain gauge. The metal foil strain gauge was used in a half-bridge wheatstone configuration, with an excitation voltage of 2V. For temperature testing, the halfshaft, SWO and gauge were placed in the Tenny Jr. environmental chamber. The temperature was changed in 5°C increments. At each testing temperature, the system was allowed to stabilize such that all components reached the same temperature, and measurements were taken every 10 minutes at the temperature of interest for one hour.

4.4 Results

4.4.1 Strain Sensitivity

Using an induction metal bond enabled repeatable strains up to 1000$\mu\varepsilon$ as shown in Figure 4.6. To understand how the strain is transferred to the MEMS device, it is helpful to consider two separate problems. The first involves determining how much strain is transferred from the steel shaft to the top of the silicon substrate. Using the previously mentioned COMSOL model of the silicon die mounted on the halfshaft, the strain transfer is approximately 75% near the MEMS device. In other words, if 1000 $\mu\varepsilon$ is measured on the steel, the strain near the MEMS device will be approximately 750 $\mu\varepsilon$. The second involves considering how strain is transferred from the top of the silicon substrate into the vibrating beams of the tuning fork.

Assuming perfect strain transfer from the top of the substrate to the vibrating beams of

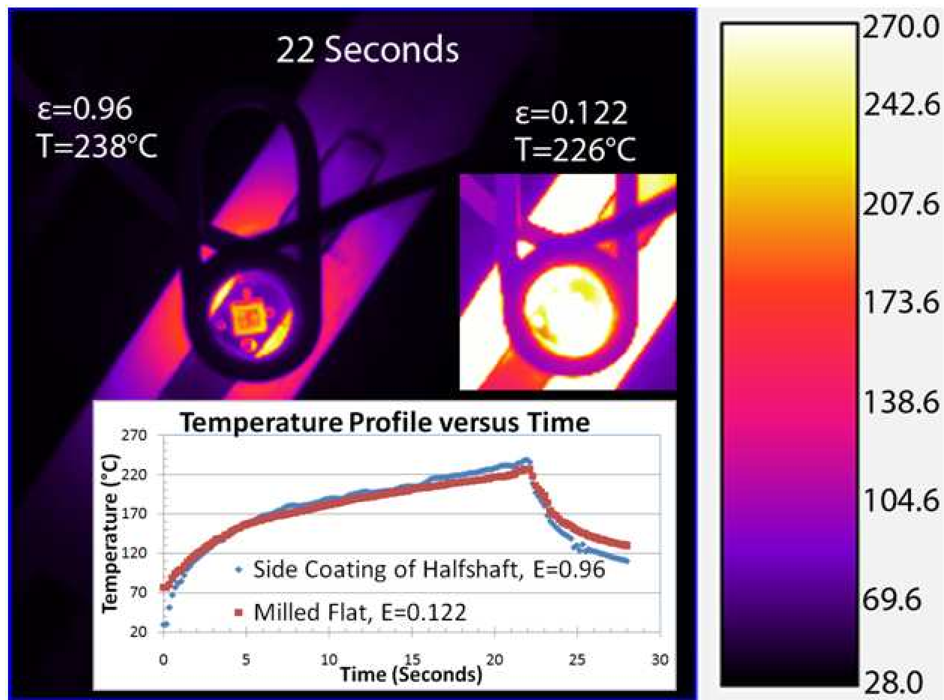

Figure 4.4. Temporal temperature data from induction bonding. Power was applied for 22 seconds at 1350W and 11.7MHz. The coating of the half-shaft has a spectral emissivity of 0.96 and the milled-flat bonding location has an emissivity of 0.122.

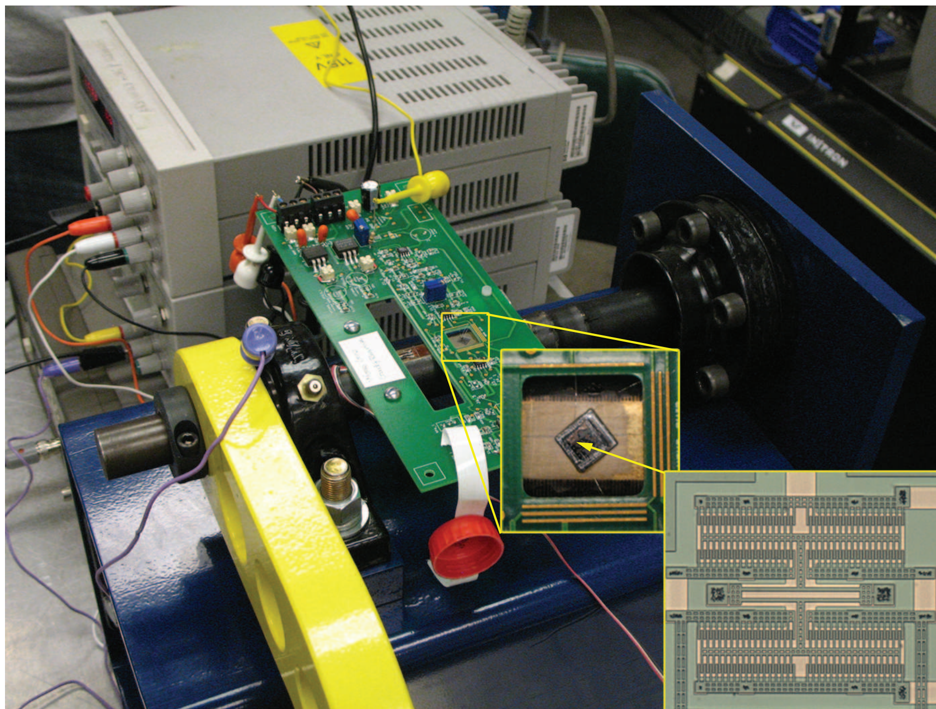

Figure 4.5. Experimental setup. The gauge is oriented to measure torques applied to the halfshaft and wire-bonded to the PCB. The inset shows the actual gauge used, the sense tines are approximately 200 microns long.

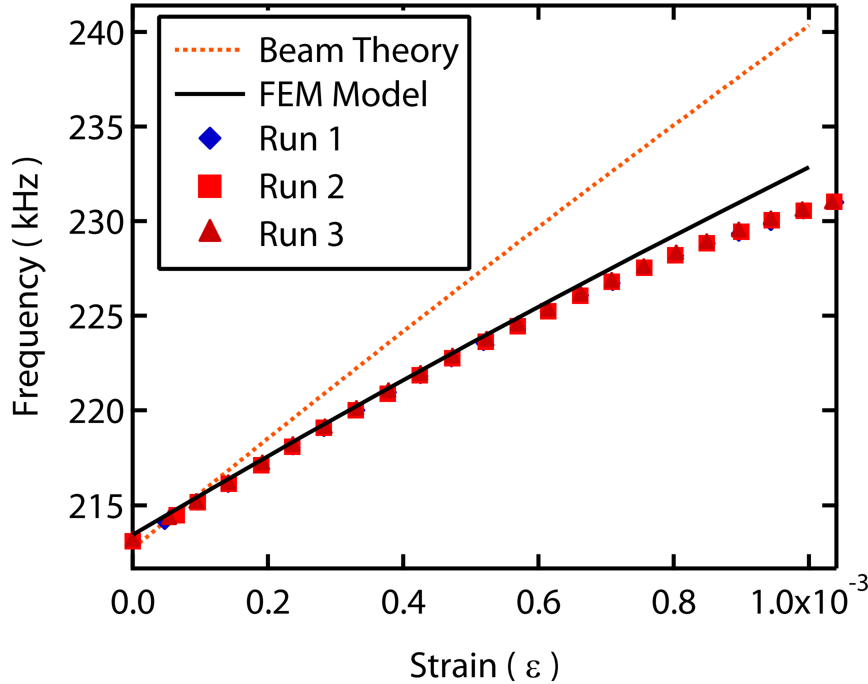

Figure 4.6. For the induction bonded die, the measured strain sensitivity of the tuning fork was lower than expected when combining equation 4.3 with estimates of the strain transfer through the MEMS die. Finite element models of the tuning fork under strain verified that some strain loss is occuring between the top of the MEMS die and the device itself.

the tuning fork, this strain transfer model may be combined with equation 4.3 to determine the maximum expected strain transfer. This is plotted in Figure 4.6, labeled "Beam Theory", and overestimates strain sensitivity of the device. This overestimation occurs because the model does not consider how strain is transferred from the top of the silicon die through the anchors and into the resonating beams.

FEM is used to understand how strain is transferred from the top of the substrate into the vibrating beams of the tuning fork. To be clear, this structure is called the anchor-block structure and includes the large square anchor tying the tuning fork to the substrate, the tether, and the block connecting the resonating beams. For reference, this structure is seen in Figure 1.1F. The strain transfers estimated by FEM are much more in line with the experimental data, as shown in Figure 4.6 labeled "FEM Model". In this particular case, the strain transfer over the 1000 $\mu\varepsilon$ range was approximately 26 Hz/$\mu\varepsilon$.

The strain sensitivity of this tuning fork was previously measured to be 39 Hz/$\mu\varepsilon$. However, this number was for very low strains (several microstrain), and was performed using on chip strain actuators. At such low strains, compliance and strain transfer in the anchor-block structure are not as large of a concern. One area for further study is the anchor-block structure, which couples the beams to each other and to the substrate. Most authors have examined this structure to maximize quality factor, and minimize energy loss, but little

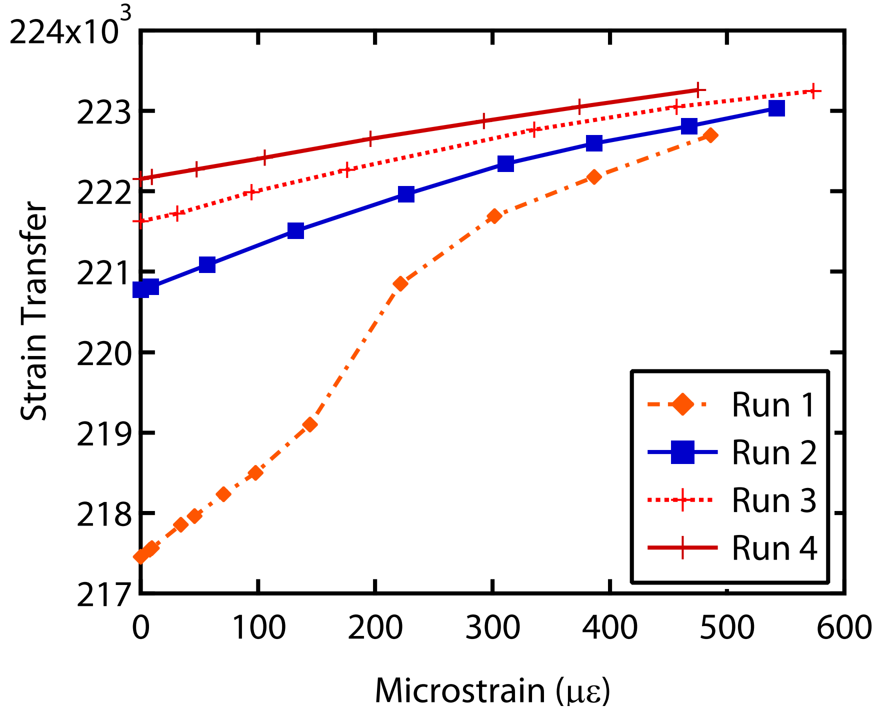

Figure 4.7. Measured frequency response to applied mechanical strain for an epoxy bonded gauge. The results show that the epoxy failed around 150 $\mu\varepsilon$. Bias voltage = 60V.

work to date focuses on this structure at high strains. Additional work in this area would be necessary to maximize the strain sensitivity of the tuning fork under high strains.

There is some curvature to the experimental data, especially at high strains, which is both repeatable, and not explained by the model. More analysis of the square wave oscillator circuit and the electrical properties of resonating structures under high strains would be useful in determining the exact nature of this non-linearity.

The induction bonding does appear to have caused some compressive strain in the gauge. As the underlying substrate cools from higher temperatures to room temperature, it compresses the strain gauge. In this case, the approximate unstrained frequency was 217 kHz, as measured in previous unbonded experiments with these strain gauges. The post induction bonded frequency was approximately 213 kHz. Using simple beam estimations, this equates to approximately 100 $\mu\varepsilon$. However, as mentioned above, a more complete analysis would be necessary to determine the exact number.

Epoxy bonding is an alternative for low strain applications, although the strain transfer is much lower than that of metal bonding. Initial experiments as shown in Figure 4.7 indicate that strains over 150 $\mu\varepsilon$ will cause delamination and failure of the bond. More conservative testing under 100 $\mu\varepsilon$ found repeatable results, although more testing would be necessary for long term tests. In Figure 4.8, it is seen that the strain sensitivity is low at 5 Hz/$\mu\varepsilon$ for epoxy bonding, compared to 26 Hz/$\mu\varepsilon$ for induction bonding.

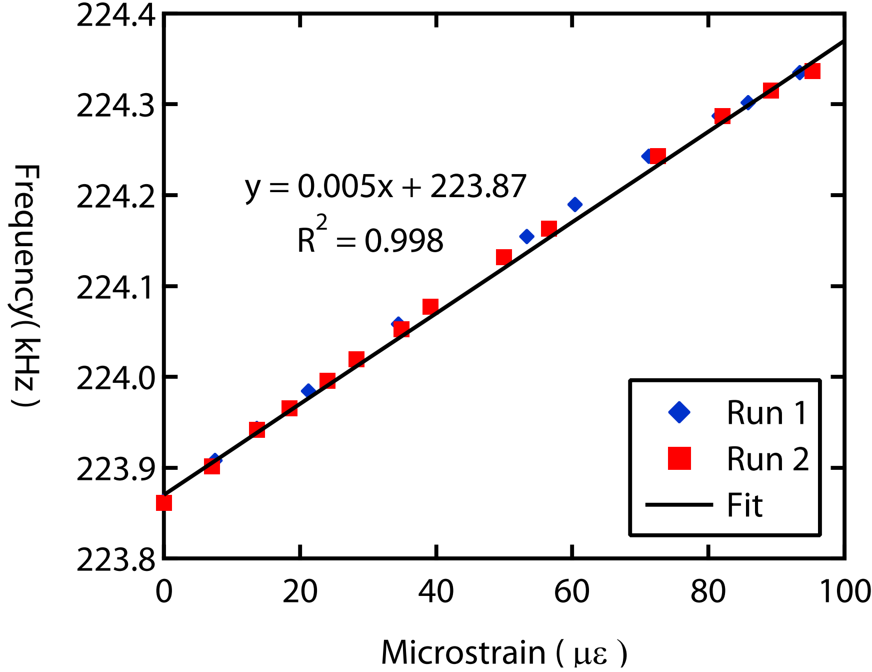

Figure 4.8. Measured frequency response to applied mechanical strain for an epoxy bonded gauge under 100 $\mu\varepsilon$. Bias voltage = 60V. The strain sensitivity of the system is extracted from this plot and used to determine torque sensitivities.

For epoxy bonding, it is also interesting to note that the natural frequency of the device after bonding shifted from 217.0 kHz to approximately 223.9 kHz, indicating that some tensile strain was induced. Unlike the induction bonding, pressure was applied during the epoxy bonding, and may play a role in the induced tensile strain. Also, a small local curvature in the halfshaft would have the effect of inducing tensile strain in the top of the die and could explain this phenomenon.

Using the measured strain sensitivity for both the induction bonded case and the epoxy bonded case, the torque sensitivity could be calculated by modifying Equation 4.2 and replacing strain (ε) with strain sensitivity ($\partial f/\partial\varepsilon$). The results for different shaft configurations and materials are presented in Figure 4.9. The torque sensitivity is mainly dependent on the shaft diameter and modulus of elasticity of the shaft. For this particular system with a metal bond, the torque sensitivity is 53.5 Hz/Nm. Similarly, the epoxy bonded gauge has a torque sensitivity is 10.55 Hz/Nm (46 ppm/Nm).

The strain sensitivity was also used to estimate the resolution as a function of bandwidth. Previous work [5] has shown that the resolution is a function of the mechanical strain sensitivity of the DETF and phase noise of the SWO. Given the previously measured noise performance of the square wave oscillator board, the resolution of this system is approximately 0.002 $\mu\varepsilon$ (0.0009 Nm) in a 4 kHz bandwidth. Similarly, an epoxy bond gives a resolution 0.01 $\mu\varepsilon$ (0.005 Nm) in a 4 kHz bandwidth.

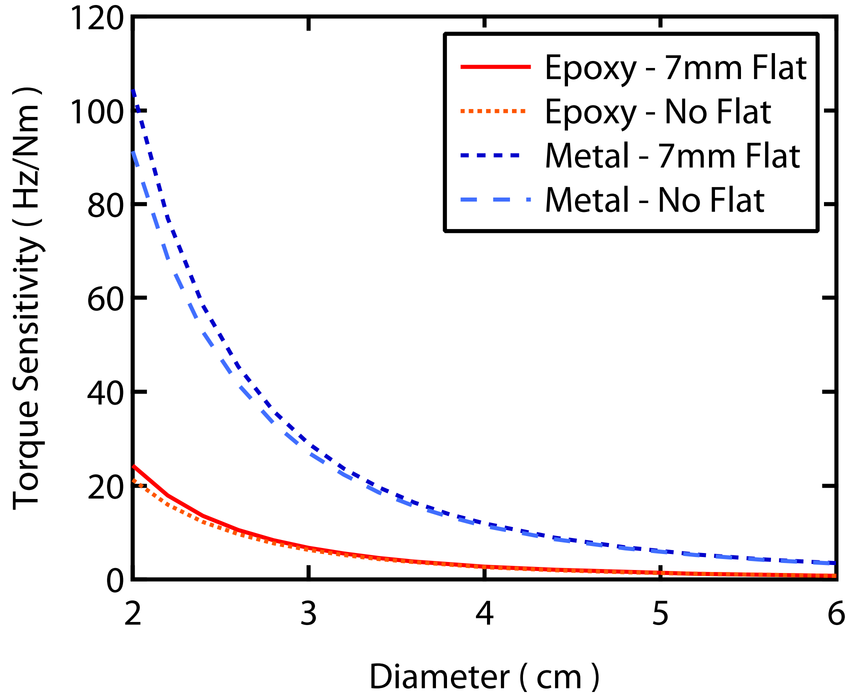

Figure 4.9. Calculated torque sensitivity for various shaft diameters with differing modulus of rigidity. The torque sensitivity has a third order dependence on the shaft diameter.

4.4.2 Temperature Sensitivity

The temperature sensitivity of the metal bond sensor system is 142 Hz/$\mu\varepsilon$, as shown in Figure 4.10 which is equivalent to approximately 5.5 $\mu\varepsilon$/°C error. While this number is fairly significant, it is important to note that this is due to the CTE mismatch between the silicon and steel surface. However, parallel research efforts to create metal MEMS, such as the one outlined in [79, 80] could lead to microscale metal double ended tuning forks which are well matched to their substrate, with significantly lower temperature sensitivities.

The natural frequency as a function of temperature for the epoxy bonded sensor is shown in Figure 4.11. The linear temperature sensitivity of the bonded device with oscillator electronics was measured to be -10.4 Hz/°C (2 $\mu\varepsilon$/°C). For comparison purposes, the frequency response of a resonator with oscillator electronics not attached to any surface was -6.3 Hz/°C . The epoxy result is surprising since a simple linear model would predict that at increased temperature, the steel would tension the gauge, and increase the resonant frequency. This effect is most likely caused by an interaction related to the low strain transfer present in the epoxy bonded gauge.

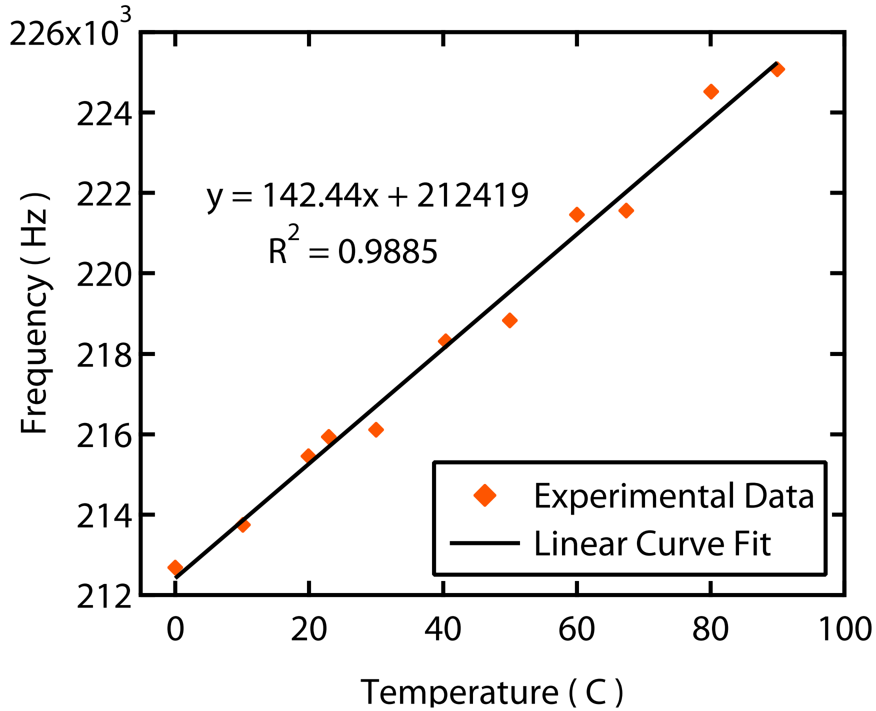

Figure 4.10. Frequency response to temperature with a metal bond. The linear fit is used to provide an estimate of the temperature sensitivity in this range. Bias voltage = 40V.

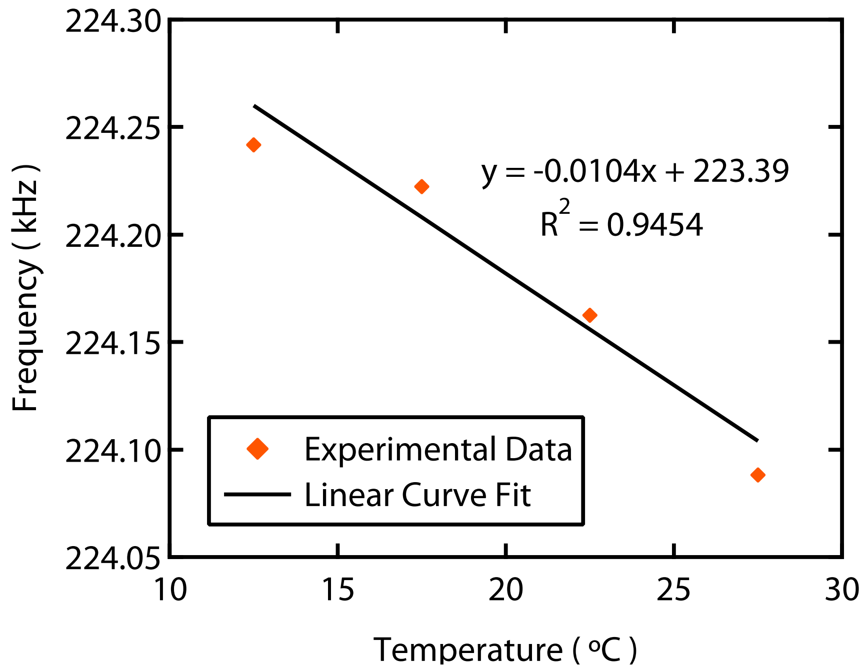

Figure 4.11. Frequency response to temperature with an epoxy bond. The linear fit is used to provide an estimate of the temperature sensitivity in this range. Bias voltage = 40V.

4.5 Discussion

For this testing, a flat was milled into the halfshaft to assist in bonding the MEMS die. For a one-inch component, the flat needed is quite small and has a minimal effect on the stiffness (0.7% reduction) and stress (9% increase) of the shaft. It should be noted that the current MEMS die has not been optimized for strain transfer or torque testing, and that an improved layout would reduce the flat size.

In considering the strain transfer from the component to the actual MEMS device, two strain transfer cases must be considered. First, the strain from the bottom of the component to the top of the die must be considered. Second, the strain from the top of the die into the resonating beams must be considered. More research is needed on the second phenomenon to understand the exact mechanism of strain loss and to improve the strain gauge itself.

The metal bond was able to withstand strains of 1000 $\mu\varepsilon$, and had a strain sensitivity of 26 Hz/$\mu\varepsilon$, which correlated to a torque sensitivity of 53.5 Hz/Nm. The epoxy bond was able to withstand strains of 100 $\mu\varepsilon$, and had a strain sensitivity of 5 Hz/$\mu\varepsilon$, which correlated to a torque sensitivity of 10.55 Hz/Nm. The temperature sensitivities of the gauges was fairly high at 5.5 $\mu\varepsilon/°$C and 2 $\mu\varepsilon/°$C for the metal and epoxy bond, respectively. While these numbers are high, research into devices with better matched CTEs could maintain the high strain sensitivity but reduce the temperature sensitivity.

Chapter 5

Ion Beam Sputtered Silicon Carbide Encapsulation & Film Characterization

5.1 Tuning Fork Encapsulation Issues and Needs

This chapter proposes and tests a novel encapsulation method which is especially suited for MEMS double-ended tuning forks (DETF). The encapsulation uses a novel ion beam sputtering method to seal a scaffolding layer. The scaffolding layer provides structural support for the encapsulation, and is designed to withstand applied pressures while preserving device sensitivity. Furthermore, while using ion beam sputtered material for sealing encapsulation is a promising technique, it is not known if and how much material passes directly through release holes. Experiments in this chapter directly measure the amounts of material, and this method is shown to deposit much less material than typical wafer level encapsulation methods.

Many of the key reasons that tuning forks need encapsulation are highlighted in Figure 5.1. Typical wafer level encapsulation focuses on either novel structural layers or on novel final sealing methods. Regardless, this type of encapsulation typically begins with the deposition of a sacrificial layer, which defines the space between the final device and the encapsulation layer. Next, a structural (or scaffolding) layer is deposited over the sacrificial layer. This structural layer will either possess pores or have lithographically defined holes through which the underlying sacrificial layer(s) may be removed. Finally, the encapsulated

structure will be sealed with a film to maintain the desired internal humidity and pressure conditions.

An interesting class of research has been focused on taking advantage of the porous structure of varying scaffolding layers. Authors have reported on permeable polysilicon [81] or electrochemically etched polysilicon [82]. This technique has also been expanded to use other materials such as silicon dioxide [83], as well as alumina [84]. All of these methods depend on a special material property enabling for a permeable membrane, limiting the available materials for the designer.

For MEMS strain gauges, the encapsulation must protect the underlying device while not significantly changing the device operating characteristics. The resonant frequency and expected strain transfer should remain the same to make a truly manufacturable product. Effective mechanical design can guarantee that the strain transfer is not affected. However, the device resonant frequency would change if mass were deposited on the exterior of the tuning fork. One of the chief problems with current wafer level encapsulation techniques is that the final sealing step tends to deposit mass on the underlying structure, causing the problem mentioned above.

Typically, the final step of monolithic encapsulation involves removing sacrificial layers through release holes and sealing these release holes with a final thin film deposition. Figure 5.2 shows several common final sealing techniques and the typical mass which is deposited using each technique. The techniques based on chemical depositions tend to coat all sides of the MEMS device, since they have a diffusive component. Physical depositions such as sputtering have poor step coverage, and do not efficiently seal release holes. Ion beam sputtering has the unique advantage of being a physical based deposition with good directionality control.

5.2 Ion Beam Deposited Silicon Carbide for Encapsulation

Extensive development has been placed into micro and nanoscale sensors which take advantage of scaling laws and micro and nano physical phenomenon. However, simple monolithic integrated encapsulation remains a key barrier for commercial deployment of these devices. Monolithic integrated encapsulation offers cost savings since it can be created with the same techniques used to pattern the micro and nano devices, saving space, reducing fabrication complexity, and potentially improving yield.

Chemical vapor deposition (CVD) techniques have been used previously [85], but some mass is deposited onto the underlying micro or nano structure as shown in Figure 5.2A&B. Plasma-enhanced chemical vapor deposition (PECVD) has also been shown to have low mass depositions, but have not conclusively proven that there is no mass deposition in

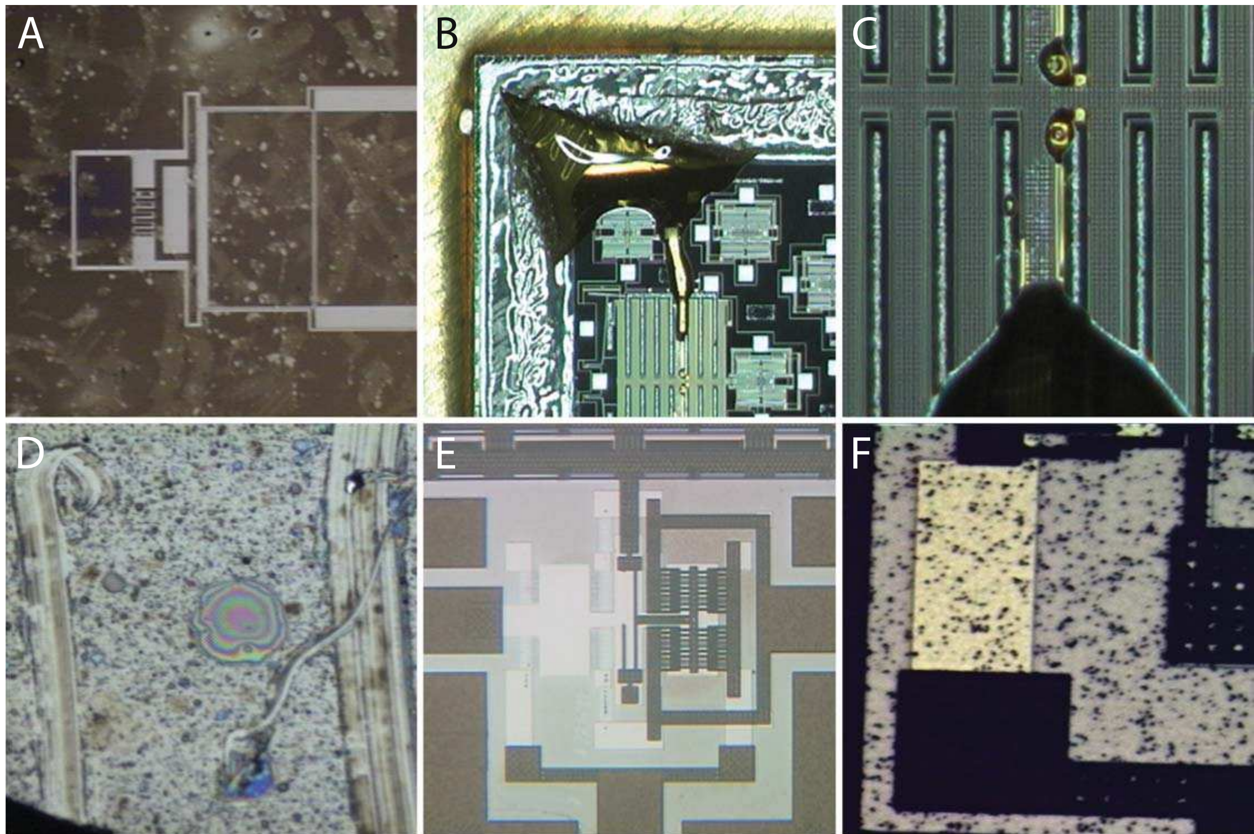

Figure 5.1. Key Issues for Tuning Forks which can be solved with encapsulation A) Oxidation B) Epoxy Bonding C) Liquids D) Oily residue in Engine Environment [30] E) Mechanical Impact F) Dirt

the cavity [86, 87, 88]. Both techniques have a diffusive component, enabling material to deposit conformally within the encapsulation cavity. Some authors have proposed techniques which circumvent mass deposits, but these methods rely on specific nano-pourous material properties [81, 83], require extra processing steps [84], or may only be used with certain materials, such as metals [89]. While microdevices may be designed to accommodate some deposited sealing material, such a deposition would likely be detrimental to the functionality of nanometer sized devices.

To date, ion beam sputtering has been used for a variety of purposes, including nanowire fabrication [90] and ultrathin film deposition [91]. Preliminary results indicate that the technique adequately seals holes and channels [92], but the topography seen in release hole sealing has not been thoroughly examined. Furthermore, the technique may be combined with ion beam assisted deposition to tune a variety material parameters [93, 94, 95, 96].

As an alternative to traditional techniques, this chapter proposes and examines the merits of using ion beam sputter deposition as a final sealing layer. In this technique, high energy ions are streamed towards a target, and the material is sputtered in a mirrorlike manner towards the substrate. The amount of sputtered material leaving the target is a strong

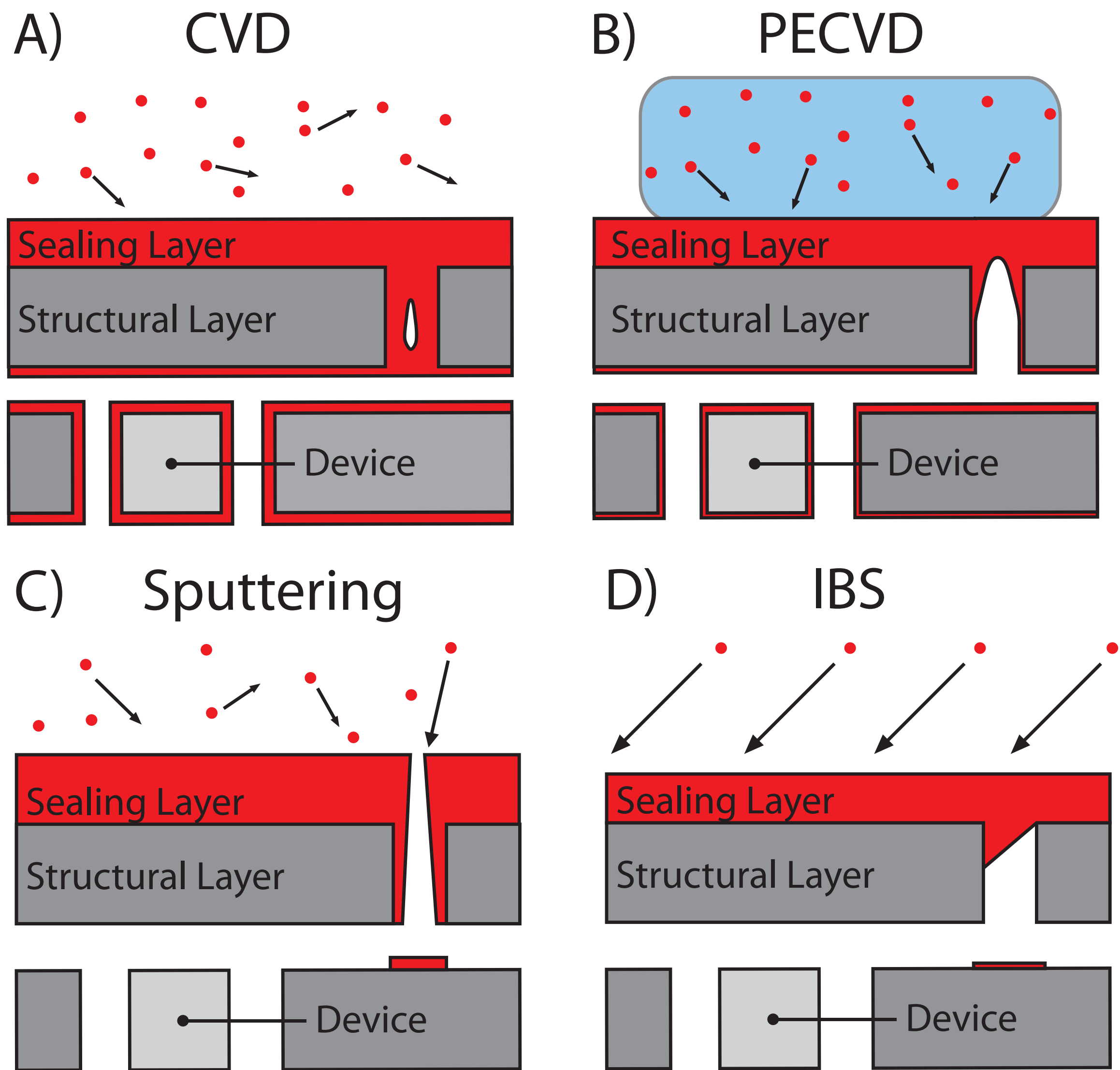

Figure 5.2. Possible sealing methods and their step coverage on a sample micro or nanoscale device. A) Chemical Vapor Deposition (CVD) has a diffusive component which deposits material on the undelying device structure. B) Plama Enhanced Chemical Vapor Deposition (PECVD) still coats the underlying structure, but to a lesser extent when compated with CVD. C) Sputtering, which typically suffers from poor step coverage, resulting in a large amount of material being used to seal the release holes. D) Ion beam sputtering (IBS) enables anglar sputtering of material preventing mass loading of the target device.

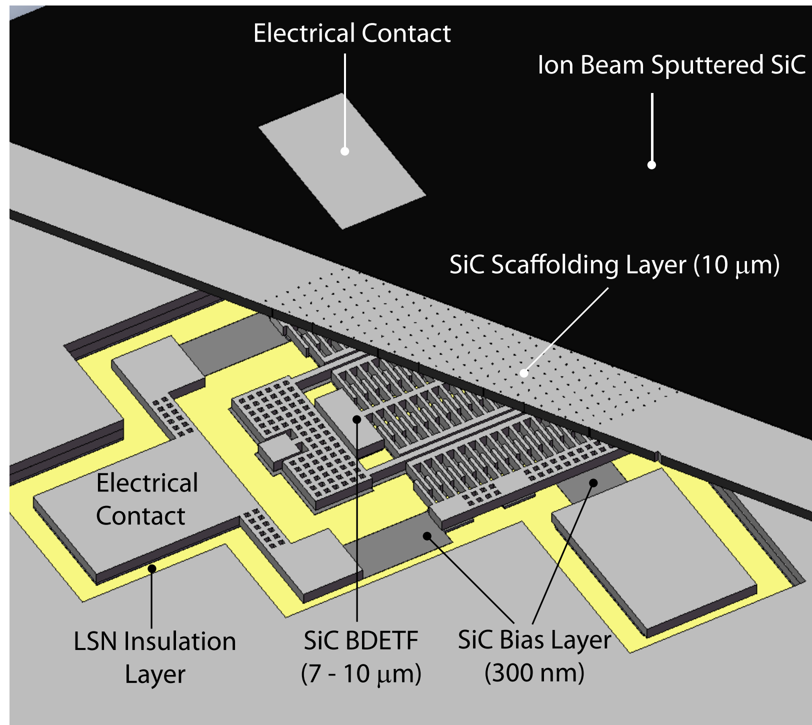

Figure 5.3. View of Ion Beam Deposited SiC Encapsulated Balanced Mass Double Ended Tuning Fork Strain Gauge

function of the angle of departure, unlike traditional sputtering which has a fairly uniform angular distribution. Figure 5.2C shows traditional sputtering with a uniform deposition for all angles, causing a large mass to be deposited below the release hole. In Figure 5.2D, the ion beam sputtering method is shown, showing the highly directional nature of the deposition.

One of the key issues which is not discussed in this work, and would need to be addressed, is the stress typically found in the ion beam sputtered films. It is possible that the high stresses encountered during deposition could cause the encapsulation layer to collapse on the underlying device. However, one approach could involve breaking the final encapsulation sealing step into a series of deposition and annealing cycles.

5.3 Encapsulation Overview & Design

While the ion beam deposited silicon carbide is useful for preventing mass loading (discussed later) and for harsh environment encapsulation, careful attention must still be paid to the mechanical design of the packaging layer. Mechanically, the package must withstand directly applied pressures to facilitate bonding. Furthermore, the package itself should be able to survive the same shocks as the device which it protects. Finally, the package must not attenuate strain measured by the tuning fork.

Ultimately, each of the constraints mentioned above will have some effect on the desired encapsulation thickness. The package must be thick enough not to fracture or deflect into the device, but thin enough to prevent strain attenuation. To find the optimal design, each constraint is examined with respect to encapsulation thickness. The area of the encapsulation will be the minimum area which can adequately cover the device of interest, in this case, a rectangle of 480 μm x 310 μm is modeled. The order in which the analysis is performed is not important, however, at the end of the analysis, each constraint must be considered in order to find an optimal design. In this analysis, it was found that pressure was the active constraint.

Pressure may cause the membrane to fail in two ways: inducing high stresses leading to fracture or inducing high deflections leading to device failure. In this analysis, it is assumed that if the membrane touches the device, failure occurs. Clever device design could create membranes which could purposely deflect into the center of the device area without causing damage. However, this encapsulation was specifically designed for the BDETF discussed in Chapter 2, conceptually shown in Figure 5.3.

Determining exact applied pressure requirement is highly dependent on the final application of the system. Previous authors have suggested that the encapsulation survive 80 atm (for injection molding) [97]. However, the solution to achieving encapsulation capable of surviving high pressures lies in using very thick (20 - 40 μm), fast depositions of silicon [97, 85]. Unfortunately, this option is simply not possible or feasible for existing silicon carbide technology, due to the low deposition rate. This design instead focuses on creating a lid which will survive rough handling and directly applied pressures on the order of 10 atm.

5.3.1 Stress & Deflection Calculation

The scaffolding or structural layer of the encapsulation is analytically modeled as a flat diaphragm in this analysis. This layer will be created from LPCVD SiC, have lithographically defined release holes, and will be subsequentle sealed with ion beam sputtered SiC, as shown in Figure 5.3. Once an optimal thickness for the scaffolding layer is determined, the design can be further refined to include release holes and potential stress concentrations using FEM. Both the stress and the deflection for a square membrane undergoing a uniformly distributed load have been derived previously by Roark [76], and a concise form of the solution is given below for convenience.

$$y_{max} = \frac{\alpha q b^4}{E t^3} \tag{5.1}$$

$$\sigma_{max} = \frac{-\beta q b^2}{t^2} \tag{5.2}$$

where q is the distributed load expressed in force per area (in this case pressure), t is the thickness, b is the length of the short edge. The equation also includes, α and β, which are

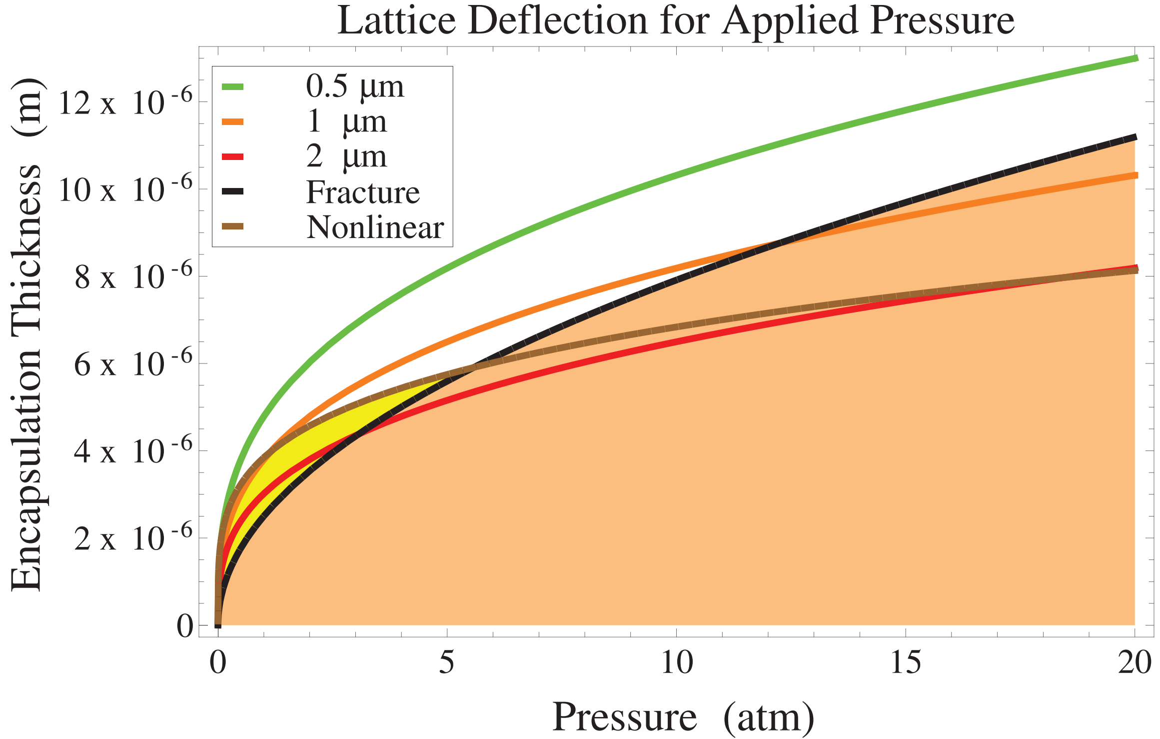

Figure 5.4. Design Graph for the Maximum Deflection of a membrane and fracture stress for SiC as a function of applied pressure. Below the line marked "Fracture" the membrane will fail. Also, in the area below "Nonlinear", additional calculations would be necessary to find the exact failure points.

factors which account for the rectangular shape of the membrane and are functions of the geometry of the membrane. For a perfect square, β is 0.3078, increasing to 0.5 as the long side to short side ratio approaches infinity. Similarly, α is 0.0138 for a square membrane, increasing 0.0284 as the long side to short side ratio approaches infinity [76].

Equation 5.1 is re-arranged to solve for the necessary thickness for a given deflection at a given pressure. Figure 5.4 shows the needed thickness for several maximum deflection constraints (1, 1.5, and 2 μm). In designing encapsulation, these deflection constraints are dependent on the sacrificial layer thickness above the device of interest and below the scaffolding layer. For oxide, 1-2μm was considered a reasonable thickness. Young's Modulus, E, has a a wide range of reported values, from 283 GPa [98] to 448 GPa [67]. In this case, an average value of 360 GPa was used.

Equation 5.2 is re-arranged to solve for the minimum thickness in which the maximum stress is equal to the fracture stress, also shown in 5.4. The fracture stress can be difficult to determine in microspecimens since this number is inherently dependent on the film quality and the number of defects. In this case, an average value of 0.17% was assumed to be the fracture strain, and the same Young's Modulus was used to convert to fracture stress.

5.3.2 Nonlinear Considerations

It is important to remember that for a flat diaphragm, Roark's solution involves linear assumptions. For high deflections and thin membranes, shear forces must also be considered, creating a nonlinear response. This has also been solved for previously by Giovanni [99]. In looking at these solutions, the nonlinear solution typically reduces the maximum deflection and maximum stress. However, for conservative engineering design, it is important to note where the nonlinear response begins. In Giovanni, the condition for linearity is given in equation 5.3, and this condition is plotted in Figure 5.4.

$$\frac{Pb^4}{Et^4} \leq 10 \tag{5.3}$$

5.3.3 Shock Survivability

In considering shock survivability, it is helpful to begin by estimating a shock force. While the designer must be careful to distinguish between dynamic and static shock events, static loads are simple to estimate and are a useful place to begin the analysis. The distributed load is estimated as the density times the thickness times the shock factor. To make comparisons between the different constraints easier, the distributed load due to shock can be rewritten as an equivalent pressure. For this diaphragm, a shock of 100,000 G on a 50 μm thick membrane will produce a maximum force which is equivalent to that applied by 1.6 atm. Since the diaphragm will be designed to survive much higher pressures, it was concluded that shock is not an active constraint for typical wafer level encapsulation.

5.3.4 Encapsulation Effect on Strain Transfer

Determining the effect of the encapsulation on strain transfer is key to an effective design. A 2D COMSOL model was constructed to give insight into how strain transfer would be affected by a "lid" on the device. From these models, several important design rules were learned. First, the presence of the strain gauge tends to locally stiffen the measurement area, reducing the measured strain. For example, a silicon strain gauge attached to a steel surface under a specified strain will tend to measure less than the specified strain. A complete analysis of this can be found in [35]. However, this local stiffening can be counteracted by a slight moment induced in the strain gauge, which can amplify the strain experienced by the substrate. This is especially important for thick substrates with very thin encapsulation caps. Finally, unless the encapsulation is the same thickness as the substrate, there will be a minimal effect on the strain transfer. In cases of a thin cap on a thick substrate, it is the substrate which has the greatest effect on the strain transfer. Hence, the key to getting good strain transfer depends on creating first a thin substrate, and second minimizing the encapsulation thickness.

Ultimately, a thickness of approximately 7 - 10 μm was chosen as an appropriate thickness for this device. Using Figure 5.4, a 10 μm film will only deflect 0.5 μm at 10 atm, and will not fracture until 17 atm. This thickness provided adequate protection from pressure, and also was a reasonable thickness for the scaffolding layer using today's LPCVD SiC production processes. This thickness survives high shocks. Furthermore, this encapsulation has little additional effect on the strain transfer properties of a gauge constructed on a standard 500 μm thick substrate.

Once this thickness was chosen, the next step of design was centered around determining how much mass would be deposited through the proposed release holes shown in Figure 5.3. Since this would be the last step of a seven to eight mask process, simple test structures were designed to measure this mass.

5.4 Through Hole Deposition Experimental Testing

Previous work has shown that ion beam sputtering of silicon carbide can be used to seal both trenches and holes in a silicon wafer [92]. From images of the sealed trenches, it is seen that the ion beam sputtered deposition is highly directional, but there is a small lateral deposition rate. If the material were deposited uniformly from a single direction, the trench or hole size would propagate uniformly through the film. While this would eventually seal the trench, the top of the film would still have a hole or trench shaped object in it. However, this is not the case. Instead, as the sealing layer becomes thicker, the hole size reduces. This phenomenon indicates that material must be depositing from other directions. These other depositions can also be the source of mass deposition through the release holes.

Hence, to test the mass depositions, release holes would have to be created below a very flat, clean surface. This type of surface would ease the discovery of any mass depositions. Also, if the release holes are made at a repeating distance, any mass depositions must also have a similar pattern of repetition. A perfect structure to use for these mass deposition experiments was a silicon-on-insulator (SOI) wafer. Holes could be patterned in the device layer, and once released, the underlying substrate is quite smooth. This experimental device is shown in Figure 5.5

Since the holes were lithographically defined a number of experiments examining the deposition as a function of hole size, aspect ratio, and the time could be simultaneously performed. Arrays of holes of different sizes were patterned in SOI wafers with silicon layer thicknesses of 3.5 μm and 6.5 μm. The arrays had square holes of 1, 1.5, and 2 μm on a side, creating aspect ratios ranging from 1.75 to 6.5. The 2 μm thick underlying oxide layer was then etched using a vapor hydrofluoric acid (HF) release to create a diaphragm. Directional ion beam sputtered amorphous silicon carbide (SiC) was then deposited onto the membranes at incident angles of 0, 45, and 55 degrees for 80 minutes, giving a film thickness of 0.4 μm. Time trials were also performed at an angle of 45° on the 3.5 μm thick silicon layer devices with deposition times of 5, 10, 20, 40, and 80 minutes. This angle was chosen since

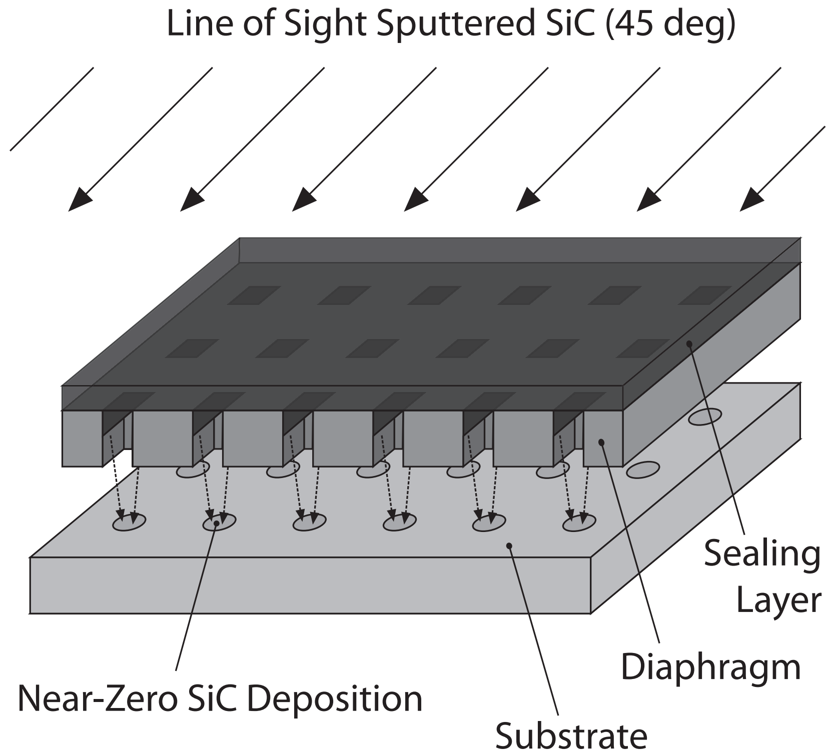

Figure 5.5. Experimental Setup and Deposition Step Overview

the sidewall deposition and top surface deposition amounts should be the same, providing information about the influence of the hole sealing on the underlying mass deposition. The diaphragms were subsequently removed and the underlying structure was examined using scanning electron microscopy (SEM) and atomic force microscopy (AFM).

Sputtering was performed using a custom built ion beam sputtering tool for micro and nano applications. The angle of sputtered material incidence may be changed from 0° to 55° using a tilting stage. In this case, argon ions with an energy of 1.175 keV and a current of 0.5 A were used. The base pressure of the system was 1 x 10^{-6} Torr, and the operating pressure was approximately 1x10^{-4} Torr. Rutherford Backscattering Spectroscopy (RBS) confirmed that the films have a 1:1 ratio of silicon to carbon, indicating that the film was indeed SiC. Additional details on the sputtering system are given in [92].

5.5 Mass Loading Results

5.5.1 Deposition Spatial Confinement

In all cases, it was found that the all material was spatially confined directly below the release hole. Figure 5.6 shows experimental confirmation of the spatial confinement seen on all test structures. The area in between deposits is atomically smooth as measured by AFM, as seen in Figure 5.7A. By using SiC, the spatial confinement could be tested by dipping the substrate with the mass deposits into potassium hydroxide (KOH), which preferentially etched the exposed silicon areas as shown in Figure 5.7B.

For comparison purposes experiments were performed using samples coated with 250 nm of PECVD SiN (SiC was unavailable) with an Oxford Plasmalab 80plus PECVD system, at 0.9 Torr and 350°C. It may be possible to improve the recipe for encapsulation purposes as seen in [87], but these coatings are fundamentally conformal coatings. As expected, material was deposited everywhere inside the cavity, with concentrated masses below the release holes. In the best case, the films were optically transparent and could not be measured using a Nanospec/AFT Model 3000 interference spectrum measurement system. However, these films were thick enough to protect the underlying silicon substrate and only KOH etching through pinholes was observed.

5.5.2 Deposition Shape Analysis

Further analysis of the AFM data for various release hole depths and areas showed that the release holes had several repeating topological features, which changed depending on the release hole size and shape as well as the deposition conditions. First, the spatial confinement of all the release holes appears to be due to shadowing effects. That is, considering the geometries of the release hole and the angles of deposition, all deposition is confined to areas which have direct line of sight with the sputtering target. The variation in the width of the deposit is given in Figure 5.8

Also, all mass depositions had a relatively flat area of constant height, but some depositions also had a characteristic peak, which is shown in the inset of Figure 5.9. This peak was often significantly taller than the flat area, and tended to appear below release holes with a low aspect ratio.

The time trial experiments give insight into the nature the deposition formation, as shown in Figure 5.10. The initial shape contains information about the angles of distribution available from the source seen in Figure 5.10A. More material is being sputtered on the left hand side of the deposit, as seen by the slightly higher deposition amount. Also, the initial area taken up by the deposition remained fairly constant with time. However, a peak shape appears with increasing time, starting wide and becoming narrower. The shape is presumably

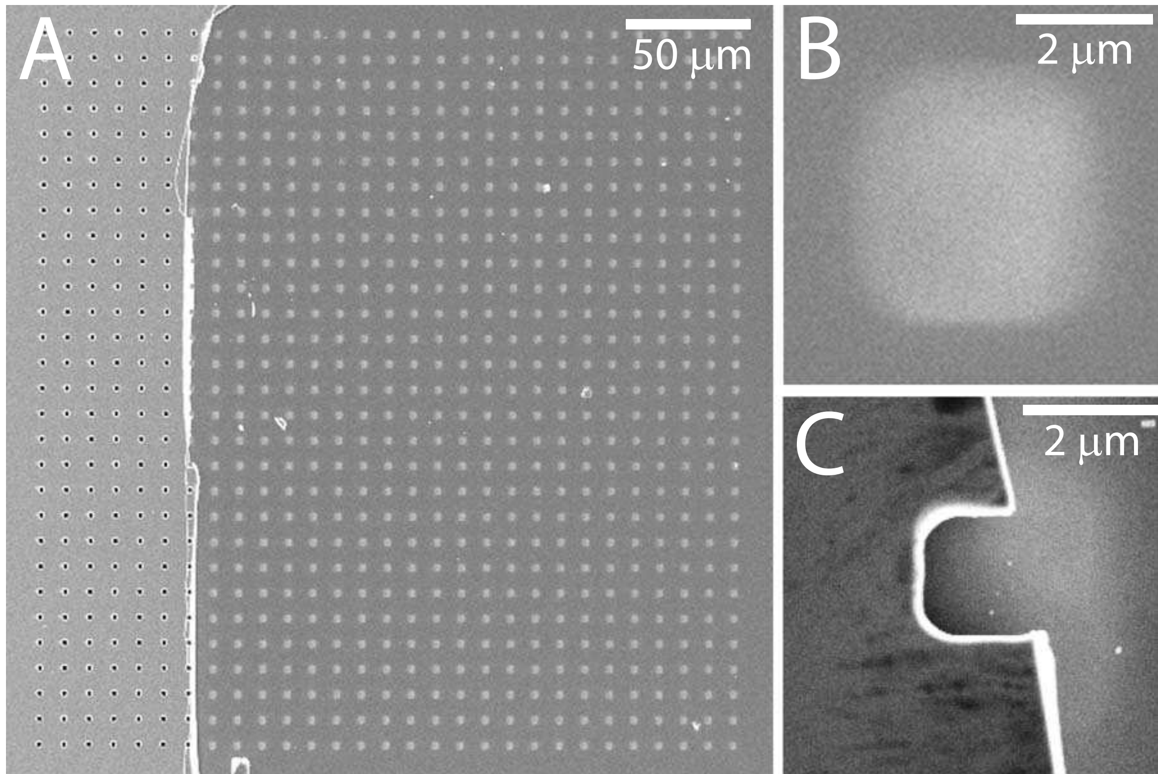

Figure 5.6. SEM of test structure (A) The top diaphragm containing release holes has been cracked and partially removed. The deposition on the substrate is very thin, well spaced, and regular. (B) Deposition on the substrate and (C) the deposition partially below a release hole.

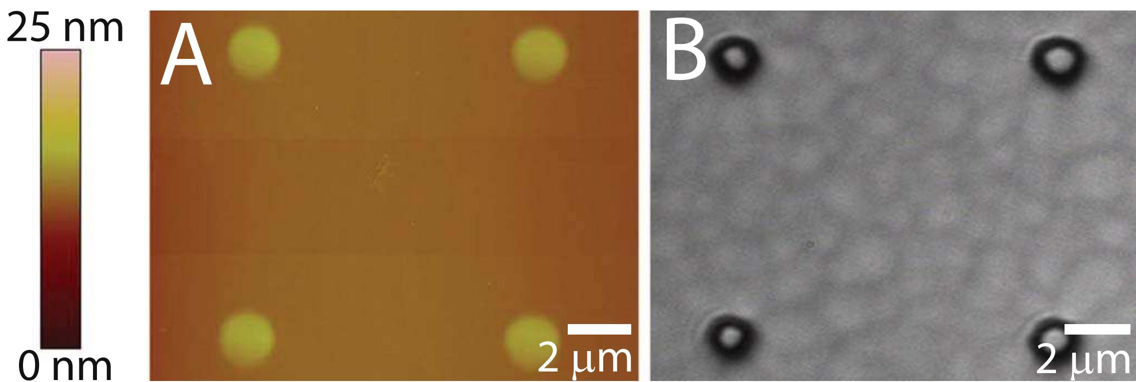

Figure 5.7. (A) AFM image of the diaphragm area before potassium hydroxide (KOH) dip. (B) Optical image after KOH dip. The resulting SiC-capped islands confirm the spatial confinement.

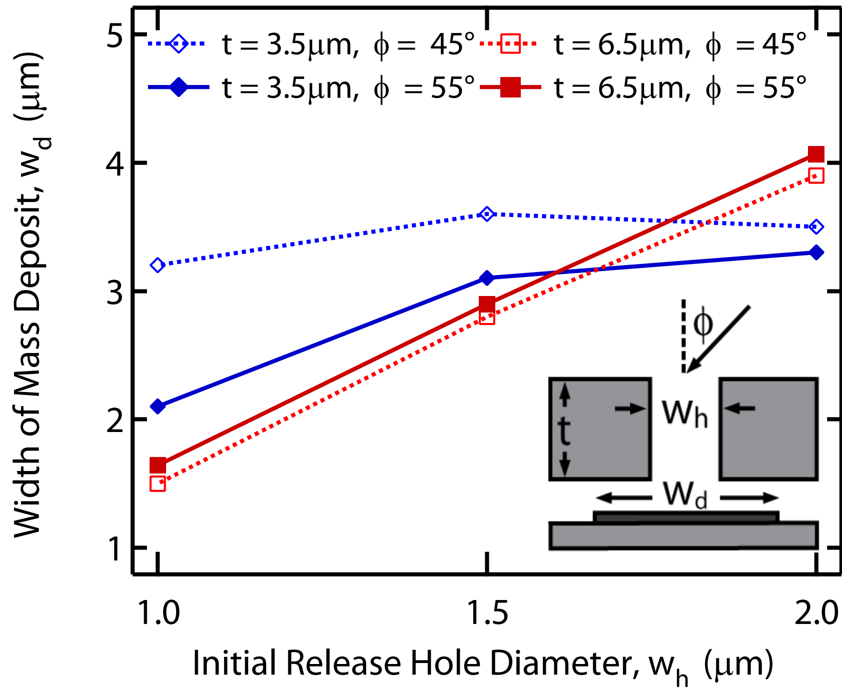

Figure 5.8. Measurements of the mass deposit width after 80 minute deposition show that the deposits are spatially confined, and all deposited by off-axis direct line of sight depositions.

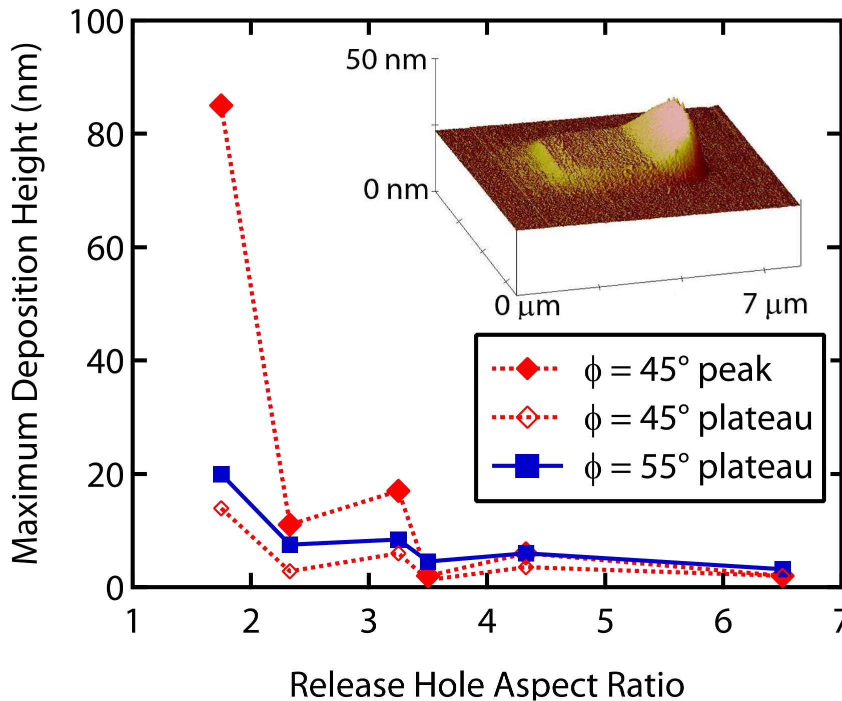

Figure 5.9. Measurements of the heights of the deposits after 80 minutes show that the height is quite small when compared to the top surface (0.4 μm). The characteristic peak is formed for the 45°, and all depositions have a characteristic flat region which increases in height with time

from the release holes above closing off and shadowing effects which enable less material to enter into the release hole itself.

Given these two observations, the shape of the deposition can be explained by considering Figure 5.11. Argon ions (not pictured) strike the sputtering target creating a distribution of sputtered material which has a range of directions and deposition rates, represented by the arrows on the sputtering target. Some excellent pictures of this as well as information about Monte Carlo simulations can be found in [100]. When considering the range of deposition angles and deposition rates, only certain angles will geometrically be able to pass through the release hole. The blue triangular shapes show what material may actually enter the release hole for two different situations in Figure 5.11 A & B. In examining the low aspect ratio hole in Figure 5.11 A, it is seen that both a wider range of particle trajectories and amounts for a given direction are much higher than those seen in Figure 5.11 B. It is this range of both directions and differing deposition rates which is responsible for the peak development. The narrowing of the peak is caused by the release hole above sealing with time.

It is possible for other deposition parameters such as pressure and temperature to have an effect on the deposition. For the RF ion source used in these experiments, it is necessary to keep low pressures. In this case, all pressures were low enough such that the mean free path distance is larger than the source to wafer distance. As such, it is not possible to examine the effect of this on the deposition. Depositions were performed and both room temperature and 450°C, and no measurable change was found in the shape of the deposition. However, increasing temperatures further could change the shape of the deposition by possibly enabling some surface diffusion.

5.5.3 Mass Estimates

Finally, using the AFM data, a mass analysis was performed on the time trial data to estimate the amount of mass per release hole and also to ascertain how the mass increases with time. Four mass deposits, next to one another, were analyzed to ensure that an average was measured. In examining Figure 5.6, it is seen that the masses are fairly uniform over the diaphragm area. Since the masses were 10 μm apart, a 20 μm x 20μm scan captured four masses and the surrounding flat area. Each scan consisted of a 512 x 512 array of measured heights. Therefore, each data point represented the average height over an area of 0.039 μm x 0.039 μm (20 μm $\div$ 512 μm). Hence, the volume of each area was simply the height times the area represented by each data point. By multiplying this volume by the density of silicon carbide, assumed to be 3150 kg/m^3, the mass was determined.

In performing the above analysis, the zero point and the presence of noise or dust needs to be considered. First, in examining the AFM data, there is some error in the zero point. In looking at areas which are far from the mass deposits and which should be very flat (since the area is single crystalling silicon), there will often be an offset. In otherwords, the height should read zero in this area, but will instead be slightly away from zero. In this case, this offset is present throughout the entire data set, and was removed.

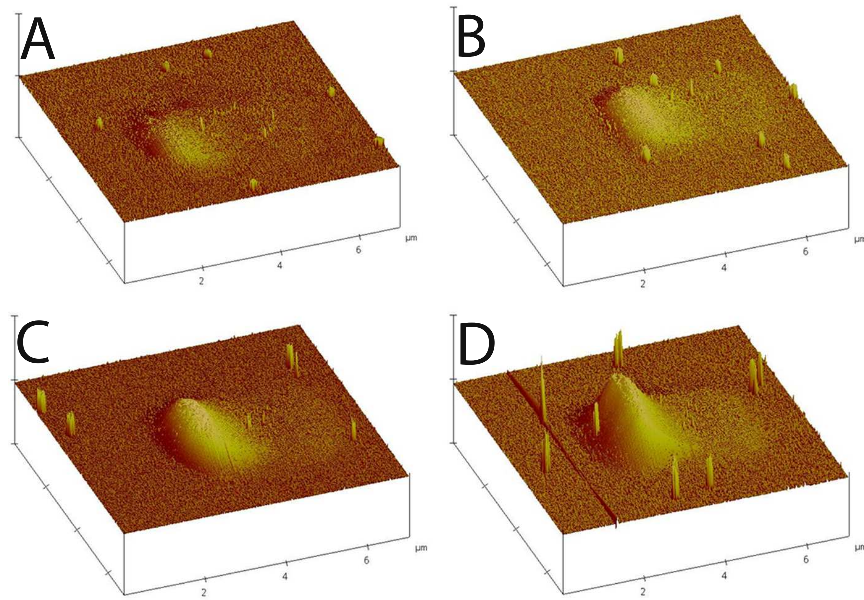

Figure 5.10. A) - D) Time evolutions of the 3.5 μm thick diaphragm and 2 μm square release hole showing the characteristic peak and plateau deposition region. The plateau region appears early and contains information about the range of deposition angles, where as the peak is indicative of the narrowing of the release holes.

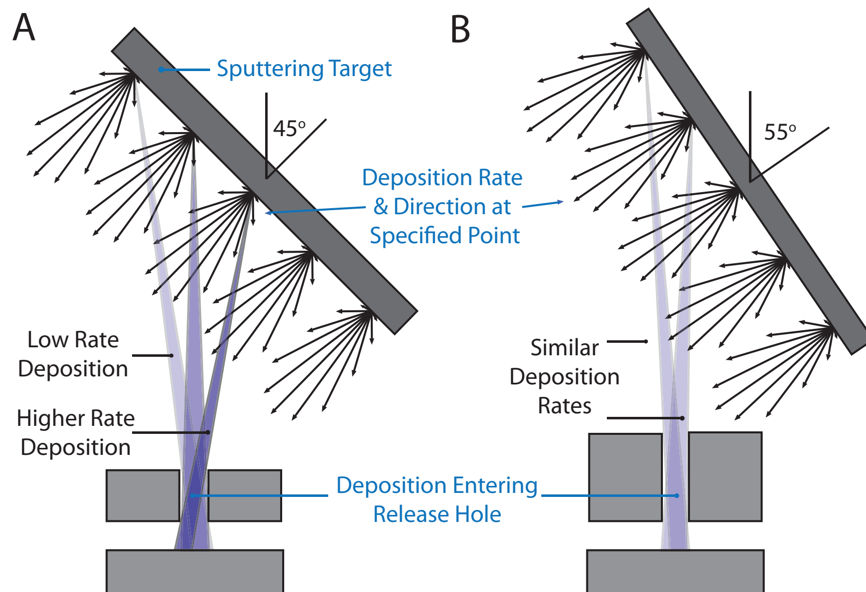

Figure 5.11. The deposition rate and angle greatly affect the shape of the mass deposits A) The 45 degree angle allows some direct, high rates of deposition to pass directly through the release hole. B) With higher deposition angles, the amount of material entering the release hole is reduced.

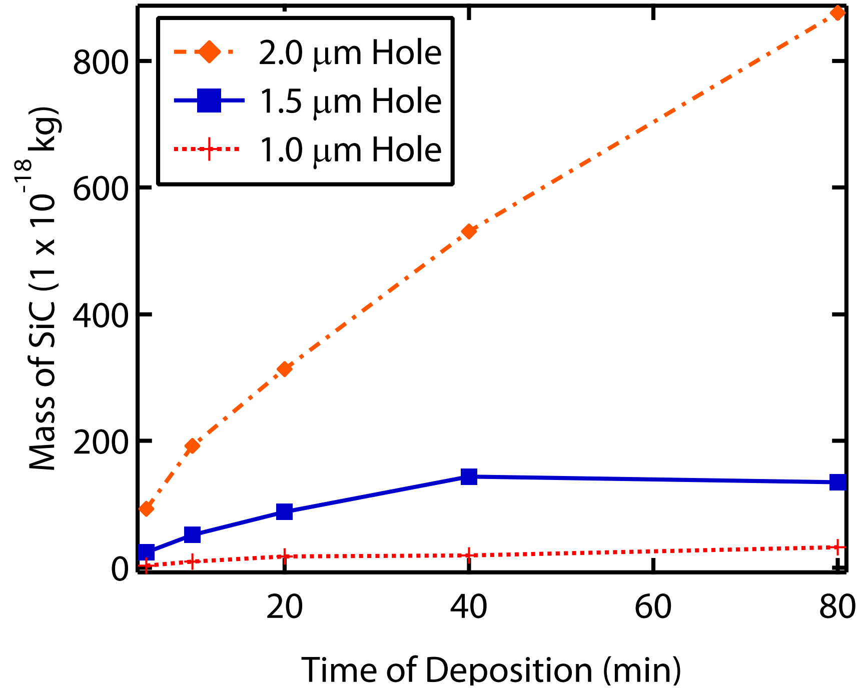

Figure 5.12. The mass depositions for a 3.5 μm diaphragm approach a constant value indicating that the top hole is sealing and that the mass flux is being reduced with time

The process of breaking the diaphragms and removing them with tape often created sparse small particulates in the AFM scan which were often much taller than the other data. It was determined that these were particulates since they appeared in a random fashion and were of varying quantity. To remove these particulates from the data, it is useful to use a program such as MATLAB or IgorPro. In this case, the particle analysis toolkit in IgorPro was used. Since the area of the particles or noise was quite small (typically a few pixels), the volume of these particle areas was neglected. Alternatively, one could interpolate the value of the heights of the pixels obscured by particles. However, it was found that the error between interpolation and simply ignoring these pixels was minimal for this analysis.

Figure 5.12 summarizes the mass measurement results, showing that the rate of mass accumulation decreases with time. This phenomenon is expected since the release holes are closing with time. Also, the rate of accumulation reduction itself is dependent on the hole size. Since a constant 0.4 μm of material is deposited over the course of the experiment, larger holes enable much larger amounts of material to pass through. Also, considering Figure 5.11, the hole is being preferentially sealed on the same side as the peak expected below the mass deposit.

5.6 Discussion

Analyzing data from the width, height, and shape of mass deposits, the deposition in ion beam sputtering is from a narrow range multi-angled deposition. Much of the material is deposited in a single direction with additional lower deposition rates occurring in lateral directions. Since there is a continuous distribution of material being sputtered onto the wafer, the size and aspect ratio of the release hole is key to reducing the amount of material deposited through the release hole. High aspect ratio release holes only allow direct line of sight sputtering from very low rate angles. As such, this allows the material deposited through the release hole to be on the order of nanometers thick, while the top surface has approximately 400 nm of material deposited. Part of the reason for the mass deposition in the release holes is the very large size of the target relative to the size of the wafer. However, this is needed to create uniform sealing depositions along the entire wafer.

Using the estimated masses, it is possible to calculate expected frequency shifts on a standard double ended tuning fork. Preliminary calculations indicate that the frequency shifts expected for these mass depositions are quite small given the large comb drive mass. Also, since the depositions are spatially confined, release holes may be placed very close to the device to enable quick release and zero mass loading. Given these results, encapsulation suitable for nanoscale structures is both feasible and possible.

Chapter 6

Conclusions & Future Work

This thesis resolves four key systems level issues which have prevented MEMS double-ended tuning forks (DETFs) from being used in commercial settings as strain gauges. By examining each issue individually, but with a systems level perspective, a series of design improvements were made in the gauge that did not sacrifice performance. By using silicon carbide, it was possible to create a harsh environment compatible DETF which retained the favorable strain sensing characteristics of a comparable silicon DETF. From this research, a novel temperature compensation technique was discovered which takes advantage of thermally induced strains to counteract changes in the modulus of elasticity. The thesis also explored the first high strain testing of a MEMS DETF mounted on an automotive halfshaft for torque sensing. Finally, an encapsulation scheme is designed around a novel ion beam sputtering deposition sealing step, and shown to have very low mass depositions through release holes. Each of the sections below comments on the key insights learned and offers suggestions for future work.

6.1 Improved Harsh Environment Survivability

Chapter 2 demonstrated that a harsh environment strain gauge could be fabricated which retains high strain sensitivity (66 Hz/$\mu\varepsilon$) and resolve 0.1 $\mu\varepsilon$ in a 10 kHz bandwidth. Furthermore, it was shown that an alternate material stack which utilizes silicon nitride rather than silicon dioxide works well with SiC up to 600°C. Testing required custom built and specialized equipment, such as a platform to locally heat dies, and a light gas gun. Using a light gas gun, shocks of 64,000 G were achieved, and much higher shocks are possible using this equipment setup. From this data, it was shown that the shock modeling methods proposed by Azevedo [3] are valid up to 64,000 G.

Some of the areas for improvement are centered around the etching and materials properties of SiC. Special care needs to be taken in adapting silicon based tools for SiC, especially in regards to improving etch quality. The chief difficulty with etching SiC is finding CMOS compatible etch materials which provide vertical sidewall etching. Additional materials research is warranted to improve the quality factor of poly-SiC. This research found that the quality factor is 10 times lower than quality factors of the same DETF created in silicon. More research is needed to understand the reason for the low quality factor, but slanted and rough sidewalls, interfacial layers, and grain size are believed to be possible culprits.

6.2 Temperature Stability & Compensation

The traditional temperature dependence of tuning forks is fairly linear over most temperature regimes, and is dominated by changes in the modulus of elasticity. By inducing thermal strains, the temperature compensation scheme presented in Chapter 3 trades this linear temperature dependence for a parabolic temperature dependence. However, the linear temperature sensitivity of tuning forks has been reduced approximately 10 fold over a 50 degree range without compromising the strain sensitivity of the device. The method of purposely mismatching device and substrate materials is simple to implement and preserves the strain sensing properties of the double ended tuning fork used in this work. The key to this temperature compensation technique is considering the coefficients of thermal expansion (CTE) of different materials as a function of temperature. Ideally, there will be a small, consistent CTE difference to compensate for a modulus change. However, in the absence of that, looking for cross-over points in the CTE data will also lead to temperature compensation.

Given the initial success seen in this area, more research into different material combinations is warranted. The analytical model proposed in this chapter could be reapplied to other material combinations with little additional effort. For example, a precursory glance at aluminum nitride (AlN), shows similar modulus trends and CTE trends to SiC. AlN is currently being studied for harsh environments, and could benefit from this temperature compensation scheme, although some extensions may be necessary to account for the metal electrodes needed for AlN actuation. However, as mentioned before, the exact value of the CTE and small differences in the data provide for large changes in temperature compensation. More accurate measurements of CTE, and especially data on how much variation can exist using different film deposition techniques would be especially useful.

6.3 High Strain Torque Testing

Chapter 4 presented the first high strain testing of a DETF, proving their viability in a multitude of situations. Initial tests show tuning forks operating at high strains of 1000 $\mu\epsilon$ show that the device can be readily adapted for use as a torque sensor. For the halfshaft used in this experiment, a strain sensitivity of 54.86 Hz/Nm (253 ppm/Nm) was achieved, with a resolution of 0.0009 Nm in a 4 kHz bandwidth. It was also shown that epoxy bonding is good for situations when strains less than 100 $\mu\epsilon$ are expected. In adapting the tuning fork for torque sensing, a flat placed on a circular object requires a minimal amount of additional manufacturing and does not substantially change the objects strength or stiffness.

When using a MEMS DETF it is important to consider two areas of strain transfer. First, the strain transfer from the object to the die surface must be considered. In this area, work has already been performed on flat substrates [35], and initial work on circular substrates has been presented here. Next, the strain transfer from the top surface of the die into the resonating beams must be considered. Future work should focus on full models of the DETFs under high strains. Studies should focus on the anchor-block structure to understand how strain is coupled from the top of the die to the vibrating beam structure. It is also interesting to note that the anchors themselves could place a moment on the tuning fork structure. Studies examining this area and the effect on the tuning fork could be of interest as well. Also, when bonded to an object with a substantially different coefficient of thermal expansion, large thermal strains will be present. However, research into metal DETFs fabricated on metal susbrates could solve this issue, enabling good CTE matching.

6.4 Low Mass Loading Encapsulation

In Chapter 5 encapsulation which could successfully protect a DETF without attenuating the strain sensitivity of the device was developed. The encapsulation is composed of two parts, a structural layer and a sealing layer created with ion beam sputtered material. Analytical studies of the structural layer show that the layer can be designed such that it protects the DETF without attenuating the strain. To do this, it is necessary to consider both the maximum allowed deflection and the maximum stress in the layer. Furthermore, initial studies found that encapsulation thicknesses less than that of the substrate minimally effect the strain transfer.

One of the key advantages of using ion beam sputtering to create the sealing layer is the highly directional nature of the deposition. This highly directional deposition enables very thin, spatially confined depositions below the release holes. Testing structures in this experiment revealed that mass deposited through release holes is 400 times thinner than the material deposited on the scaffolding layer. The material deposited through the release hole is by line-of-sight deposition and is found to be dependent on the aspect ratio and size of the release hole, as well as the angle of deposition. Given that the encapsulation is spatially

confined, it would be especially useful in nanoscale structures. One of the main concerns which needs to be addressed is the high stresses present in the ion beam deposited films. Initial annealing results have shown that annealing is a promising avenue to reduce these stresses, but more research is needed to draw more definitive conclusions.

This thesis presented a number of design improvements for the MEMS DETF strain gauge. It also validates new operational limits, showing that these devices are capable of operation at high temperature and under high strain. Given the increased understanding of the performance of the gauge, and the added improvements proposed in this thesis, it is now possible to consider developing a commercially deployable MEMS strain gauge.

Bibliography

[1] H. C. Nathanson, W. E. Newell, R. A. Wickstrom, and Jr. Davis, J. R. The resonant gate transistor. *Electron Devices, IEEE Transactions on*, 14(3):117–133, 1967.

[2] Robert G. Azevedo, Wayne Huang, Oliver M. O'Reilly, and Albert P. Pisano. Dual-mode temperature compensation for a comb-driven MEMS resonant strain gauge. *Sensors and Actuators A: Physical*, 144(2):374–380, 2008.

[3] Robert G. Azevedo, Debbie G. Jones, Anand V. Jog, Babak Jamshidi, David R. Myers, Li Chen, Xiao-an Fu, Mehran Mehregany, Muthu B. J. Wijesundara, and Albert P. Pisano. A SiC MEMS resonant strain sensor for harsh environment applications. *IEEE Sensors Journal*, 7(4):568–576, 2007.

[4] David R. Myers, Kan Bun Cheng, Babak Jamshidi, Robert G. Azevedo, Debbie G. Senesky, Li Chen, Mehran Mehregany, Muthu B. J. Wijesundara, and Albert P. Pisano. Silicon carbide resonant tuning fork for microsensing applications in high-temperature and high g-shock environments. *Journal of Micro/Nanolithography, MEMS and MOEMS*, 8(2):021116, 2009.

[5] Kenneth E. Wojciechowski, Bernhard E. Boser, and Albert P. Pisano. A MEMS resonant strain sensor operated in air. In *MEMS 2004*, pages 841–845, 2004.

[6] B. Beihoff. A survey of torque transduction methodologies for industrial applications. In *Pulp and Paper Industry Technical Conference, 1996., Conference Record of 1996 Annual*, pages 220–229, 1996.

[7] Richard S. Figliola and Donald E. Beasley. *Theory and Design for Mechanical Measurements*. John Wiley & Sons, 3 edition, 2000.

[8] *Strain Gage Selection: Criteria, Procedures, Recommendations.* Vishay Precision Group, tech note tn-505-4 edition, 2010.

[9] V. Kalinin, G. Bown, J. Beckley, and R. Lohr. Pulsed interrogation of the saw torque sensor for electrical power assisted steering. volume 3, pages 1577 – 1580, Aug 2004.

[10] D. C. Betz, G. Thursby, B. Culshaw, and W. J. Staszewski. Advanced layout of a fiber bragg grating strain gauge rosette. *Lightwave Technology, Journal of*, 24(2):1019–1026, 2006.

[11] M. Suster, Guo Jun, N. Chaimanonart, W. H. Ko, and D. J. Young. A high-performance mems capacitive strain sensing system. *Microelectromechanical Systems, Journal of*, 15(5):1069–1077, 2006.

[12] Charles S. Smith. Piezoresistance effect in germanium and silicon. *Physical Review*, 94(1):42, 1954. Copyright (C) 2010 The American Physical Society Please report any problems to prola@aps.org PR.

[13] Gajendra Shekhawat, Soo-Hyun Tark, and Vinayak P. Dravid. Mosfet-embedded microcantilevers for measuring deflection in biomolecular sensors. *Science*, 311(5767):1592–1595, 2006.

[14] R. M. White and F. W. Voltmer. Direct piezoelectric coupling to surface elastic waves. *Applied Physics Letters*, 7(12):314–316, 1965.

[15] V. Avramescu, C. Bostan, B. Serban, I. Georgescu, S. Costea, N. Varachiu, and C. Cobianu. Surface acoustic wave devices and their sensing capabilities. In *Semiconductor Conference, 2009. CAS 2009. International*, volume 1, pages 27–36, 2009.

[16] Jr. Ballantine, D. S., R. M. White, S. J. Martin, A. J. Ricco, G. C. Frye, E. T. Zellars, and H. Wohltjen. *Acoustic Wave Sensors - Theory, Design, and Physico-Chemical Applications*. Elsevier, 1997.

[17] V. Kalinin, R. Lohr, and A. Leigh. Development of a calibration procedure for contactless torque and temperature sensors based on saw resonators. In *Ultrasonics Symposium, 2008. IUS 2008. IEEE*, pages 1865–1868, 2008.

[18] Lee Chang-Hoon and A. Lal. Integrated optical longitudinal strain sensor on a micromachined silicon longitudinal mode transducer. In *Ultrasonics Symposium, 1999. Proceedings. 1999 IEEE*, volume 1, pages 467–470 vol.1, 1999.

[19] W. Y. Li, C. C. Cheng, and Y. L. Lo. Investigation of strain transmission of surface-bonded fbgs used as strain sensors. *Sensors and Actuators A: Physical*, 149(2):201–207, 2009. doi: DOI: 10.1016/j.sna.2008.11.011.

[20] Liwei Lin, A. P. Pisano, and R. T. Howe. A micro strain gauge with mechanical amplifier. *Microelectromechanical Systems, Journal of*, 6(4):313–321, 1997. 1057-7157.

[21] Babak Jamshidi, Robert G. Azevedo, Anand V. Jog, and Albert P. Pisano. Enhanced cross-axis rejection capacitive strain gauge. *ASME Conference Proceedings*, 2007(4305X):535–539, 2007.

[22] William C. Tang, Tu-Cuong H. Nguyen, Michael W. Judy, and Roger T. Howe. Electrostatic-comb drive of lateral polysilicon resonators. *Sensors and Actuators A: Physical*, 21(1-3):328–331, 1990.

[23] B. Jamshidi, R. G. Azevedo, M. B. J. Wijesundara, and A. P. Pisano. Corrosion enhanced capacitive strain gauge at 370c. In *Sensors, 2007 IEEE*, pages 804–807, 2007.

[24] Trey Allen William Roessig. Integrated mems tuning fork oscillators for sensor applications. *Ph. D. dissertation, University of California, Berkeley, Department of Mechanical Engineering*, 1998.

[25] Kenneth E. Wojciechowski. Design and fabrication of mems resonant strain sensor in soi. *Ph.D. dissertation, University of California, Berkeley, Department of Mechanical Engineering*, 2004.

[26] A. A. Seshia, M. Palaniapan, T. A. Roessig, R. T. Howe, R. W. Gooch, T. R. Schimert, and S. Montague. A vacuum packaged surface micromachined resonant accelerometer. *Journal of Microelectromechanical Systems*, 11(6):784–793, 2002. 1057-7157.

[27] A.A. Seshia, R.T. Howe, and S. Montague. An integrated microelectromechanical resonant output gyroscope. *MEMS 2002*, pages 722–726, 2002.

[28] Kenneth E. Wojciechowski. Electronics for resonant sensors. *Ph.D. dissertation, University of California, Berkeley, Department of Electrical Engineering*, 2005.

[29] Li Chen and Mehran Mehregany. A silicon carbide capacitive pressure sensor for in-cylinder pressure measurement. *Sensors and Actuators A: Physical*, 145-146:2–8, 2008.

[30] Sarah Wodin-Schwartz, David R. Myers, Rebecca K. Kramer, Sun Choi, Alex Jordon, Muthu B.J. Wijesundara, Matthew A. Hopcroft, and Albert P. Pisano. Silicon and silicon carbide survivability in an in-cylinder combustion environment. In *Proceedings of PowerMEMS*, pages 477–480, 2008.

[31] D. G. Senesky, B. Jamshidi, Cheng Kan Bun, and A. P. Pisano. Harsh environment silicon carbide sensors for health and performance monitoring of aerospace systems: A review. *Sensors Journal, IEEE*, 9(11):1472–1478, 2009.

[32] M. Mehregany, C. A. Zorman, N. Rajan, and Chien Hung Wu. Silicon carbide MEMS for harsh environments. *Proceedings of the IEEE*, 86(8):1594–1609, 1998.

[33] B. D. Sosnowchik, R. G. Azevedo, A. Cao, L. Lin, and A. P. Pisano. Silicon-to-steel bonding using rapid thermal annealing. *Advanced Packaging, IEEE Transactions on [see also Components, Packaging and Manufacturing Technology, Part B: Advanced Packaging, IEEE Transactions on]*, 28(4):626–634, 2005. 1521-3323.

[34] Brian D. Sosnowchik, Liwei Lin, and Albert P. Pisano. Rapid silicon-to-steel bonding using inductive heating. In *2006 ASME International Mechanical Engineering Congress and Exposition (2006)*, pages IMECE2006–15456, Chigaco, IL, 2006.

[35] R. G. Azevedo, I. Chen, O. M. O'Reilly, and A. P. Pisano. Influence of sensor substrate geometry on the sensitivity of mems micro-extensometers. In *International mechanical Engineering Congress and Exposition*, Orlando, Florida, USA, 2005.

[36] D. R. Myers and A. P. Pisano. Torque measurements of an automotive halfshaft utilizing a mems resonant strain gauge. In *Solid-State Sensors, Actuators and Microsystems Conference (Transducers) 2009.*, pages 1726–1729, 2009.

[37] W. C. West and et al. Fabrication and testing of all solid-state microscale lithium batteries for microspacecraft applications. *Journal of Micromechanics and Microengineering*, 12(1):58, 2002.

[38] T. Wacharasindhu, J. W. Kwon, D. E. Meier, and J. D. Robertson. Radioisotope microbattery based on liquid semiconductor. *Applied Physics Letters*, 95(1):014103–3, 2009.

[39] Rajesh Duggirala, Amit Lal, and Shankar Radhakrishnan. Radioisotope micropower generation: Integrated radioisotope actuated electro-mechanical power generators. In *Radioisotope Thin-Film Powered Microsystems*, volume 6 of *MEMS Reference Shelf*, pages 65–88. Springer New York, 2010.

[40] Allon I. Hochbaum, Renkun Chen, Raul Diaz Delgado, Wenjie Liang, Erik C. Garnett, Mark Najarian, Arun Majumdar, and Peidong Yang. Enhanced thermoelectric performance of rough silicon nanowires. *Nature*, 451(7175):163–167, 2008. 10.1038/nature06381.

[41] N. Chaimanonart, M. A. Suster, and D. J. Young. Two-channel passive data telemetry with remote rf powering for high-performance wireless and batteryless strain sensing microsystem applications. *Sensors Journal, IEEE*, 10(8):1375–1382, 2010.

[42] Babak Jamshidi. Poly-crystalline silicon carbide passivated capacitive mems strain gauge for harsh environments. *Ph.D. dissertation, University of California, Berkeley, Department of Mechanical Engineering*, 2008.

[43] V. Hatty, H. Kahn, J. Trevino, C. A. Zorman, M. Mehregany, R. Ballarini, and A. H. Heuer. Fracture toughness of low-pressure chemical-vapor-deposited polycrystalline silicon carbide thin films. *Journal of Applied Physics*, 99(1):013517, 2006.

[44] H. Wingbrant, H. Svenningstorp, P. Salomonsson, D. Kubinski, J.H. Visser, M. Lofdahl, and A.L. Spetz. Using a MISiC-FET sensor for detecting NH3 in SCR systems. *IEEE Sensors Journal*, 5(5):1099–1105, Oct. 2005.

[45] T.G. Brown, B. Davis, D. Hepner, J. Faust, C. Myers, C. Muller, T. Harkins, M. Holis, and B. Placzankis. Strap-down microelectromechanical MEMS sensors for high-g munition applications. *IEEE Transactions on Magnetics*, 37(1):336–342, Jan 2001.

[46] P. G. Neudeck, D. J. Spry, Chen Liang-Yu, G. M. Beheim, R. S. Okojie, C. W. Chang, R. D. Meredith, T. L. Ferrier, L. J. Evans, M. J. Krasowski, and N. F. Prokop. Stable electrical operation of 6H-SiC JFETs and ICs for thousands of hours at 500°C. *IEEE Electron Device Letters*, 29(5):456–459, 2008.

[47] SiC electronics market to reach $800m by 2015. *Semiconductor Today*, 2(9):22, November 2007.

[48] T. A. Roessig, R. T. Howe, A. P. Pisano, and J. H. Smith. Surface-micromachined resonant accelerometer. In *Solid State Sensors and Actuators, 1997. TRANSDUCERS '97 Chicago., 1997 International Conference on*, volume 2, pages 859–862 vol.2, 1997.

[49] D. S. Randall, M. J. Rudkin, A. Cheshmehdoost, and B. E. Jones. A pressure transducer using a metallic triple-beam tuning fork. *Sensors and Actuators A: Physical*, 60(1-3):160–162, 1997.

[50] P. K. Kinnell, M. C. L. Ward, and R. Craddock. Physical characterisation of selective stress coupling for resonant pressure sensors. *Sensors and Actuators A: Physical*, 115(2-3):230–234, 2004.

[51] M. A. Hopcroft, B. Kim, S. Chandorkar, R. Melamud, M. Agarwal, C. M. Jha, G. Bahl, J. Salvia, H. Mehta, H. K. Lee, R. N. Candler, and T. W. Kenny. Using the temperature dependence of resonator quality factor as a thermometer. *Applied Physics Letters*, 91(1):013505, 2007.

[52] Jeung-Hyun Jeong, Sung-Hoon Chung, Se-Ho Lee, and Dongil Kwon. Evaluation of elastic properties and temperature effects in Si thin films using an electrostatic microresonator. *Journal of Microelectromechanical Systems*, 12(4):524–530, Aug. 2003.

[53] Michele Pozzi, Musaab Hassan, Alun J. Harris, Jim S. Burdess, Liudi Jiang, Kin K. Lee, Rebecca Cheung, Gordon J. Phelps, Nick G. Wright, Christian A. Zorman, and Mehran Mehregany. Mechanical properties of a 3C-SiC film between room temperature and 600°c. *Journal of Physics D: Applied Physics*, 40(11):3335–3342, 2007.

[54] Di Gao, Muthu B. J. Wijesundara, Carlo Carraro, Roger T. Howe, and Roya Maboudian. Transformer coupled plasma etching of 3C-SiC films using fluorinated chemistry for microelectromechanical systems applications. *Journal of Vacuum Science and Technology B: Microelectronics and Nanometer Structures*, 22(2):513–518, 2004.

[55] Di Gao, Roger T. Howe, and Roya Maboudian. High-selectivity etching of polycrystalline 3c-sic films using hbr-based transformer coupled plasma. *Applied Physics Letters*, 82(11):1742–1744, 2003.

[56] D. G. Senesky and A. P. Pisano. Aluminum nitride as a masking material for the plasma etching of silicon carbide structures. In *Micro Electro Mechanical Systems (MEMS), 2010 IEEE 23rd International Conference on*, pages 352–355, 2010.

[57] Christopher S. Roper, Velimir Radmilovic, Roger T. Howe, and Roya Maboudian. Single-source chemical vapor deposition of sic films in a large-scale low-pressure CVD growth, chemical, and mechanical characterization reactor. *Journal of The Electrochemical Society*, 153(8):C562–C566, 2006.

[58] Matthew A. Hopcroft. Temperature-stabilized silicon resonators for frequency references. *Ph.D. dissertation, Stanford University, Department of Mechanical Engineering*, 2007.

[59] Donald B. Sullivan, David W. Allan, David A. Howe, and Eds. Fred L. Walls, editors. *Characterization of Clocks and Oscillators*. US Government Printing Office, 1990.

[60] Wen-Teng Chang and Christian Zorman. Grain size control of (111) polycrystalline 3c-sic films by doping used as folded-beam mems resonators for energy dissipation. *Microsystem Technologies*, 15(6):875–880, 2009.

[61] E. P. Quevy and R. T. Howe. Redundant mems resonators for precise reference oscillators. In *The 2005 IEEE Radio Frequency integrated Circuits (RFIC) Symposium*, pages 113–116, 2005.

[62] B. Kim, M. A. Hopcroft, R. N. Chandler, C. M. Jha, M. Agarwal, R. Melamud, S. A. Chandorkar, G. Yama, and T. W. Kenny. Temperature dependence of quality factor in MEMS resonators. *JMEMS*, 17(3):755–766, 2008.

[63] R. Melamud, B. Kim, M. A. Hopcroft, S. Chandorkar, M. Agarwal, C. M. Jha, and T. W. Kenny. Composite flexural-mode resonator with controllable turnover temperature. *MEMS 2007, Kobe, Japan*, pages 199–202, January 2007.

[64] W.-T. Hsu, J. R. Clark, and C. T.-C. Nguyen. Mechanically temperature-compensated flexural-mode micromechanical resonators. *IEEE Int. Electron Devices Meeting*, pages 399–402, December 2000.

[65] R. Melamud, S. A. Chandorkar, Kim Bongsang, Lee Hyung Kyu, J. C. Salvia, G. Bahl, M. A. Hopcroft, and T. W. Kenny. Temperature-insensitive composite micromechanical resonators. *Microelectromechanical Systems, Journal of*, 18(6):1409–1419, 2009.

[66] Robert Glen Azevedo. Silicon carbide micro-extensometers for harsh envirnments. *Ph. D. dissertation, University of California, Berkeley, Department of Materials*, 2007.

[67] Kamili M. Jackson. Fracture strength, elastic modulus and poisson's ratio of polycrystalline 3c thin-film silicon carbide found by microsample tensile testing. *Sensors and Actuators A: Physical*, 125(1):34–40, 2005.

[68] Robert R. Reeber and Kai Wang. Lattice parameters and thermal expansion of important semiconductors and their substrates, 2000.

[69] G. A. Slack and S. F. Bartram. Thermal expansion of some diamondlike crystals. *J. Applied Physics*, 46(1):89–98, 1975.

[70] R. R. Reeber and K. Wang. Thermal expansion and lattice parameters of group IV semiconductors. *Materials Chemistry and Physics*, 46:259–264, 1996.

[71] R. R. Reeber and K. Wang. Thermal expansion of β-SiC, GaP and InP. *Materials Research Symposium Proceedings*, 410:211–216, 1996.

[72] N. Maluf. *An Introduction to Microelectromechanical Systems Engineering.* Artech House, Boston, MA, 2000.

[73] Adam G. Rehorn, Jin Jiang, and Peter E. Orban. State-of-the-art methods and results in tool condition monitoring: a review. *The International Journal of Advanced Manufacturing Technology*, 26(Volume 26, Numbers 7-8):693–710, 2005.

[74] J. Beckley, V. Kalinin, M. Lee, and K. Voliansky. Non-contact torque sensors based on saw resonators. In *Frequency Control Symposium and PDA Exhibition, 2002. IEEE International*, pages 202–213, 2002.

[75] J. J. Sniegowski, H. Guckel, and T. R. Christenson. Performance characteristics of second generation polysilicon resonating beam force transducers. In *Solid-State Sensor and Actuator Workshop, 1990. 4th Technical Digest., IEEE*, pages 9–12, 1990.

[76] W.C. Young and R.G. Budynas. *Roark's Formulas for Stress and Strain.* McGraw-Hill, 7 edition, 2002.

[77] D. R. Myers. Design and evaluation of a torque testing appartus for strain gauges. *Masters Thesis, University of California, Berkeley, Department of Mechanical Engineering*, 2007.

[78] Y. D. Kim, C. S. Lee, and S. J. Kwon. Novel 3d force sensor using ultra-thin silicon strain gauge bonded on metal membrane. In *Solid-State Sensors, Actuators and Microsystems Conference (Transducers) 2009.*, pages 1920–1923, 2009.

[79] Marco F. Aimi, Masa P. Rao, Noel C. MacDonald, Abu Samah Zuruzi, and David P. Bothman. High-aspect-ratio bulk micromachining of titanium. *Nat Mater*, 3(2):103–105, 2004. 10.1038/nmat1058.

[80] Marco Francesco Aimi. Bulk titanium microelectromechanical systems. *Ph. D. dissertation, University of California, Santa Barbara, Department of Materials*, 2007.

[81] K. S. Lebouitz, A. Mazaheri, R. T. Howe, and A. P. Pisano. Vacuum encapsulation of resonant devices using permeable polysilicon. *Proceedings of the IEEE Micro Electro Mechanical Systems (MEMS)*, pages 470–475, 1999.

[82] Rihui He and Chang-Jin Kim. On-wafer monolithic encapsulation by surface micromachining with porous polysilicon shell. *Microelectromechanical Systems, Journal of*, 16(2):462–472, 2007.

[83] G. J. A. M. Verheijden, G. E. J. Koops, K. L. Phan, and J. T. M. van Beek. Wafer level encapsulation technology for mems devices using an hf-permeable pecvd sioc capping layer. *Proceedings of the IEEE Micro Electro Mechanical Systems (MEMS)*, pages 798–801, 2008.

[84] Rihui He and Chang-Jin Kim. Low-temperature monolithic encapsulation using porous-alumina shell anodized on chip. *Journal of Microelectromechanical Systems*, 18(3):588–596, 2009.

[85] R. N. Candler, Park Woo-Tae, Li Huimou, G. Yama, A. Partridge, M. Lutz, and T. W. Kenny. Single wafer encapsulation of mems devices. *Advanced Packaging, IEEE Transactions on*, 26(3):227–232, 2003.

[86] V. Rajaraman, L.S. Pakula, H.T.M. Pham, P.M. Sarro, and P.J. French. Robust wafer-level thin film encapsulation of microstructures using low stress pecvd silicon carbide. *Proceedings of the IEEE Micro Electro Mechanical Systems (MEMS)*, pages 140–143, 2009.

[87] A. Hchst, R. Scheuerer, H. Stahl, F. Fischer, L. Metzger, R. Reichenbach, F. Lrmer, S. Kronmller, S. Watcham, C. Rusu, A. Witvrouw, and R. Gunn. Stable thin film encapsulation of acceleration sensors using polycrystalline silicon as sacrificial and encapsulation layer. *Sensors and Actuators A: Physical*, 114(2-3):355–361, 2004.

[88] Jennifer L. Lund, Christopher V. Jahnes, Hariklia Deligianni, L. Paivikki Buchwalter, John M. Cotte, Panayotis Andricacos, David E. Seeger, and John H. Magerlein. A low temperature bi-cmos compatible process for mems rf resonators and filters. *Proceedings of the Solid-State Sensor, Actuator, and Microsystems Workshop (Hilton Head)*, pages 38–40, 2002.

[89] B. H. Stark and K. Najafi. A low-temperature thin-film electroplated metal vacuum package. *Journal of Microelectromechanical Systems*, 13(2):147–157, 2004.

[90] A. Toma, D. Chiappe, D. Massabo, C. Boragno, and F. Buatier de Mongeot. Self-organized metal nanowire arrays with tunable optical anisotropy. *Applied Physics Letters*, 93(16):163104, 2008.

[91] Cha Daigil, H. Shin Jung, Park Sangjin, Lee Eunha, Park Yoondong, Park Young-soo, Yoo In-Kyeong, Seol Kwang Soo, and Choi Suk-Ho. High trap density and long retention time from self-assembled amorphous si nanocluster floating gate nonvolatile memory. *Applied Physics Letters*, 89(24):243513, 2006.

[92] D.G. Jones, R.G. Azevedo, M.W. Chan, A.P. Pisano, and M.B.J. Wijesundara. Low temperature ion beam sputter deposition of amorphous silicon carbide for wafer-level vacuum sealing. *Proceedings of the IEEE Micro Electro Mechanical Systems (MEMS)*, pages 275–278, Jan. 2007.

[93] James K. Hirvonen. Ion beam assisted deposition. *Materials Research Society Symposium Proceedings*, 792:R12.5.1–11, 2004.

[94] L. Guzman, B. Y. Man, A. Miotello, M. Adami, and P. M. Ossi. Ion beam induced enhanced adhesion of au films deposited on polytetrafluoroethylene. *Thin Solid Films*, 420-421:565–570, 2002. doi: DOI: 10.1016/S0040-6090(02)00839-8.

[95] P. J. Martin, R. P. Netterfield, and W. G. Sainty. Modification of the optical and structural properties of dielectric zro[sub 2] films by ion-assisted deposition. *Journal of Applied Physics*, 55(1):235–241, 1984.

[96] T. Miyano and H. Kitamura. Coating on the cutting edge of an electric shaver by ion beam assisted deposition. *Surface and Coatings Technology*, 65(1-3):179–183, 1994. doi: DOI: 10.1016/S0257-8972(94)80028-6.

[97] A. Partridge, A. E. Rice, T. W. Kenny, and M. Lutz. New thin film epitaxial polysilicon encapsulation for piezoresistive accelerometers. In *Micro Electro Mechanical Systems, 2001. MEMS 2001. The 14th IEEE International Conference on*, pages 54–59, 2001.

[98] R. G. Azevedo, D. R. Myers, and A. P. Pisano. Temperature-insensitive silicon carbide resonant micro-extensometers. In *15th International Conference on Solid State Sensors and Actuators. Denver, CO*, pages 268–271, 2009.

[99] Di Giovanni. *Flat and Corrugated Diaphragm Design Handbook*. CRC Press, 1982.

[100] Michio Mizutani, Kimihiro Sasaki, and Tomonobu Hata. Investigation of ion beam sputtering process by monte carlo simulation. *Electronics and Communications in Japan (Part II: Electronics)*, 81(12):41–47, 1998.